Alma Mater Studiorum – Università di Bologna

DOTTORATO DI RICERCA IN
MONITORAGGIO E GESTIONE DELLE STRUTTURE E DELL'AMBIENTE

Ciclo 34

Settore Concorsuale: 08/A1 - IDRAULICA, IDROLOGIA, COSTRUZIONI IDRAULICHE E MARITTIME

Settore Scientifico Disciplinare: Settore ICAR/02 - Costruzioni Idrauliche e Marittime e Idrologia

Anthropogenic and climatic controls on surface water across the contiguous United States

Presentata da:
Irene Palazzoli

Supervisore:
Dott.ssa Serena Ceola

Co-Supervisore:
Prof. Alberto Montanari

Coordinatore Dottorato:
Prof. Alessandro Marzani

Esame finale anno 2022

To my family

Table of contents

Table of contents .... **v**

List of Figures .... **ix**

List of Tables .... **xv**

List of Acronyms and Abbreviations .... **xvii**

Abstract .... **xix**

Sommario .... **xxi**

1 Introduction **1**

1.1 Objectives and methodology 3

1.2 Outline of the Thesis 5

2 Literature review **7**

2.1 Surface water 7

2.2 Human pressure on surface water 9

2.2.1 Population growth and urbanization 10

2.2.2 Irrigation 11

2.3 Effects of climate change on surface water 13

2.3.1 Precipitation change 14

2.3.2 Temperature change 15

2.4 Remote sensing data 17

2.4.1 Remote sensing of surface water 18

2.4.2 Remote sensing of human dynamics 20

2.4.3 Remote sensing of climate variability 22

3 Study area and data **25**

3.1 The contiguous United States 25

3.1.1 Surface water in the contiguous United States: supply and demand 26

3.1.2 Climate change in the contiguous United States 30

3.2 Input datasets 33

3.2.1 Global Surface Water dataset 33

3.2.2 Global Human Settlement dataset 35

3.2.3 Irrigated Agriculture Dataset for the United States 35

3.2.4 Daymet dataset 37

4 Research Objective 1: Anthropogenic and climatic drivers of surface water extent change 39

4.1 Surface water, human dynamics, and climatic data 40

4.2 Assessment of the change in surface water extent, anthropogenic and climatic contributors 43

4.3 Results 46

4.3.1 Change in surface water extent 46

4.3.2 Change in the anthropogenic and climatic drivers 48

4.3.3 Contributors of changes in surface water extent 54

5 Research Objective 2: Spatial distribution of surface water loss from urban areas 61

5.1 Surface water loss and urban area data 63

5.2 Assessment of the spatial influence of urban areas on surface water loss 66

5.2.1 Observed frequency of surface water loss occurrence 66

5.2.2 Distance-decay model of surface water loss occurrence 68

5.2.3 Overall surface water extent *versus* surface water loss: comparison of distance decay patterns 70

5.2.4 Influence of climate 70

5.3 Results 71

5.3.1 Observed spatial interaction between surface water loss and urban areas 71

5.3.2 Spatial interaction between surface water loss and urban areas: distance-decay model application 71

5.3.3 Overall surface water extent *versus* surface water loss: comparison of distance decay patterns 82

5.3.4 Influence of climate 83

6 Conclusions 87

6.1 Achievements 88

6.2 Constraints 90

6.3 Recommendations 91

References 95

Appendix A 113

Appendix B 117

List of Figures

Figure 2.1 Bar chart showing the distribution of Earth's water (numbers are rounded). 8

Figure 2.2 Number of months per year during which water scarcity exceeds 1.0 (data over the time period 1996-2005). Figure taken from Mekonnen & Hoekstra (2016). 9

Figure 2.3 Trends of urban and rural population of the world from 1950 to 2050. Data source: United Nations, Department of Economic and Social Affairs, Population Division (United Nations, 2019). 11

Figure 2.4 Water stress of the major river basins expressed as a percentage of incremental evaporation due to irrigation over the outflows generated from groundwater and surface water resources. Figure adapted from Hoogeveen et al. (2015).. 13

Figure 2.5 Global annual precipitation anomaly compared to the average precipitation from 1901 to 2020 based on rainfall and snowfall measurements collected at weather stations worldwide. Data source: National Oceanic & Atmospheric Administration (NOAA) via the US EPA (EPA, 2016)... 15

Figure 2.6 Global annual temperature anomaly compared to the average temperature from 1901 to 2020 based on the combination of a set of land-based weather stations and sea surface temperature measurements worldwide. Data source: National Oceanic & Atmospheric Administration (NOAA) via the US EPA (EPA, 2016)... 16

Figure 2.7 Difference between passive and active sensors aboard a satellite. Passive sensors exploit the natural energy of the Sun. Active sensors provide their own energy. Figure taken from https://earthdata.nasa.gov/learn/backgrounders/remote-sensing. 17

Figure 2.8 Spectral signature showing the reflectance of water, soil, and vegetation at different wavelengths. Figure taken from https://seos-project.eu/classification/classification-c01-p05.html. 18

Figure 3.1 Main climatic regions of the Köppen-Geiger climate classification system found within the CONUS.. 25

Figure 3.2 Area of the contiguous United States with its 18 water resource regions (WRRs) and 204 river basins. 26

Figure 3.3 Main river systems of the United States. Major rivers of the West are highlighted in red, while major river systems of the East are highlighted in blue. 27

Figure 3.4 Map of surface water withdrawals in the United States in 2015, indicating top 5 states (and their percentage of total withdrawals) that were responsible for the largest withdrawals. 1 gallon corresponds to approximately 4.55 liters. Figure adapted from Dieter et al. (2018)...28

Figure 3.5 Frequency of irrigation in the United States in 2002, 2007, 2012, and 2017 obtained from the Irrigated Agriculture Dataset for the United States product (MIrAD-US). Circles show zoom in of areas that have been irrigated more frequently. Figure adapted from https://www.usgs.gov/media/images/mirad-irrigation-frequency-years-2002-2007-2012-and-2017. 29

Figure 3.6 Urban population growth in the United States from 1960 to 2020 as a percentage of total population. Data source: World Bank Data (https://data.worldbank.org/indicator/SP.URB.TOTL.IN.ZS?locations=US).......................30

Figure 3.7 Percentage variation of total annual precipitation in 2020 with respect to the values observed in 1901 for the CONUS and 1925 for Alaska. Figure adapted from https://www.epa.gov/climate-indicators/climate-change-indicators-us-and-global-precipitation..31

Figure 3.8 Rate of change in annual average air temperature with respect to the values observed in 1901 for the CONUS and 1925 for Alaska. Figure adapted from https://www.epa.gov/climate-indicators/climate-change-indicators-us-and-global-temperature...32

Figure 4.1 Maps of the change in surface water extent and its anthropogenic drivers over some representative regions of the CONUS. 42

Figure 4.2 Schematic representation of the methodology adopted for the analysis of the influence of anthropogenic and climatic drivers on the variation of surface water extent......43

Figure 4.3 Maps of the change in the climatic drivers over the CONUS..................................45

Figure 4.4 Spatial distribution of the net surface water change that occurred between the first (1984-1999) and the second (2000-2020) epoch across the river basins of the CONUS. 46

Figure 4.5 Histogram of the total amount of surface water gain (in blue), surface water loss (in red), and net surface water change (in green) across the main climatic regions of the CONUS.. 47

Figure 4.6 Histograms of the total amount of surface water gain (in blue), surface water loss (in red), and net surface water change (in green) across the subtypes of the main climatic regions of the CONUS. 48

Figure 4.7 Spatial distribution of the variations of the anthropogenic drivers that occurred between the two epochs considered in this study across the river basins of the CONUS. 49

Figure 4.8 Spatial distribution of the variations of the climatic drivers that occurred between the two epochs considered in this study across the river basins of the CONUS. 50

Figure 4.9 Histograms of the variation of the anthropogenic and climatic drivers across the main climatic regions of the CONUS. 51

Figure 4.10 Histograms of the variation of the total population across the subtypes of the main climatic regions of the CONUS. 52

Figure 4.11 Histograms of the variation of the total irrigated land across the subtypes of the main climatic regions of the CONUS. 52

Figure 4.12 Histograms of the variation of the mean annual precipitation across the subtypes of the main climatic regions of the CONUS. 53

Figure 4.13 Spatial overlap of potential contributors to a net surface water gain. 55

Figure 4.14 Spatial overlap of potential contributors to a net surface water loss. 56

Figure 5.1 Surface water loss locations and urban areas across the river basins and water resource regions of the CONUS. 65

Figure 5.2 Schematic representation of the spatial interaction between surface water loss locations and urban areas hypothesized in this analysis. 66

Figure 5.3 Performance of the distance-decay model reproducing the observed frequency of occurrence of surface water loss from urban areas, based on a 3 km wide distance bin. 72

Figure 5.4 Performance of the distance-decay model reproducing the observed frequency of occurrence of surface water loss from urban areas in the 14 water resource regions of the CONUS (panels a-n) that are not shown in Figure 5.3, based on a 3 km wide distance bin. .73

Figure 5.5 Comparison between the observed and theoretical average distance of surface water loss locations from urban areas ($\langle d_x \rangle$ and $\langle \hat{d}_x \rangle$) based on a 3 km wide distance bin and their frequency distribution. 76

Figure 5.6 Spatial variability and frequency distribution of α_b and β_b parameters of the distance-decay model based on a 3 km wide distance bin and applied at the river basin level.............. 77

Figure 5.7 Spatial variability of α_{WRR} and β_{WRR} parameters of the distance-decay model based on a 3 km wide distance bin and applied at the water resource region level. 78

Figure 5.8 Spatial distribution of urban attributes within river basins of the CONUS. 79

Figure 5.9 Correlation between urban attributes and α_x and β_x parameters of the distance-decay model for the three levels of spatial aggregation (river basins, water resource regions, and the CONUS). 80

Figure 5.10 Correlation between the extent of the largest urban clusters and α_b and β_b parameters for the 191 river basins of the CONUS where the distance-decay model was applied using a 3 km wide distance bin. 81

Figure 5.11 Correlation between the interquartile range of the extent of urban clusters and β_b parameter for the 191 river basins of the CONUS where the distance-decay model was applied using a 3 km wide distance bin (coefficient of determination $R^2 = 0.14$). 81

Figure 5.12 Spatial distribution of the difference between the decay rate associated to the distance-decay of surface water loss (β_b) and the overall extent of surface water (β_b^{sw}) across 191 river basins of the CONUS where the distance-decay model was applied using a 3 km wide distance bin. 82

Figure 5.13 Variability of the decay rate at the river basin level associated to the distance-decay of surface water loss (β_b) and the overall extent of surface water (β_b^{sw}). 83

Figure 5.14 Variability of α_b and β_b parameters of the distance-decay model applied at the river basin level across the main climatic regions of the CONUS.. 84

Figure 5.15 Variability of the decay rate at the river basin level associated to the distance-decay of surface water loss (β_b) and to the overall extent of surface water (β_b^{sw}) across the main climatic regions of the CONUS. 86

Figure A1 Sub-types (22 classes) of climatic regions defined by the Köppen-Geiger climate classification system found within the CONUS. 113

Figure A2 Total extent of surface water gain, loss, and net variation (gain – loss) across the CONUS as a function of the adopted threshold of change in the frequency of water observation. 113

Figure A3 Variability of the water occurrence averaged over the river basins of the CONUS for each class of water transition included in the Surface Water Loss map. 114

Figure A4 Spatial distribution of the average water occurrence for each class of water transition included in the Surface Water Loss map across the river basins of the CONUS. 114

Figure A5 Spatial distribution of the representativeness of each class of water transition included in the Surface Water Loss map across the river basins of the CONUS. 115

Figure A6 Spatial distribution of surface water loss clusters across the river basins of the CONUS. a Total number of surface water loss clusters. b Spatial extent of the largest surface water loss clusters. 115

Figure A7 Spatial distribution of the extent of the largest urban clusters across river basins of the CONUS. 116

Figure A8 Comparison between the frequency of occurrence of surface water loss across distance classes based on 1, 3, and 5 km wide distance bins. 116

Figure B1 Spatial variability of α_b and β_b. parameters of the distance-decay model based on a 1 km wide distance bin and applied at the river basin level. 117

Figure B2 Spatial variability of α_{b} and β_{b} parameters of the distance-decay model based on a 5 km wide distance bin and applied at the river basin level. 118

Figure B3 Spatial variability of α_{WRR} and β_{WRR} parameters of the distance-decay model based on a 1 km wide distance bin and applied at the water resource region level. 119

Figure B4 Spatial variability of α_{WRR} and β_{WRR} parameters of the distance-decay model based on a 5 km wide distance bin and applied at the water resource region level. 120

List of Tables

Table 4.1 Number of basins of the CONUS satisfying a specific combination of direction of change (increase or decrease) in the anthropogenic (population, POP, and irrigated land, IRR) and climatic (precipitation, PCP) drivers.. 54

Table 4.2 Values of changes in surface water extent (SW), anthropogenic factors (population, POP, and irrigated land, IRR), and climatic factor (precipitation, PCP) across the main climatic regions of the CONUS and their subtypes....................58

Table 5.1 Main physical and climatic properties and model fit results, based on a 3 km wide distance bin, for the CONUS and four representative water resource regions and related river basins (see Figure 5.3). 74

Table B1 Main physical and climatic properties and model fit results, based on a 3 km wide distance bin, for the 18 water regions and 204 river basins across the CONUS.................... 121

List of Acronyms and Abbreviations

CONUS: Contiguous United States

EO: Earth observation

ET: Evapotranspiration

FAO: Food and Agriculture Organization of the United Nations

IRR: Irrigated land

LST: Land surface temperature

MNDWI: Modified Normalized Difference Water Index

MODIS: Moderate Resolution Imaging Spectroradiometer

NDWI: Normalized Difference Water Index

NLCD: National Land Cover Dataset

OLI: Operational Land Imager

PAR: Photosynthetically active radiation

PCP: Precipitation

POP: Population

RO: Research Objective

SWO: Surface Water Occurrence

TIRS: Thermal Infrared Sensor

TM: Thematic Mapper

TMP: Temperature

URB: Urban area

WRR: Water resource region

Abstract

Anthropogenic activities and climatic processes heavily influence surface water resources and they often produce severe impacts which in turn affect both humans and the environment. Nonetheless, it is now evident that the functioning of societies and the preservation of aquatic ecosystems is dangerously threatened by the progressive depletion of freshwater resources, as many regions of the world are currently facing the issue of water scarcity while the ecological integrity of several ecosystems has been already compromised. Therefore, there is an urgent need to understand the effective contribution and the spatial influence of anthropogenic and climatic dynamics on the variation of surface water availability. Earth observations gathered from remotely-sensed data allow to thoroughly explore this research issue. Here, this investigation is performed at the regional scale by focusing on the study area of the contiguous United States (CONUS), which embeds heterogeneous hydroclimatic and socio-economic conditions. Three anthropogenic (i.e., urban area, population, and irrigated land) and two climatic factors (i.e., precipitation and temperature) were selected as potential drivers of changes in surface water extent. The analysis of the possible overlap between the changes (increase or decrease) in these drivers and the variation of surface water extent that occurred from 1984 to 2020 was then examined at the river basin level. Overall, most of the river basins experienced a net gain of surface water extent (i.e., a transition from land to water) due to an increase in precipitation, especially in the eastern region of the CONUS, and a reduction of irrigated land, mainly located in the western area. However, the river basins of the arid southwestern region of the CONUS along with some river basins situated in the northeastern area encountered a net loss of their surface water extent (i.e., a transition from water to land), which resulted to be essentially induced by population growth with the additional contribution of the precipitation deficit that hit the southwestern region and a general expansion of irrigated land. To further inspect the role of population growth and urbanization on the spatial distribution of surface water loss, a detailed spatially-explicit analysis of the interaction between human settlements and surface water depletion was carried out. In particular, the decrease of frequency of occurrence of surface water loss was analyzed and modeled as a function of distance from urban areas across the CONUS. The exponential distance-decay model defined in this analysis successfully reproduced the observed spatial trend, confirming the presence of a higher frequency of surface water loss in the proximity of human settlements and providing innovative insights on surface water loss patterns at different spatial scales (i.e., river basins, water resource regions, and the CONUS). These spatial patterns are found to be influenced by climatic conditions, with more widely distributed losses in arid regions with respect to temperate and continental climates. The results presented in this Thesis provide a new and deeper understanding of the contribution and the spatial influence of anthropogenic and climatic dynamics on the variation of surface water availability, which could be effectively integrated in the definition of sustainable strategies for urbanization, water management, and surface water restoration, considering both human and environmental water needs.

Keywords: surface water resources, surface water depletion, anthropogenic drivers, climatic drivers, distance-decay model, human pressure.

Sommario

Le attività antropiche e i processi climatici esercitano un'influenza notevole sulle risorse idriche superficiali, causando spesso gravi impatti che a loro volta colpiscono l'uomo e l'ambiente. Il funzionamento delle società e la preservazione degli ecosistemi di acqua dolce sono infatti fortemente minacciati dal progressivo esaurimento delle risorse idriche. Numerose aree a livello globale presentano una situazione di notevole criticità a causa della scarsità di risorsa idrica, con conseguenze catastrofiche che vanno a minare l'integrità di numerosi ecosistemi acquatici e terrestri. Per questi motivi, è necessario comprendere approfonditamente l'effettivo contributo di dinamiche antropiche e climatiche sulla variazione dell'estensione delle risorse idriche superficiali, analizzandone anche l'influenza a livello locale. Le immagini della superficie terrestre rilevate dai sensori satellitari permettono di approfondire questa problematica. Nella presente Tesi, tale indagine viene eseguita alla scala regionale focalizzando l'attenzione sull'area di studio degli Stati Uniti continentali (CONUS), la quale è caratterizzata da condizioni idro-climatiche e socio-economiche estremamente eterogenee. In primo luogo, per valutare l'effetto di fattori antropici e climatici sulla variazione dell'estensione della risorsa idrica superficiale sono stati selezionati tre fattori antropici (estensione dell'area urbana e della superficie irrigata, distribuzione della popolazione) e due fattori climatici (precipitazione e temperatura) in qualità di potenziali cause di tale variazione. Lo studio della possibile sovrapposizione tra la variazione (intesa come incremento e decremento) di tali fattori e quella associata alla risorsa idrica superficiale, verificatesi tra il 1984 e il 2020, è stata quindi valutata a scala di bacino idrografico. Complessivamente, nella gran parte dei bacini del CONUS si è verificato un aumento netto dell'estensione della risorsa idrica superficiale (equivalente ad una transizione da suolo ad acqua), le cui cause potrebbero essere associate ad un incremento della precipitazione, specialmente nella regione orientale del CONUS, e ad una riduzione della superficie irrigata, principalmente localizzata nell'area occidentale. Una netta riduzione dell'estensione della risorsa idrica superficiale (equivalente ad una transizione da acqua a suolo) è stata invece osservata nei bacini idrografici appartenenti alla regione arida sudoccidentale nonché in alcuni bacini situati nell'area nordorientale del CONUS. Tale riduzione sembra ricondursi ad una significativa crescita demografica, a cui si aggiungono una diminuzione delle precipitazioni (prevalentemente nella regione sudoccidentale) e una generale espansione della superficie irrigata. In secondo luogo, per valutare in maniera più approfondita il ruolo della crescita demografica e urbana sulla distribuzione spaziale (a livello locale) delle risorse idriche superficiali perse all'interno del CONUS, è stata effettuata un'analisi dettagliata dell'interazione nello spazio tra gli agglomerati urbani e l'esaurimento delle risorse idriche superficiali. Nello specifico, è stato analizzato la distribuzione nello spazio della frequenza di osservazione della perdita di risorsa idrica superficiale in funzione della distanza dalle aree urbane all'interno del CONUS. Successivamente è stato definito un modello esponenziale di distance-decay che ha riprodotto con successo l'andamento osservato nello spazio, confermando la presenza di una maggiore frequenza di perdita di risorsa idrica superficiale in prossimità degli agglomerati urbani. Tale modello è stato applicato a vari livelli di aggregazione spaziale (bacino idrografico, regione idrica e CONUS), fornendo una visione innovativa della distribuzione spaziale dell'esaurimento della risorsa idrica. È emerso, inoltre, come le caratteristiche climatiche prevalenti abbiano influenzato le distribuzioni spaziali osservate e riprodotte dal modello. In particolare, le regioni caratterizzate da climi aridi presentano delle perdite di risorsa idrica superficiale maggiormente distribuite rispetto a quelle caratterizzate da climi temperati e continentali. I risultati presentati in questa Tesi offrono una conoscenza più approfondita del contributo e dell'influenza a livello locale da parte delle dinamiche antropogeniche e climatiche sulla variazione della risorsa idrica superficiale disponibile. Tale conoscenza può essere integrata nella definizione di strategie sostenibili di gestione del processo di urbanizzazione, delle risorse idriche e del loro ripristino, che tengano conto delle esigenze sia della società che dell'ambiente.

Parole chiave: risorse idriche superficiali, esaurimento delle risorse idriche superficiali, fattori antropici, fattori climatici, modello di distance-decay, pressione antropica.

1 Introduction

Water is a major and unique resource for humans and the environment. Indeed, beyond being essential for life on Earth, water represents also an indispensable element to the economic wealth of societies and to numerous ecosystems (Poff et al., 1997; Vörösmarty et al., 2010; Cosgrove & Loucks, 2015; Granzotti et al., 2018). Among all the water resources, surface water, i.e., water bodies found on land surface, plays an essential role for freshwater supply and the preservation of freshwater ecosystems and functions (Poff et al., 1997; Jenkins et al., 2010; Dieter et al., 2018; Granzotti et al., 2018). However, socioeconomic and technological development, water-management policies, and climate variability are responsible for the spread of multiple pressures on surface water resources (Delpla et al., 2009; Averyt et al., 2013; Yigzaw & Hossain, 2016; Duran-Encalada et al., 2017; Brown et al., 2019b; Erler et al., 2019). Human activities severely affect water bodies, as they often compromise water quantity and quality and threaten ecological integrity through the artificial modification of the morphology and the flow regime of water bodies as well as the introduction of pollutants, which put at risk water security and the biodiversity of aquatic ecosystems (Cosgrove & Loucks, 2015; Wanders & Wada, 2015; Grizzetti et al., 2017; Wada et al., 2017). Moreover, water demand is rapidly increasing worldwide due to the global demographic growth, improved living standards, changing consumption patterns, and the expansion of irrigated agriculture (Mekonnen & Hoekstra, 2016). As a result, surface water resources are exploited at an accelerating rate to satisfy the subsequent larger demands for consumptive use, food production, and power generation (McDonald et al., 2011a, 2011c; Okello et al., 2015; Yigzaw & Hossain, 2016). Furthermore, surface water resources are highly exposed to climate change, as they are extremely dependent on precipitation and temperature (Kifle Arsiso et al., 2017). Future climate variability, along with the anthropogenic impacts due to urban and economic growth, is expected to further impact surface water resources from rivers, lakes, reservoirs, and wetlands, as the climatic changes are projected to amplify both their magnitude and severity over the next decades (Okello et al., 2015; Kummu et al., 2016). All these factors introduce uncertainties on future availability of surface water, increasing the risk of water scarcity and ecosystems degradation and posing a serious challenge for sustainable development (Haddeland et al., 2006; Ferguson & Maxwell, 2012; Khatri & Tyagi, 2015; Liyanage & Yamada, 2017; Botter & Durighetto, 2020). The analysis of how human actions and climate change affected surface water availability is key to understand and prevent future issues with water shortages and the associated social, political, and environmental implications (Cosgrove & Loucks, 2015). Thus, the identification of the dominant drivers of the change in surface water availability is crucial as the following questions need to be addressed:

(Q1a) How has the spatial extent of surface water changed in the last 40 years?

(Q1b) What are the main anthropogenic and climatic factors governing the remotely-sensed change of surface water extent and where do they determine a gain/loss of surface water (i.e., a transition from land to water/water to land)?

Furthermore, it is well acknowledged that human activities in urban areas strongly rely on surface waters causing an excessive stress on local water sources, which are destined to gradually disappear (McDonald et al., 2014). Even though the impacts of urbanization on the environment have been long studied, the consequences of urban development on water resources, and especially the dynamics of spatial interaction between urban areas and surface water loss, are less known (Bigelow et al., 2017; Cooley et al., 2021). In particular, it is necessary to unravel the spatial influence of human settlements on surface water depletion to discover and examine the presence of hotspots of localized and concentrated pressure on surface waters, which may produce negative effects on human life and the environment (Padowski & Jawitz, 2012; Wada et al., 2016; Boretti & Rosa, 2019). The anthropogenic overexploitation induced by growing urban water demand raises concerns on future availability of surface waters and requires an answer to the following questions:

(Q2a) Where does urbanization cause surface water loss?

(Q2b) How does the frequency of surface water loss change as the distance from human settlements increases?

Over the past decade the application of satellite-based information has extraordinarily expanded thanks to the exceptional advantages supplied by this technology, such as data with global spatial coverage and high temporal resolution (Sheffield et al., 2018; Seydi et al., 2020; Afaq & Manocha, 2021). Remote sensing imagery represents a robust source of data for the detection and monitoring of any process of environmental or anthropogenic change that takes place above the Earth's surface, providing critical information for the control and prevention of natural and human-induced calamities (Asokan & Anitha, 2019; Karthikeyan et al., 2020). For instance, images captured by satellite sensors allow the measurement of key components of the hydrological cycle, such as precipitation, evaporation, water bodies levels, soil moisture, and snow, and the observation of processes related to human activities, such as urban areas development, land use and land cover change (Fang et al., 2018; Wang et al., 2018; Xiong et al., 2018; Liu et al., 2020).

The study area of the contiguous United States (CONUS) offers a unique opportunity to investigate the impacts of human dynamics and climate change on surface water resources over a large and heterogeneous territory, which includes regions characterized by diverse hydroclimatic conditions, and with spatially-varying topography, surface water availability, and degree of urbanization. Finally, performing such an investigation on the CONUS gives the additional benefit of a large volume of freely accessible data, including remotely-sensed data (Di Baldassarre et al., 2021).

1.1 Objectives and methodology

The first Research Objective (RO1) of this Thesis aims at addressing questions (Q1a) and (Q1b) by evaluating the influence of anthropogenic and climatic factors on the variation of surface water extent at the river basin and climatic region level across the CONUS from 1984 to 2020 (Pekel et al., 2016). The variation that occurred before and after the year 2000 in surface water extent and its anthropogenic and climatic drivers was evaluated to determine which factors played a key role in the gain and loss of surface water resources. Three anthropogenic and two climatic drivers were involved in this analysis: urban area, population, and irrigated land were the variables representing human dynamics (anthropogenic drivers), while precipitation and temperature were used to account for the effects due to climate variability (climatic drivers). Maps of the changes in surface water extent and its drivers that took place between 1984-1999 (first epoch) and 2000-2020 (second epoch) were generated from datasets derived from satellite images and ground-based observations. More specifically, locations of gains and losses of surface water were extracted to obtain the net variation of surface water extent (given by the difference between the total gain and total loss) at the scale of river basin and climatic region. Subsequently, the total built-up area, total population distribution, total irrigated land, as well as the mean annual precipitation, and mean monthly temperature observed over the first and second epoch were defined to calculate the variation of the drivers between the two time-windows. The potential overlap between the net surface water gain and loss and the corresponding direction of change of their drivers was assessed across the river basins of the CONUS to establish which among the considered anthropogenic and climatic factors contributed the most to the variation of surface water availability. Finally, the influence of climate was verified as well, by looking at the climatic regions of the CONUS and their subtypes, as defined by the Köppen-Geiger classification system (Beck et al., 2018). In particular, trends of change in surface water extent and its anthropogenic and climatic factors were estimated across the main climatic regions and subregions of the CONUS to verify if the relations between them is influenced by the climatic conditions of a specific area. A scientific paper presenting the analysis and the results related to this first Research Objective is currently in preparation (Palazzoli et al., in prep.).

The second Research Objective (RO2) of this Thesis attempts to provide an answer to questions (Q2a) and (Q2b). Here, the relation between urbanization and surface water depletion was explored by evaluating the spatial distribution of surface water losses that occurred between 1984 and 2018 as a function of distance from urban areas across the CONUS. Maps of surface water loss locations and built-up areas were created from datasets derived from remotely-sensed data. This analysis consists in an innovative application of the distance-decay concept to evaluate and analytically reproduce the influence of urban areas on the spatial distribution of surface water loss across the CONUS. Moreover, as for RO1, the influence of climate was analyzed to possibly identify distinct signatures of the spatial distribution of surface water losses from human settlements within the main climatic regions of the study area (Palazzoli et al., 2022).

An accurate understanding of (i) the contributing factors to a change in surface water extent and (ii) the dynamics of the spatial interaction between urban areas and surface water loss distribution is fundamental to define ecologically sustainable solutions that ensure water conservation and ecosystem protection, with an emphasis on those strategies that allow to meet urban water demand and at the same time prevent the depletion of surface water resources (McDonald et al., 2011c; Lyons, 2014; Grizzetti et al., 2017; Boretti & Rosa, 2019; Paiva et al., 2020).

1.2 Outline of the Thesis

The present Thesis report comprises six chapters, which are structured in the following way.

Chapter 1 (i.e., the current one) is a general *introduction* to the study framework, specifying the objectives and methodology of the research, and the executive summary.

Chapter 2 reviews the *scientific literature* related to the subject matter of this dissertation. First, it explains the importance of surface water resources for humans and the environment. Afterwards, it provides information about the impacts of human activities and climate change on surface waters. Finally, remote sensing technique and its application of the detection of surface water, human dynamics, and climate is illustrated in the fourth section.

Chapter 3 describes the *study area* and the collection and processing of *data*. In particular, the currently available datasets derived from satellite and ground-based observations and adopted for data extraction in order to create the maps employed in RO1 and RO2 are presented.

Chapter 4 treats in detail the study of the *influence of anthropogenic and climatic factors on the variation of surface water extent* at the river basin level across the contiguous United States (CONUS) from 1984 to 2020 (i.e., RO1). Starting from the main motivations, the Chapter then describes the employed data and the designed and adopted methodology, and finally discusses the achieved results.

Chapter 5 deals with the analysis of the *spatial distribution of surface water losses as a function of distance from urban areas* (i.e., RO2). This Chapter presents a structure similar to the previous one.

Chapter 6 concludes the dissertation by summarizing the overall findings and the critical issues of the study. It also provides starting points and suggestions for further research.

2 Literature review

2.1 Surface water

Surface water resources represent any water body that is above the ground, including streams, rivers, lakes, ponds, reservoirs, wetlands, glaciers, and ice-caps (Dooge, 2009; Huang et al., 2018), which are vital sources for the maintenance of ecosystems and for socio-economic development (FAO, 2017). Freshwater represents 2.5% of the total amount of water on Earth and is mostly stored in glaciers and groundwater, meaning that humans have access to a very limited amount of it, as shown in Figure 2.1 (Oki & Kanae, 2006; Regan, 2012). Water is naturally recycled within the water cycle: evaporation converts water from liquid to gas, which then recondenses into a liquid, while also water becomes carbohydrates when assimilated by vegetation through photosynthesis, it ultimately reverts to the liquid state via decomposition (Oki & Kanae, 2006). This cycle makes freshwater a renewable resource with a rate of renewal that depends on climate, limiting the quantity of freshwater available to human society. For instance, water in rivers is renewed on average every 16 days, while the largest lakes have a renewal period ranging from hundreds to thousands of years. When surface waters are withdrawn and used with a rate that is higher than their renewal rate, they become non-renewable, eventually causing water scarcity, which is a condition that occurs when water supply is insufficient to meet water demand. Therefore, it is necessary to define more efficient water management solutions that control the impacts of a steadily growing water demand (Shiklomanov, 1993; Oki & Kanae, 2006; Hoogeveen et al., 2015; Wada et al., 2016).

From local to global scale, surface waters sustain and preserve the biodiversity of aquatic and terrestrial ecosystems, supply water to societies as well as guarantee economic growth by providing water to agriculture and industry (Huang et al., 2018; Wang et al., 2018, 2020; Xiong et al., 2018; Cooley et al., 2021). However, global freshwater availability is changing and population growth, human activities, and climate change stress the need to contain water consumption under sustainable levels, in order to avoid water scarcity, and the resulting ecosystems degradation and impacts on technological progress and environmental security (Kummu et al., 2016; Rodell et al., 2018; FAO, 2020). Currently, the annual water withdrawals are equal to 3800 km^3/year, while the annual discharge of water that flows from land to the sea through the rivers is 45,500 km^3/year, with the latter giving an estimate of water availability (Oki & Kanae, 2006). Human-induced and natural factors reshape surface water bodies, by shrinking and expanding their extent, or moving their location with time (Huang et al., 2018). As a result, nowadays two-thirds of aquatic habitats are facing many challenges and they are threatened by future variability of precipitation patterns and river discharge. Furthermore, about 5 billion people live in areas that are already experiencing water shortages and that are exposed to a higher risk of water scarcity because of future scenarios of population growth and climate change (Rodell et al., 2018). Therefore, the impacts on both the environment and human communities make critical the detection of the location, extent, and volume of surface waters and the monitoring of their dynamics (Huang et al., 2018; Wang et al., 2018).

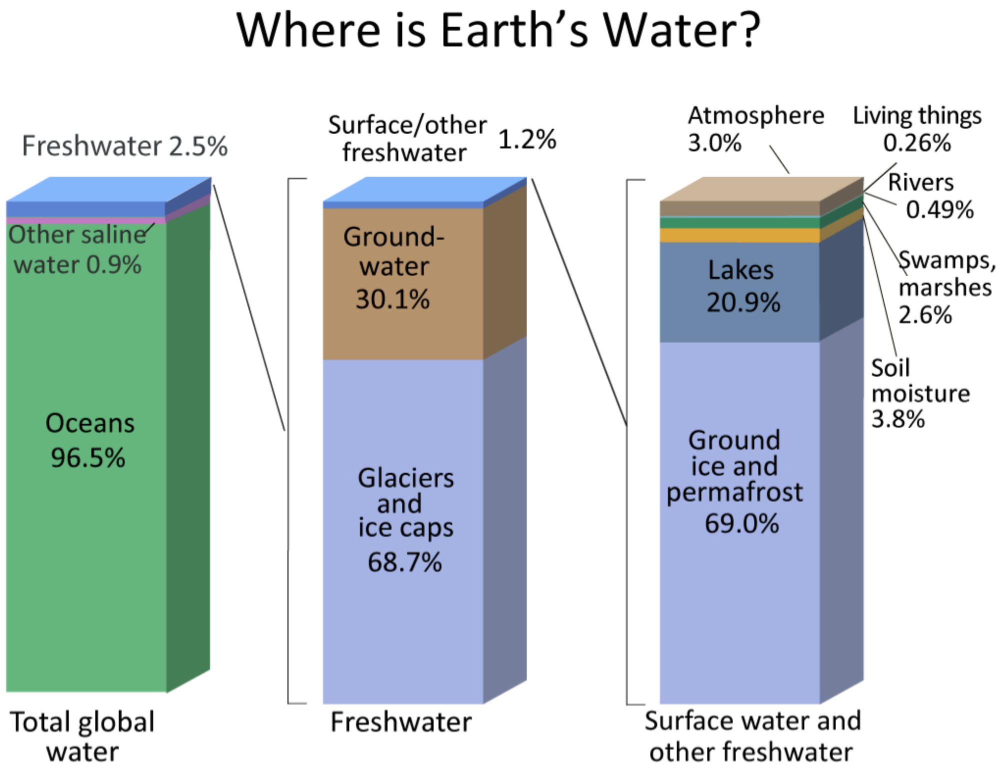

Figure 2.1 Bar chart showing the distribution of Earth's water (numbers are rounded). The left-side bar chart shows all water (saline and freshwater) on, in, and above the Earth. The central bar shows the distribution of all freshwater. The right-side bar shows the portion of freshwater found in surface water, snow, ice, and relatively-shallow ground water. Source: Igor Shiklomanov's chapter "World fresh water resources" in Peter H. Gleick (editor) 1993, Water in Crisis: A Guide to the World's Fresh Water Resources (Shiklomanov, 1993).

2.2 Human pressure on surface water

Through history humans have learnt how to control and exploit water resources exerting a critical and constantly increasing pressure on hydrology (Vörösmarty et al., 2004; Bierkens, 2015; Ceola et al., 2015; Wada et al., 2017). Specifically, the terrestrial water cycle has been rapidly disrupted through direct actions, such as water diversions and withdrawals, and through indirect effects due to, e.g., land cover change and human-induced climate change (Rost et al., 2008). The global demand for water is strongly affected by growing population, urbanization, economic development, and food security policies. Water demand is currently growing at a rate of 1% per year (UNESCO, 2020), while two-thirds of the world population is experiencing water scarcity from 1 to 12 months per year as shown in Figure 2.2 (Mekonnen & Hoekstra, 2016). By 2050 the manufacturing, thermal electricity generation, and domestic use are expected to produce a 55% increase of water demand (WWAP, 2015). Under this scenario, rivers and lakes are highly exposed to the risk of overexploitation and depletion, since they represent, together with groundwater, the main water source for anthropogenic uses (Shiklomanov, 1993; Ceola et al., 2019).

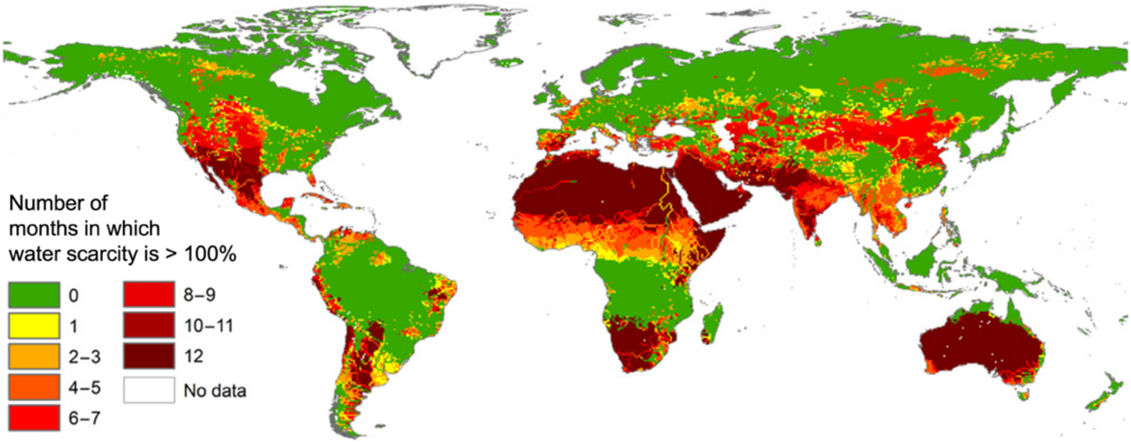

Figure 2.2 Number of months per year during which water scarcity exceeds 1.0 (data over the time period 1996-2005). Figure taken from Mekonnen & Hoekstra (2016).

Since water is mainly withdrawn for agricultural, industrial, and domestic purposes (Regan, 2012; Flörke et al., 2013), the present analysis examines the anthropogenic effects caused by irrigation, urbanization, and population dynamics.

2.2.1 Population growth and urbanization

Demographic expansion and the process of urbanization are among the main anthropogenic factors that modify water flow regimes and rivers morphology, placing a massive stress on river systems (Paterson et al., 2015; Grizzetti et al., 2017; Ceola et al., 2019). In addition, industrial and domestic sectors are globally responsible for the 19% and 11% of the total anthropogenic use of freshwater, respectively (Flörke et al., 2013).

The past century witnessed a global increase of population living in cities, which starting from 2007 exceeded the number of people residing in rural areas, as shown in Figure 2.3 (United Nations, 2019). Specifically, in 1900 about 16% of the global population, corresponding to 0.3 billion people, was living in urban areas, whereas in 2010 urban population became more than half of the world's population with 3.5 billion people (Kummu et al., 2011). Currently, 55% of the global population is urban and this fraction is set to progressively increase reaching almost 70% by 2050 (Paterson et al., 2015; United Nations, 2019). In particular, by 2030 people living in urban areas are expected to constitute 83% and 53% of the total population in developed and developing countries, respectively (McGrane, 2016). This rapid growth of urban population is associated to the expansion of existing cities and the development of new urban areas. This is accompanied by an increase in global urban water demand, which in turn alters hydrologic balances of basins providing and receiving freshwater supplies (McDonald et al., 2014; Padowski & Gorelick, 2014). In 2050 water demand in urban areas is projected to reach an increase of 50-80%, amplifying the competition for freshwater among cities and between urban areas and the agricultural sector (Garrick et al., 2019).

Human settlements usually develop along rivers as they supply water for different uses, such as drinking water, irrigation, transportation, and power purposes (O'Driscoll et al., 2010; Kummu et al., 2011; Everard & Moggridge, 2012; Ceola et al., 2015; Fang & Jawitz, 2019). The development of new urban areas determines considerable changes of local water resources, such as the increase of impervious surface area, channels alteration, interruption of rivers and floodplains, high water demand, and the introduction of new pollutants that deteriorate water quality. Consequently, streams and rivers gradually disappear causing a widespread degradation of freshwater ecosystems (Everard & Moggridge, 2012; Ceola et al., 2015; Kaushal et al., 2017). In particular, the expansion of the total impervious surfaces influences surface water availability through an increase of the surface runoff and a drop of infiltration, producing earlier peaks in river discharge with respect to rainfall events. These effects determine a higher risk of floods, as well as droughts due to reduced groundwater recharge (Everard & Moggridge, 2012; Bhaskar et al., 2020). Moreover, urbanization affects the distribution of surface water through direct water abstraction from springs and rivers (Flörke et al., 2018), groundwater exploitation turning into increased infiltration (Wada et al., 2012), land drainage supporting agricultural development (Smedema et al., 2000), and increased evaporation induced by the urban heat island effect (Zhou et al., 2015).

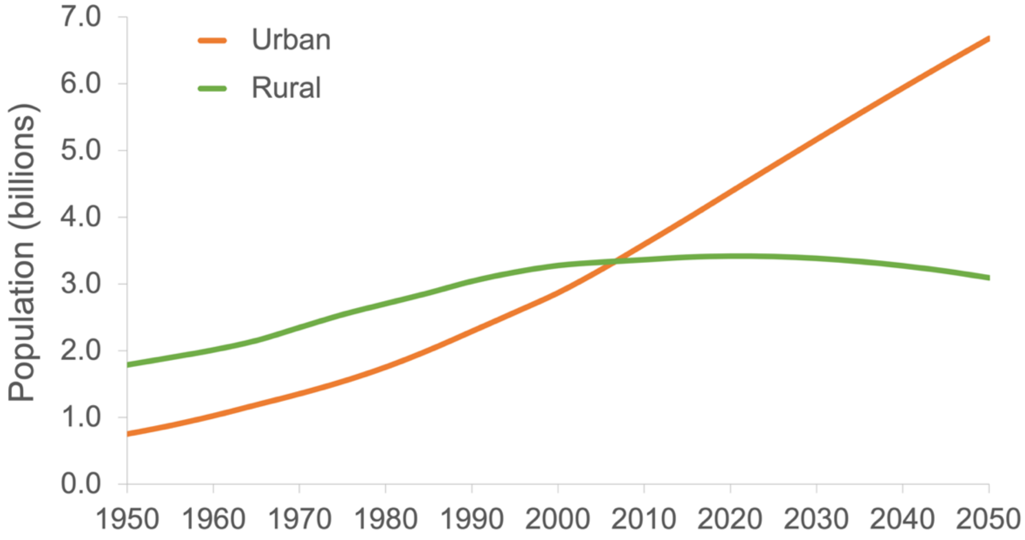

Figure 2.3 Trends of urban and rural population of the world from 1950 to 2050. Data source: United Nations, Department of Economic and Social Affairs, Population Division (United Nations, 2019).

Urban water demand is spatially concentrated within a small and highly-dense area with thousands or millions of people. Even though infrastructures allow cities to reach sources of surface water and groundwater that are far away from the urban area, urban water demand usually relies on local freshwater sources that are found near the city center (McDonald et al., 2014). As a result, a reduction in the extent of surface water bodies close to cities reflects an anthropogenic overstress on water resources which might lead to a condition of water scarcity in the future (McDonald et al., 2014).

2.2.2 Irrigation

The practice of irrigation consists in the full or partial artificial application of water (including both surface water and groundwater) to counteract the precipitation deficit during the crop growing season (Ozdogan et al., 2010). Irrigated agriculture allows to guarantee food security even under the most demanding conditions induced by the economic and demographic growth and climate change (Bekele et al., 2019; Zohaib & Choi, 2020). Indeed, although irrigation covers only 20% of the total cultivated land, it sustains 40% of the global food production as it produces at least twice the crops per unit of land coming from rainfed agriculture (World Bank, 2021). Besides increasing soil productivity, the benefits coming from the adoption of irrigated agriculture are longer growing seasons and the possibility to select crop types.

Most of the global water withdrawals is destined to the food production system and in particular to irrigation (Dang et al., 2015). However, after land area, water represents the second most limiting factor for food production and its supply largely influences crop yield (Nair et al., 2013). As a result, the agricultural sector is at the same time a cause and a victim of water scarcity, as it is responsible for 70% of global freshwater withdrawals from rivers, lakes, and aquifers, and for more than 90% of consumptive use (i.e., nonrecoverable water) due to the evapotranspiration of crops, while it is also extremely sensitive to water shortages (FAO, 2012; Hoogeveen et al., 2015; Wada et al., 2016). The impacts of irrigation withdrawals on surface water availability and quality have been observed also in humid regions (Nie et al., 2021). In particular, Figure 2.4 depicts that the water stress per major river basin at the global scale, which is expressed as a percentage of incremental evaporation due to irrigation over the outflows generated from groundwater (effluent discharge) and surface water (runoff) resources, is higher in correspondence of some of the world's top cereal producing areas (Hoogeveen et al., 2015). Increasing food demand due to economic and world population growth requires an agricultural expansion, inducing extensive water abstractions, especially in arid and semi-arid regions, which are likely to experience water scarcity (Anderson et al., 2012; Starr & Levison, 2014; FAO, 2020).

Crop water requirements vary among crops and geographical regions, depending on soil moisture levels, influenced among all by rainfall patterns, temperature, soil type, and vegetation (Pimentel et al., 1997). For ideal growing conditions, soil moisture in the root zone should be at least 50%, which requires artificial irrigation. Therefore, irrigated agriculture is considerably sensitive to climatic conditions and future climate variability is expected to remarkably impact irrigation as it will affect hydrological regimes and water availability (FAO, 2012). Furthermore, the consumption of surface water resulting from irrigation practices has consequences on regional climate, ecosystems, and human health (Anderson et al., 2012). Hence, human pressure along with droughts and the reduction of water supplies caused by climate change are enhancing competition for water resources and they will lead to an extensive water use for irrigation, as the irrigated food production will increase by more than 50% by 2050 (Mancosu et al., 2015; FAO, 2017; Nie et al., 2021). In particular, water shortages and scarcity will be amplified in some regions (arid regions) while they will start to appear in some other areas that currently have a sufficient amount of water resources (Pimentel et al., 1997; FAO, 2012).

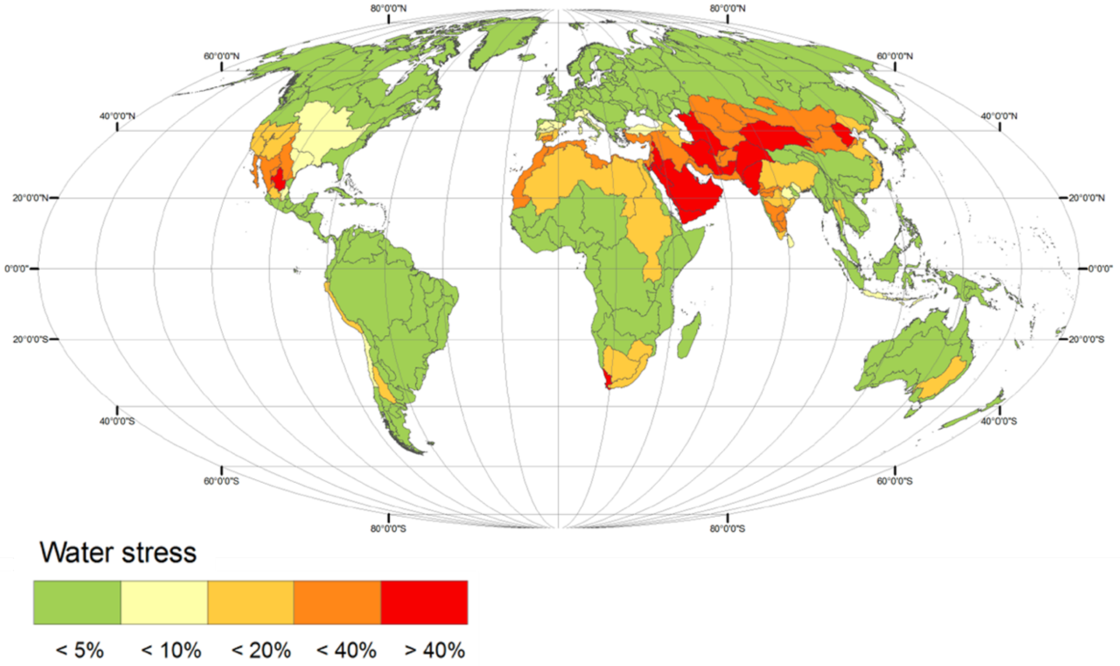

Figure 2.4 Water stress of the major river basins expressed as a percentage of incremental evaporation due to irrigation over the outflows generated from groundwater and surface water resources. Figure adapted from Hoogeveen et al. (2015).

2.3 Effects of climate change on surface water

Warming climate is one of the drivers of water stress, as it causes spatiotemporal variations of precipitation, temperature, and evapotranspiration (ET), which in turn affect river runoff and groundwater recharge, posing a threat to water security (Kundzewicz, 2008; Duan et al., 2019). In particular, climate change increases the frequency of hydrologic extreme events, such as flood and drought, producing a decrease of water supplies and a growth of water demand (Zhuang et al., 2018; Brown et al., 2019a). Moreover, the changes in climatic variables influence and interact with each other. Indeed, the difference between precipitation and ET determines the amount of local water that is accessible at the watershed level. However, as temperature rises ET becomes more intense, drying surfaces, reducing soil moisture and surface waters (Duan et al., 2019).

Future climatic changes are predicted to considerably affect the global hydrologic regimes, by modifying the amount, distribution pattern, and timing of water availability, with the most sudden water cycle changes occurring under high emission scenarios (McDonald et al., 2011c; Zhuang et al., 2018; Petpongpan et al., 2020; IPCC et al., 2021). Overall, projections of future precipitation anticipate a reducing trend in semi-arid regions, rising trend in temperate regions, more frequent extreme events, and a higher variability in rainfall distribution, whereas greenhouse gas emissions are expected to raise temperature globally, and the greatest variations are projected in the poles rather than at the equator (McDonald et al., 2011c; FAO, 2012). In order to prevent severe water shortages, beside mitigation strategies restraining human-induced climate change in the future, there is the need to employ proper adaptation solutions that are able to take advantage from the hydrologic changes that already took place and that are expected to intensify in the future. These adaptation solutions include both the improvement of water supply and the reduction of water demand (Brown et al., 2019a).

2.3.1 Precipitation change

Precipitation is the main source of water body on land (Kundzewicz, 2008). As a result, surface water as well as the whole hydrologic cycle are extremely sensitive to precipitation variability and extreme events, such as floods and droughts, which are a consequence of warming climate (Kifle Arsiso et al., 2017; Pendergrass et al., 2017; Brunner et al., 2021; McKinnon & Deser, 2021). On one hand, heavy rainfall produces extreme runoff or flooding. On the other hand, scarce rainfall determines a decrease of water level in water bodies (both surface water and groundwater), a decline in soil moisture, and droughts (Kundzewicz, 2008). Specifically, drought is a slow process that progressively reduces the amount of water stored in soil, decreasing springs, reservoirs, and aquifers, and it can last for years or even centuries. Figure 2.5 shows that the global annual precipitation anomaly generally increased during the last decade, although it did not present a defined pattern from 1901 and 2020.

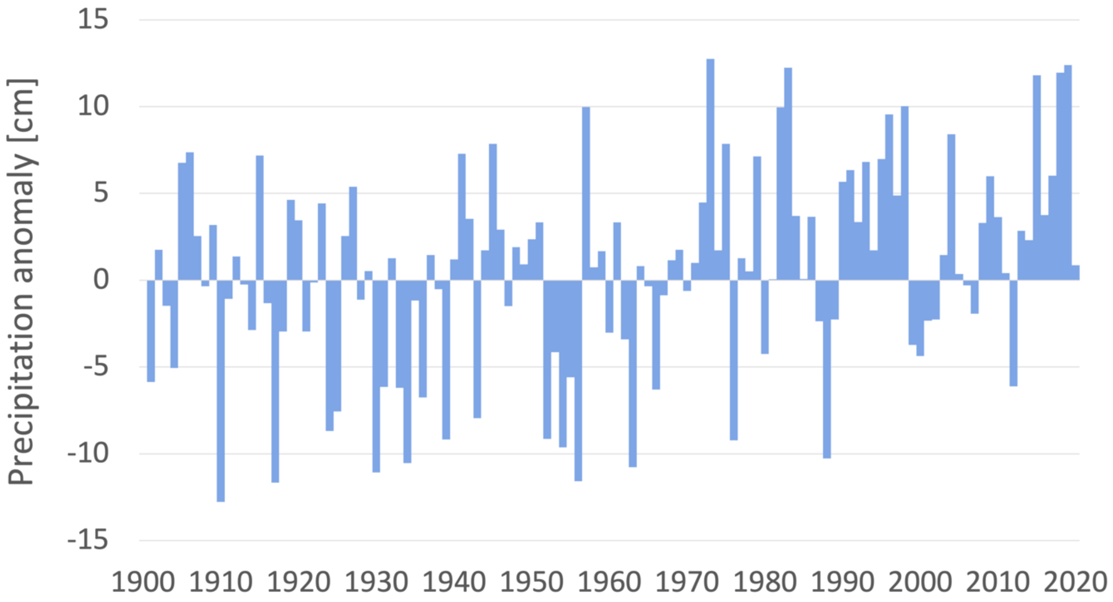

Figure 2.5 Global annual precipitation anomaly compared to the average precipitation from 1901 to 2020 based on rainfall and snowfall measurements collected at weather stations worldwide. Data source: National Oceanic & Atmospheric Administration (NOAA) via the US EPA (EPA, 2016).

Droughts are particularly dangerous to humans and natural organisms, in such a way that history is full of drought episodes that modified and devastated entire civilizations and ecosystems (Wanders & Wada, 2015; Van Loon et al., 2016; CRED, 2020). The more the economy is sensitive to water availability variation, the greater the impacts of droughts will be, with contained damages where there is an efficient regional and global trade and when infrastructure networks and institutions allow to easily store, move, and reallocate water. In natural ecosystems droughts promote the establishment of invasive species or shifts in species composition (Lund et al., 2018). Hence, changes in precipitation patterns influence the availability of surface water, causing impacts on both humans and ecosystems (Duran-Encalada et al., 2017; Konapala et al., 2020). In addition, the occurrence of extreme events impacts also the solutions that humans developed to deal with such episodes, for instance droughts involving large areas hinder water management strategies that rely on water transfer from adjacent regions (Brunner et al., 2021).

2.3.2 Temperature change

All the components of the water cycle depend on temperature. Indeed, warming climate affects processes such as precipitation, ET, soil moisture, and river flow. By controlling the evapotranspirative demand, i.e., the evaporation from soils, plants, and trees, and the transpiration process related to the use and release of water from plants, temperature alters water availability (Georgakakos et al., 2014). Rising temperatures determine an increase in the potential ET rates and in the amount of water held in the atmosphere, and this condition of higher atmospheric moisture and temperature will produce more intense precipitation (Kundzewicz, 2008; Balling & Goodrich, 2011). Figure 2.6 shows that temperature has been increasing worldwide since 1976.

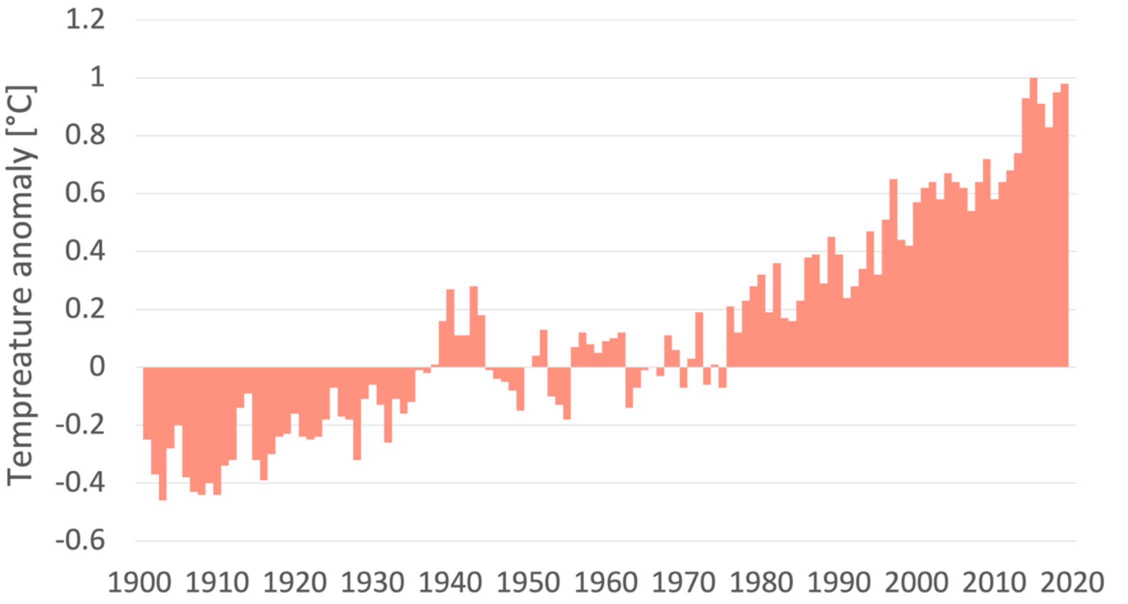

Figure 2.6 Global annual temperature anomaly compared to the average temperature from 1901 to 2020 based on the combination of a set of land-based weather stations and sea surface temperature measurements worldwide. Data source: National Oceanic & Atmospheric Administration (NOAA) via the US EPA (EPA, 2016).

Additional effects due to warming temperature are the glaciers retreat and the reduction of snow cover (Kundzewicz, 2008), as well as the increase in the severity and extent of drought events (Brunner et al., 2021). Moreover, wild fires represent another countereffect of high temperatures, along with earlier springs warming, and dampened surface water (MacDonald, 2010). Finally, long periods characterized by temperature that are above or below normal values, i.e., heat and cold waves, have impacts on both the environment and human activities (Vose et al., 2017), and in the future hot extremes will become more frequent, while there will be a drop in the frequency of cold extremes (Kundzewicz, 2008).

2.4 Remote sensing data

Satellite remote sensing is a powerful tool that has emerged during the second half of the 20th century. The operation of remote sensing is based on the mechanisms of reflection, absorption, and transmission of electromagnetic radiation. The satellite sensor is the instrument that measures and records the radiance, which is the reflected radiation in the direction toward the sensor. Passive sensors use the light emitted by the Sun (passive remote sensing), while active sensors use the light emitted by the satellite itself (active remote sensing), as shown in Figure 2.7.

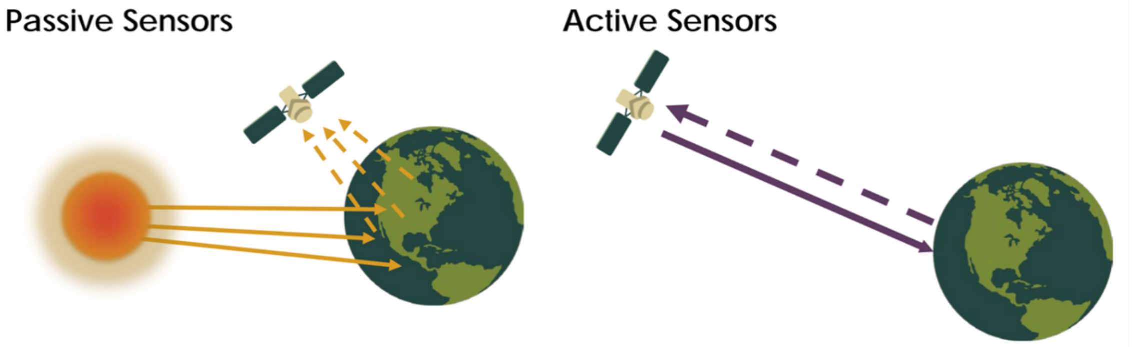

Figure 2.7 Difference between passive and active sensors aboard a satellite. Passive sensors exploit the natural energy of the Sun. Active sensors provide their own energy. Figure taken from https://earthdata.nasa.gov/learn/backgrounders/remote-sensing.

Every feature on Earth reflects, absorbs, transmits, and emits electromagnetic energy and is characterized by a unique spectral signature, which defines the percentage of total radiation that is reflected by a target (i.e., the reflectance) as a function of wavelength (for some examples, see Figure 2.8). Therefore, the various wavelengths of the electromagnetic spectrum associated to the reflected radiation allow to identify features and materials and extract information on terrestrial processes, such as hydrological cycle and vegetation dynamics, that are occurring when the satellite passes over a specific location of the Earth's surface (Karthikeyan et al., 2020).

Remote sensing provides global-scale and freely available Earth Observation (EO) at very high spatial and temporal resolution. For this reason it has been recognized to be the most relevant source of data for the detection and analysis of natural or man-induced changes, which consists in the identification and measurement of significant differences in objects and conditions captured over the same region of interest at different times from the comparison of two or more images (Asokan & Anitha, 2019). The operation of change detection has important implications for resources management and it is particularly useful for the inspection of inaccessible areas (Seydi et al., 2020; Afaq & Manocha, 2021). Therefore, remote sensing plays a key role in monitoring the process of environmental change. Satellite imagery allows to record changes in land use, spatial allocation of human settlements and activities, and climatic variables, which are all major factors in altering water dynamics (Fang et al., 2018; Sheffield et al., 2018; Ceola et al., 2019; Liu et al., 2020). Specifically, once they have been acquired, satellite images are corrected in order to remove unwanted artifacts and noise due to atmospheric interferences (image preprocessing). Afterwards, an algorithm is applied to identify changes and create a map. Several change detection techniques have been defined based on the type of application (Asokan & Anitha, 2019). In what follows a review of the main methods that are generally adopted for the monitoring of surface water resources, human activities, and climatic conditions is presented.

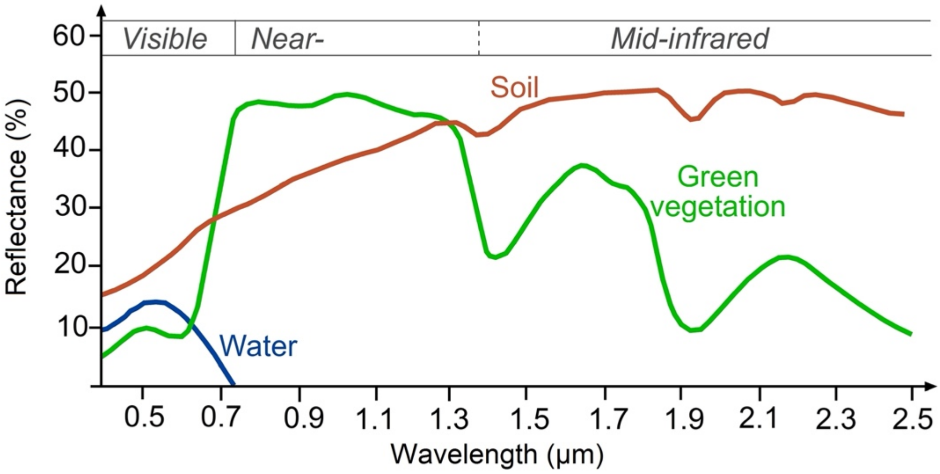

Figure 2.8 Spectral signature showing the reflectance of water, soil, and vegetation at different wavelengths. Figure taken from https://seos-project.eu/classification/classification-c01-p05.html.

2.4.1 Remote sensing of surface water

Satellite data have been widely employed to detect and track surface water extent and its persistence and recurrence, as well as to identify flooded regions and wetlands (Acharya et al., 2016; Huang et al., 2018). The estimation of the spatiotemporal variation of surface water bodies is fundamental to many environmental applications, such as flood prediction, the evaluation of irrigation in agricultural land, and hydropower energy (Acharya et al., 2016; Donchyts et al., 2016). Furthermore, optical satellite imagery supplies relevant information for those areas that are not easily accessible or have a large extent (Mueller et al., 2016). Although several approaches are available for the identification of water bodies from satellite images, the most common is the calculation of spectral indices obtained from the combination of multiple bands whose positive values indicate the presence of water, e.g., the Normalized Difference Water Index (NDWI) and the Modified NDWI (MNDWI). The definition of these indices exploits the capability of water to absorb radiation at near-infrared wavelengths and beyond, which determines very low or no reflection from water in the spectral bands corresponding to these wavelengths (Mueller et al., 2016). Moreover, techniques using information regarding satellite view angle and solar zenith/azimuth are necessary to reduce the errors of commission (i.e., wrong detection of water) due to the noise in the signal produced by the presence of clouds, snow, and ice (Donchyts et al., 2016). Even if spectral indices are largely used in water detection for their simplicity, the definition of a threshold value can be laborious and impractical as the spectral signature of water varies as a function of sediments, algae, depth, and the reflectance signal from the bottom (Tulbure et al., 2016). The most accurate approach to extract water from remotely-sensed data is the supervised or unsupervised classification of multispectral data as they detect statistical pattern, instead of empirical thresholds. When a supervised classification is carried out, a set of representative training samples is employed to train a classifier in the discrimination between spectral signatures of different land cover classes. Therefore, the supervised classification is used when the analyst has a good knowledge of the area. However, this approach presents some issues due to the selection of a proper set of training sites. The unsupervised classification allows to overcome this limitation as it does not require training samples (Chen et al., 2018). Other methods are based on digitizing through visual interpretation, which is highly accurate, but time consuming, and the density slicing on a single band through the application of a threshold applied over a band (Acharya et al., 2016).

The Landsat Thematic Mapper (TM) sensor provides images at 30 m resolution and a 16 days temporal resolution, representing a valuable and the most commonly used product for an accurate and precise detection of surface water bodies and the monitoring of their evolution (Tulbure et al., 2016; Schaffer-Smith et al., 2017). In particular, Landsat images are extensively used in the detection of surface water and, thanks to the launch of Landsat 8 from 2013, the improved Operational Land Imager (OLI) sensor and Thermal Infrared Sensor (TIRS) provide a clearer and more accurate EO (OLI images), with a higher spatial resolution than the previous versions of Landsat. One of the major improvements came from the introduction of two additional bands, the deep blue band (band 1) and the cirrus band (band 9). The deep blue band has a higher sensitivity to chlorophyll and the suspended materials found in coastal waters and it is also able to retrieve atmospheric aerosol properties. The cirrus band supports the detection of cirrus cloud. In addition, the higher values of signal-to-noise ratio (SNR) provided by the two sensors allow to better detect variations in the quality of water, which is an information that otherwise tends to be lost in the noise of the signal (Acharya et al., 2016). Landsat satellite images have been widely used to extract surface water maps (Acharya et al., 2016; Donchyts et al., 2016; Schaffer-Smith et al., 2017; Xiong et al., 2018) and measure its inter- and intra-annual variability (Mueller et al., 2016; Tulbure et al., 2016; Wang et al., 2018). The analysis of over 3 million Landsat satellite images observed from 1984 to 2020 generated the Global Surface Water dataset, a set of maps showing the location, size, and change of surface water bodies at 30 m resolution (Pekel et al., 2016). This dataset is considered to be the best evaluation of surface water dynamics and it documents the loss of almost 90,000 km^2 of permanent surface water on the planet, caused, among all, by drought, climate change, and anthropogenic activities (Pekel et al., 2016; Yamazaki & Trigg, 2016).

2.4.2 Remote sensing of human dynamics

Mapping land cover change as influenced by human dynamics is another core application of remote sensing. Recently, satellite images at very fine spatial resolution have replaced the use of products at coarser (medium-low) resolutions in the description of land cover. Although high and very high resolution (HR and VHR) imagery produce more exhaustive maps, they also introduced some limitations due to the complexity of textures and structural patterns found at this level of detail which are usually solved with the application of the supervised and unsupervised classification techniques (Chen et al., 2018).

Geography defines the term human settlements as any agglomeration of buildings where people live and work. Thus, the presence of buildings represents the core element that characterizes and helps for the identification of human settlements (Florczyk et al., 2020). The extent of human settlements derived from satellite images is employed to identify urban areas, assess their morphology and correlation with socio-economic parameters. Moreover, maps depicting urban change at high spatial resolution are helpful for the analysis of human-induced processes, such as greenhouse gas emissions, urban heat island effect, land use change, urban sustainability, and to determine situations of danger associated to landslides, earthquakes, floods, and other natural hazards (Liu et al., 2020). Urban area maps are used to infer information regarding spatial distribution of population and to calibrate land-use change models (Marconcini et al., 2020). Currently there are several remotely-sensed products depicting the presence of human settlements (Chen et al., 2018; Florczyk et al., 2020; Liu et al., 2020; Bernhofen et al., 2021). For instance, Landsat images coupled with other data, such as population data, MODIS imagery or alternative satellite imagery like the Chinese GF1 and GF2 satellites, have been used to determine the spatial distribution of urban areas and predict its expansion (Bounoua et al., 2018; Xiong et al., 2018; He et al., 2019), to study the conversion from cultivated land into built-up land, and to derive land use/land cover maps (Cai et al., 2019; Yuan et al., 2019). Besides these applications, Landsat images have been further employed to produce the Global Human Settlement Layer (Corbane et al., 2019), the most acknowledged open and free tool capable of capturing the spatial distribution and evolution over time of built-up areas at 30 m resolution (Corbane et al., 2019). This dataset shows that between 1975 and 2015 urban areas expanded by 40%, in terms of both population and built-up surface (Melchiorri et al., 2018). The combination of Sentinel-1 and Landsat-8 multitemporal satellite images was used to generate the World Settlement Footprint (WSF2015), a map of global human settlements of 2015 at 10 m resolution. Finally, another recent layer with a high spatial resolution is the Global Urban Footprint (GUF) showing global settlements of 2012 with a 12 m spatial resolution (Marconcini et al., 2020).

Several studies have demonstrated the potential of remote sensing in the detection of irrigated areas as well, using multispectral and multi-temporal satellite images (Ozdogan et al., 2010; Pageot et al., 2020). Remotely sensed data of irrigated areas represent an alternative resource to the numerous existing maps that have been derived mainly from country-level irrigation statistics and census, such as the Global Map of Irrigated Areas and the MIRCA2000 product provided by FAO (Food and Agriculture Organization of the United Nations) (Ambika et al., 2016; Bazzi et al., 2019). Although the unquestioned capabilities of satellite imagery, until a few years ago the application of this powerful tool to determine irrigated lands, and thus land use, involved a limited number of studies compared to the classical land cover analysis. This is due to the fact that land cover is less difficult to determine than land use, as it does not require the knowledge of land management or the location and timing of irrigation practices. Another limitation of mapping irrigated agriculture with remote sensing data is the identification of small irrigated areas that in total may cover a significant area extent and may thus produce a remarkable amount of water consumption. Moreover, in humid areas the spectral signature of irrigated land and those of non-irrigated land may be the same, and additional information on crop planting, maturity, and harvest are needed (Ozdogan et al., 2010). However, in-situ observations are not able to monitor high spatial and temporal variability and this issue has favored a more frequent application of satellite images in this field (Karthikeyan et al., 2020). Many studies have been carried out on the use of remote sensing data for the definition of maps of irrigated land (Bastiaanssen et al., 2000; Ambika et al., 2016; Bazzi et al., 2019; Coleman et al., 2020; Graf et al., 2020; Dari et al., 2021). Some applications have proved that the joint use of different types of data can improve the accuracy of the classification of irrigated land. For instance, Demarez et al. (2019) combined the radar Sentinel-1 images, the optical imagery of Landsat8, and the digital elevation model of the Shuttle Radar Topography Mission (SRTM) to identify irrigated crops and found that this combination produces much more robust products compared to those obtained from the use of optical images alone. Also Pageot et al. (2020) discovered that the combination of optical and radar data from Sentinel-1 and Sentinel-2 together with meteorological time series yields superior results in the discrimination between irrigated and rainfed areas.

2.4.3 Remote sensing of climate variability

Satellite imagery offers the possibility to observe some of the components of the water cycle and measure hydrological fluxes and their spatio-temporal variability. In particular, satellite observations improve the quantification and prediction of precipitation, which is a crucial climatic variable of the water cycle (Hong et al., 2018; Levizzani & Cattani, 2019). Currently, rain gauges, satellite retrieval, and reanalysis are the main approaches employed to estimate precipitation with global coverage. Although each of these techniques has its own set of merits, satellite-based remote sensing technology presents the great potential to cover broader spatial extent and monitor large scale events (Chen et al., 2020; Xu et al., 2020). Another advantage of satellite sensors is that they provide accurate, continuous, and uniform observations, while avoiding the high cost of ground observation networks (Hong et al., 2018). Levizzani & Cattani (2019) extensively reviewed the current status of remote sensing of precipitation demonstrating that it has the potential to improve our knowledge of the processes involved in the water cycle and the monitoring of climate change, supporting the existing systems of in-situ observation. Some examples of satellite precipitation products are the Tropical Rainfall Measuring Mission (TRMM), which provides midlatitude precipitation at 0.25° spatial resolution since 1998, the Multi-satellite Precipitation Analysis (TMPA) and the Global Precipitation Measurement (GPM) products that produce global near-real time precipitation estimates every 30 minutes at 0.1° spatial resolution since 2014, and the Integrated Multi-satellitE Retrievals of GPM (IMERG) (Wang & Xie, 2018). In addition, the merging of satellite sensors and ground precipitation observations along with machine learning and geostatistics techniques helps the prediction of precipitation patterns (Varouchakis et al., 2021).

Remote sensing observations help the estimation of land and air temperature as well. Land surface temperature (LST) is a major driver of global climate changes and Earth's energy budget, as its variation may determine an increase or decrease of atmospheric temperature. Over the past decade a lot of progress has been achieved in the retrieval of LST from satellite sensors and currently several products of LST at regional and global scale have been derived from MODIS and Landsat images, which supply estimations at higher spatial resolution (Ermida et al., 2020; Firoozi et al., 2020; Prakash & Norouzi, 2020; Zhang et al., 2021). Air temperature is a fundamental climatic parameter as well, governing and influencing many hydrological processes. Weather stations have been traditionally used to measure air temperature, but they produce sparse and insufficient data, requiring a spatial interpolation method to derive spatially continuous data over large areas. Thanks to the strong correlation between LST and air temperature, it is possible to estimate air temperature from satellite-derived LST (Li & Zha, 2019; Collados-Lara et al., 2020; Shen et al., 2020). In addition, LST data obtained from satellite sensors are often used to quantify and map the urban heat island (UHI) effect in urban environments (Faroughi et al., 2020; Venter et al., 2020).

Despite the discussed improvements that the application of satellite images has brought to the measurement of climatic variables, in this Thesis precipitation and temperature data were derived from datasets developed with in-situ observations for spatial and temporal coverage reasons (i.e., data across the CONUS from 1984 to 2020).

3 Study area and data

3.1 The contiguous United States

The contiguous United States (i.e., the area including the lower 48 states in North America, also known as the CONUS) is selected as the study area for this analysis because it encompasses an extensive and heterogeneous territory, characterized by broad topographic variations, wide-ranging surface water area extents, diverse urbanization levels, and it is exposed to different hydroclimatic conditions, including both wet and dry regions. The Köppen-Geiger climate classification system defines the main climatic zones across the globe, based on threshold values and the seasonality of monthly air temperature and precipitation. The most recent version of this climate classification system is available at 1 km spatial resolution (Beck et al., 2018), where five main climatic regions and 30 sub-types are identified, out of which 22 are found within the area of the CONUS (Figure A1). Most of the CONUS lies on the continental (40.47%), arid (33.67%), and temperate (25.41%) climatic regions, while a small fraction is characterized by a tropical (0.27%) and polar (0.18%) climate (Figure 3.1).

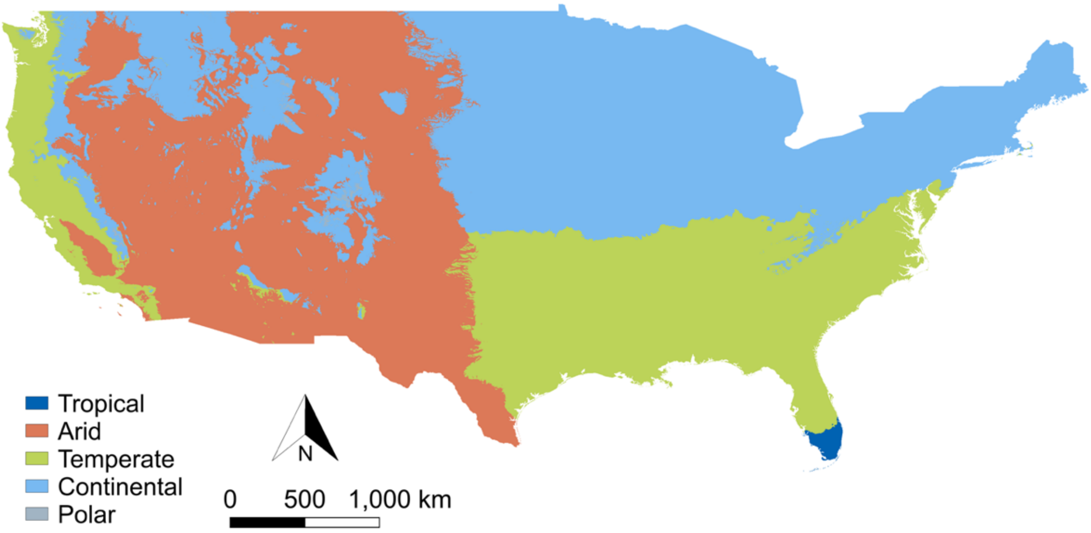

Figure 3.1 Main climatic regions of the Köppen-Geiger climate classification system found within the CONUS.

Beyond the characteristics described so far, another reason that motivates the choice of the CONUS for this analysis is the availability of a profuse amount of data in this region, which allows to conduct an in-depth study of the influence of anthropogenic and climatic drivers on surface water resources (Di Baldassarre et al., 2021).

Following the delineation of the hydrologic units provided by the USGS (Seaber et al., 1987), the CONUS includes 18 water resource regions (WRRs) containing 204 river basins (i.e., 4-digit hydrologic units, HUC-4s, also known as subregions), as shown in Figure 3.2. The 18 water resource regions represent geographic areas corresponding to either the drainage area of a major river (e.g., the Missouri region) or the combined drainage areas of a series of rivers (e.g., the Texas-Gulf region, which contains some rivers draining into the Gulf of Mexico). Whereas, the 204 river basins (subregions) are defined as areas drained by a river system, a reach of a river and its tributaries in that reach, a closed basin(s), or a group of streams forming a coastal drainage area (Seaber et al., 1987).

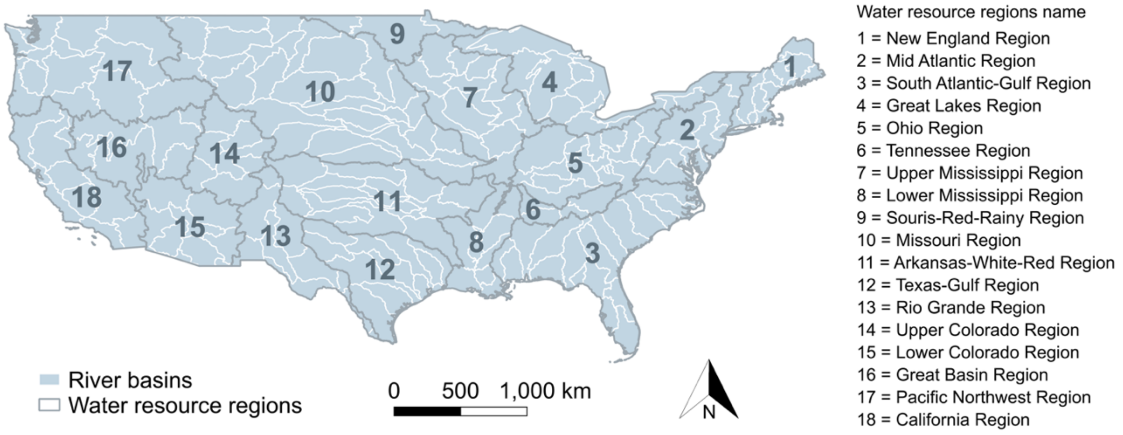
1
2
3
4
5
6
7
8
9
10
11
12
13
14
15
16
17
18
River basins
Water resource regions
0 500 1,000 km
N
Water resource regions name
1 = New England Region
2 = Mid Atlantic Region
3 = South Atlantic-Gulf Region
4 = Great Lakes Region
5 = Ohio Region
6 = Tennessee Region
7 = Upper Mississippi Region
8 = Lower Mississippi Region
9 = Souris-Red-Rainy Region
10 = Missouri Region
11 = Arkansas-White-Red Region
12 = Texas-Gulf Region
13 = Rio Grande Region
14 = Upper Colorado Region
15 = Lower Colorado Region
16 = Great Basin Region
17 = Pacific Northwest Region
18 = California Region

Figure 3.2 Area of the contiguous United States with its 18 water resource regions (WRRs) and 204 river basins.

3.1.1 Surface water in the contiguous United States: supply and demand

Surface water availability remarkably varies across the US, with significant differences between western and eastern regions. Indeed, fresh surface water is largely available in the East, especially in correspondence of the major rivers (such as the Mississippi, Ohio, Missouri, Delaware, Susquehanna, and Tennessee Rivers), while the West is characterized by few river systems (e.g., Colorado River, Rio Grande, Sacramento-San Joaquin, Columbia Rivers) that drain about 66% of the entire region and encompass vast areas with limited surface water availability because of the arid climate and the massive use of water for irrigation, as shown in Figure 3.3 (Dettinger et al., 2015; Tidwell et al., 2017). An overall decline in surface water supply has been observed and is expected to continue in the future, especially in the southwestern US where the availability of surface water is a function of both policies and physical processes. This will put under water shortages some sectors that are highly reliant on freshwater, contrasting the positive effects resulting from improved water use efficiency (Averyt et al., 2013).

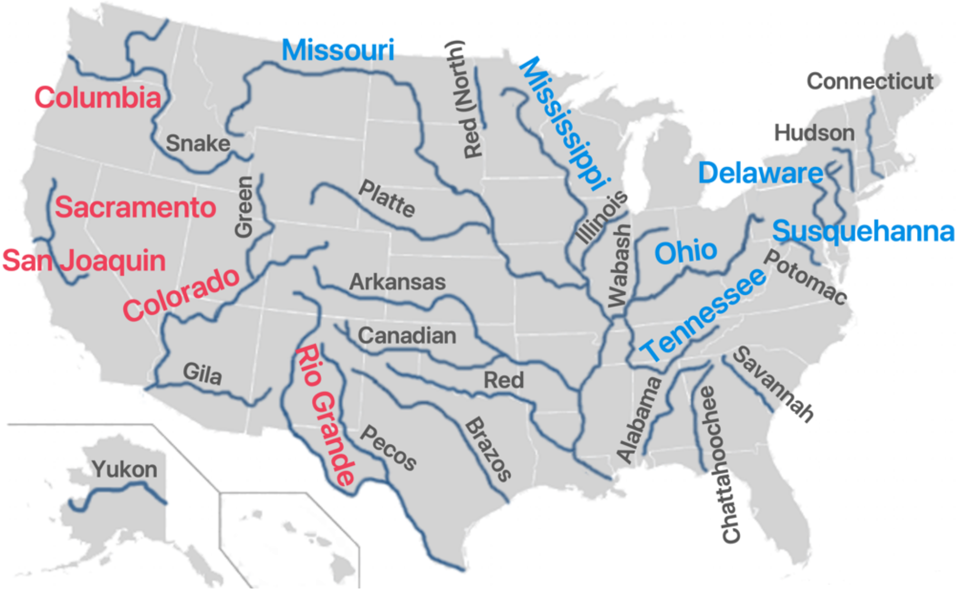
Missouri
Columbia
Snake
Red (North)
Mississippi
Connecticut
Hudson
Delaware
Sacramento
Green
Platte
Illinois
Susquehanna
San Joaquin
Colorado
Arkansas
Wabash
Ohio
Potomac
Tennessee
Canadian
Rio Grande
Gila
Red
Savannah
Alabama
Chattahoochee
Pecos
Brazos
Yukon

Figure 3.3 Main river systems of the United States. Major rivers of the West are highlighted in red, while major river systems of the East are highlighted in blue.

In the United States surface water represents the main source of water withdrawals, accounting for more than 70% of total freshwater supply. In 2015, surface water withdrawals were approximately equal to 237,000 Mgal/day (out of which 84% came from freshwater sources) and they contributed 61% of the total public-supply withdrawals, 99% of the total thermoelectric-power withdrawals, 82% of the total self-supplied industrial withdrawals, and 52% of the total irrigation withdrawals. Moreover, surface water withdrawals exceeded those of groundwater for all anthropogenic uses, with the exception of domestic, livestock (i.e., watering, feedlots, dairy operations, and other on-farm needs), and mining sectors. The largest withdrawals of surface water were observed in Texas, Idaho, Florida, California, and New York, where they constituted around 25% of the total national withdrawals (Figure 3.4).

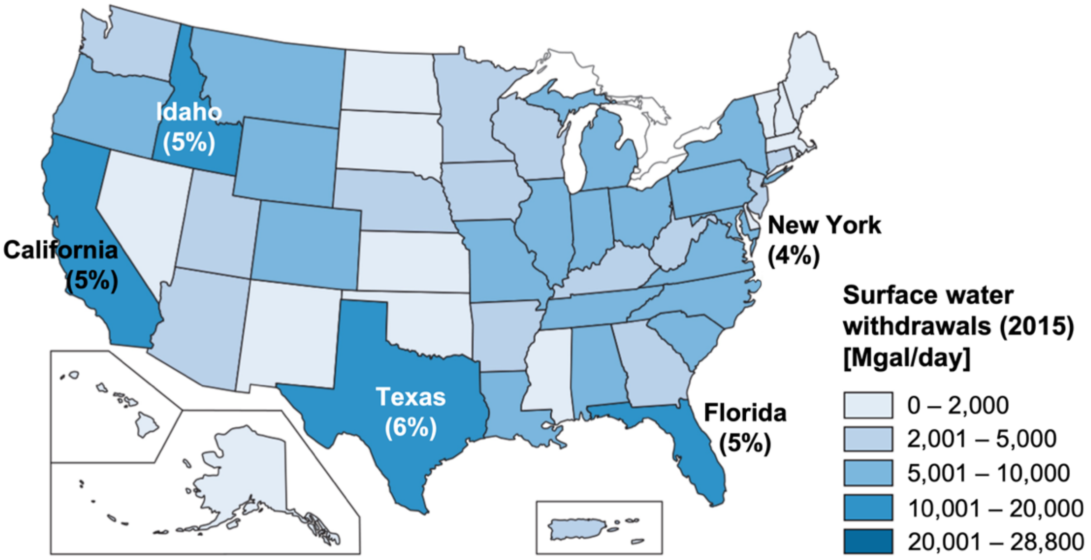

Figure 3.4 Map of surface water withdrawals in the United States in 2015, indicating top 5 states (and their percentage of total withdrawals) that were responsible for the largest withdrawals. 1 gallon corresponds to approximately 4.55 liters. Figure adapted from Dieter et al. (2018).

Surface water represents the primary source of water employed in irrigation systems in the US, especially in the western states, although its use in this sector decreased from 66% of 1985, to 57% in 2010, and lastly to 52% of 2015 thanks to more efficient irrigation systems. Between 1985 and 2010, most of the irrigation water was supplied by surface-water sources, ranging from 66% in 1985 to 57% in 2010. During the period 2010-2015 a decrease in surface water withdrawals has been observed, especially in California, Texas, Ohio, Illinois, Pennsylvania, and North Carolina, which determined more than two-thirds of the total surface-water withdrawal drop (Dieter et al., 2018). Figure 3.5 shows the count of years during which each pixel of the map (250 m spatial resolution) has been observed to be irrigated over the years 2002, 2007, 2012, and 2017, highlighting five areas characterized by various levels of irrigation frequency. Specifically, most of the major irrigation-dominated areas across the CONUS are found to be located in the central valley of California, the Snake River Basin in Idaho, the Columbia Basin of the interior Northwest, the Ogallala Aquifer in the central Plains, and the Mississippi Flood Plains, while more sparsely scattered irrigation is located along the east and southeast coasts (Pervez & Brown, 2010).

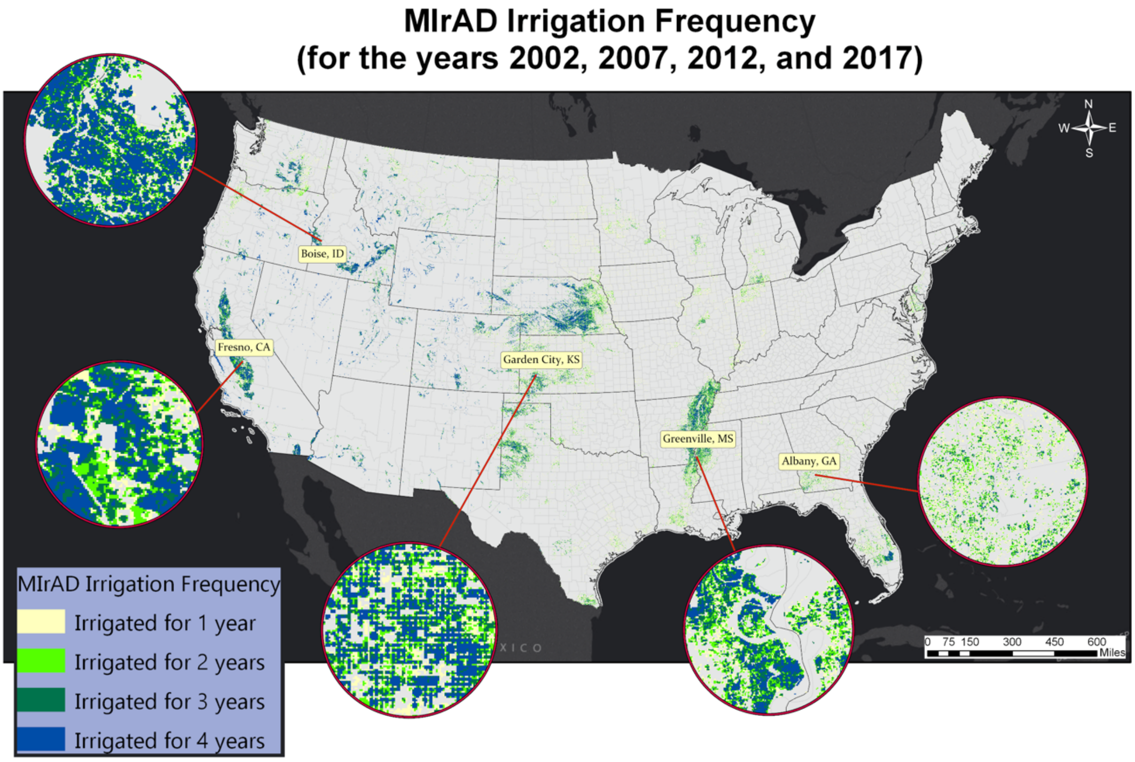
MIrAD Irrigation Frequency
(for the years 2002, 2007, 2012, and 2017)
N
W
E
S
Boise, ID
Fresno, CA
Garden City, KS
Greenville, MS
Albany, GA
MIrAD Irrigation Frequency
Irrigated for 1 year
Irrigated for 2 years
Irrigated for 3 years
Irrigated for 4 years
0 75 150 300 450 600
Miles

Figure 3.5 Frequency of irrigation in the United States in 2002, 2007, 2012, and 2017 obtained from the Irrigated Agriculture Dataset for the United States product (MIrAD-US). Circles show zoom in of areas that have been irrigated more frequently. Figure adapted from https://www.usgs.gov/media/images/mirad-irrigation-frequency-years-2002-2007-2012-and-2017.

Even though over the past decades there has been a growth of US urban population (Figure 3.6), per capita water usage by the agricultural and municipals sectors declined, such that total water use (i.e., water withdrawals and consumption) remained stable around the level of 1985 (Averyt et al., 2013; Dettinger et al., 2015). In particular, fresh and saline surface water withdrawals dropped by 14% between 2010 and 2015 (Dieter et al., 2018). However, water demands may evolve in the future depending on economic, social, and technological scenarios as well as legal and policy factors and climate change. In the United States urban areas have been generally developed adjacent to major rivers and, with more than 80% of population currently living in US cities (Figure 3.6), urbanization places an enormous pressure on surface water resources (Sun & Caldwell, 2015; Fang & Jawitz, 2019).

Pekel et al. (2016) observed that even if surface water area across the US increased on average by 0.5% since 1984, growing water demands and drought conditions determined a 33% loss of the extent of surface water resources in the western region (i.e., in Arizona, California, Idaho, Nevada, Oregon, Utah). Furthermore, southern US is among the most urbanized area of the country because of its high population growth rate, and this process is responsible for hydrological changes in the watersheds of this area (O'Driscoll et al., 2010). Future socio-economic and climate scenarios will likely exacerbate this situation (Yigzaw & Hossain, 2016; Baldocchi et al., 2019; Brown et al., 2019a; Li et al., 2020), as population increase is expected to cause a significant gap between water demand and supply in the future (Daher et al., 2019), while increasing temperatures will likely impact the hydrological cycle and water balance (Brown et al., 2019a).

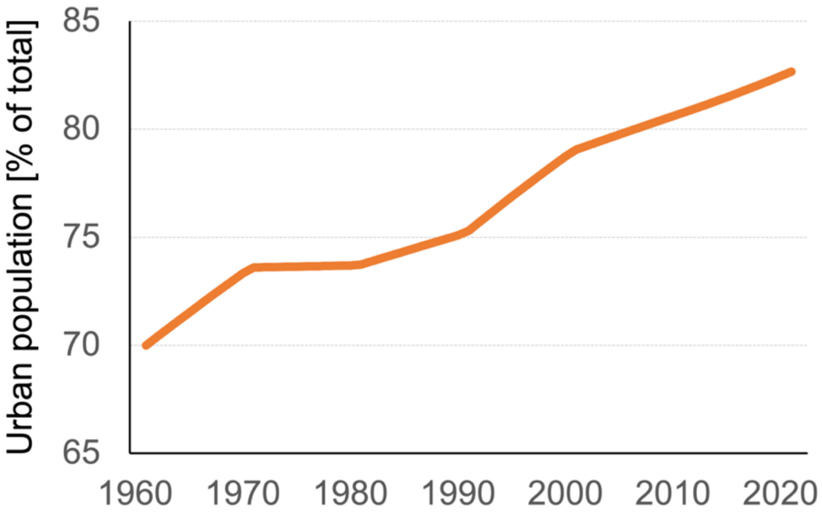

Figure 3.6 Urban population growth in the United States from 1960 to 2020 as a percentage of total population. Data source: World Bank Data (https://data.worldbank.org/indicator/SP.URB.TOTL.IN.ZS?locations=US).

3.1.2 Climate change in the contiguous United States

During the 20th century the United States became wetter and warmer, with varying patterns and a few exceptions depending on the region (CCSP, 2008; EPA, 2016; Brown et al., 2019b). As shown in Figure 3.7, the eastern and southern US have encountered an increase in precipitation, whereas the southwest faced a rainfall drop (CCSP, 2008; EPA, 2016; Easterling et al., 2017). More specifically, over the last decades the average annual precipitation increased in the Midwest, Great Plains, and the Northeast, and decreased in parts of the Southeast and Southwest (Balling & Goodrich, 2011; Georgakakos et al., 2014; Sun & Lall, 2015; Hoerling et al., 2016; Bartels et al., 2020). Starting from 2001 the arid areas of the Southwest (i.e., California, Nevada, Utah, Arizona, and New Mexico) experienced invasive droughts that were produced by the combination of reduced precipitation (whose effects were amplified by high temperatures), increased ET, and decreased runoff (MacDonald, 2010). An example of these events is the drought that occurred in California from 2012 to 2016, which is recalled to be one of the most severe, longest, and warmest in the history of this area (Lund et al., 2018). Furthermore, an increase in the intensity and frequency of heavy precipitation has been observed throughout most of the country as well, especially in the northeastern US (Easterling et al., 2017).

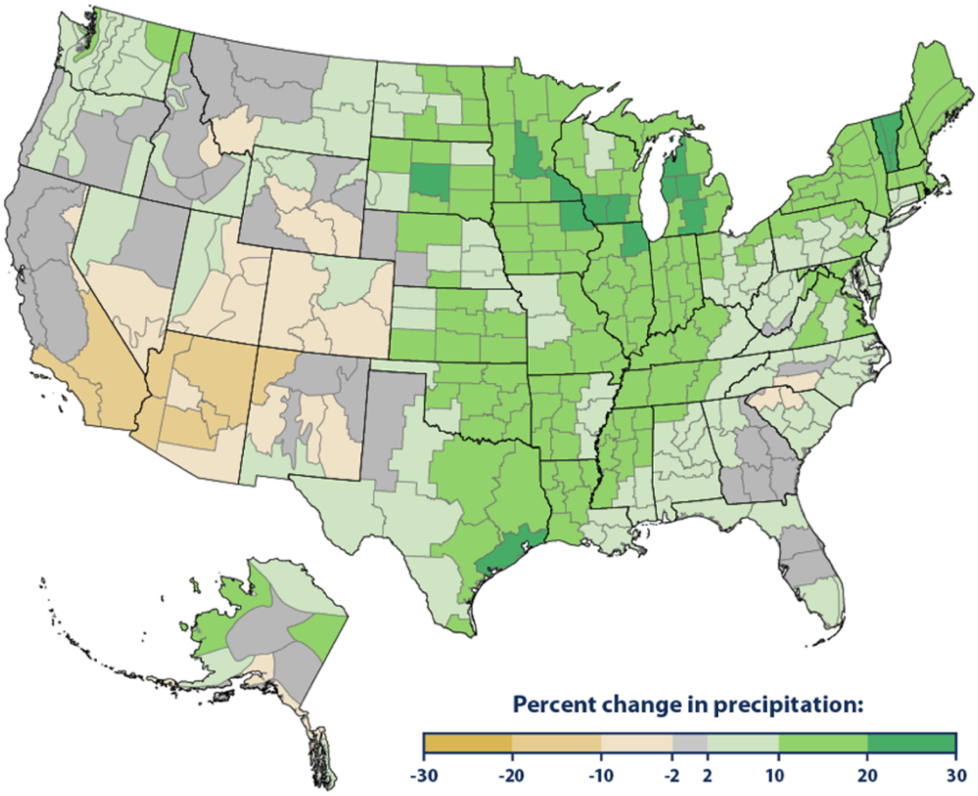

Figure 3.7 Percentage variation of total annual precipitation in 2020 with respect to the values observed in 1901 for the CONUS and 1925 for Alaska. Figure adapted from https://www.epa.gov/climate-indicators/climate-change-indicators-us-and-global-precipitation.

The average air temperature has increased in the whole CONUS since 1901 (Figure 3.8), with some areas of the United States becoming significantly warmer, such as the North, the West, and Alaska, while in some other regions, like the Southeast, there has been a smaller variation (CCSP, 2008; EPA, 2016; Vose et al., 2017). However, not all of these regional trends are statistically significant (EPA, 2016). Warming temperatures have shifted the timing of the peak in rivers flow, as demonstrated by earlier peaks in the western US. This effect is the product of the reduction of spring-snow pack, earlier snowmelt, and a higher fraction of precipitation in the form of rain, instead of snow (Georgakakos et al., 2014). Heat waves have become more intense in the US, except for the region of the Great Plains and the Midwest, while the occurrence of cold waves has decreased (Vose et al., 2017).

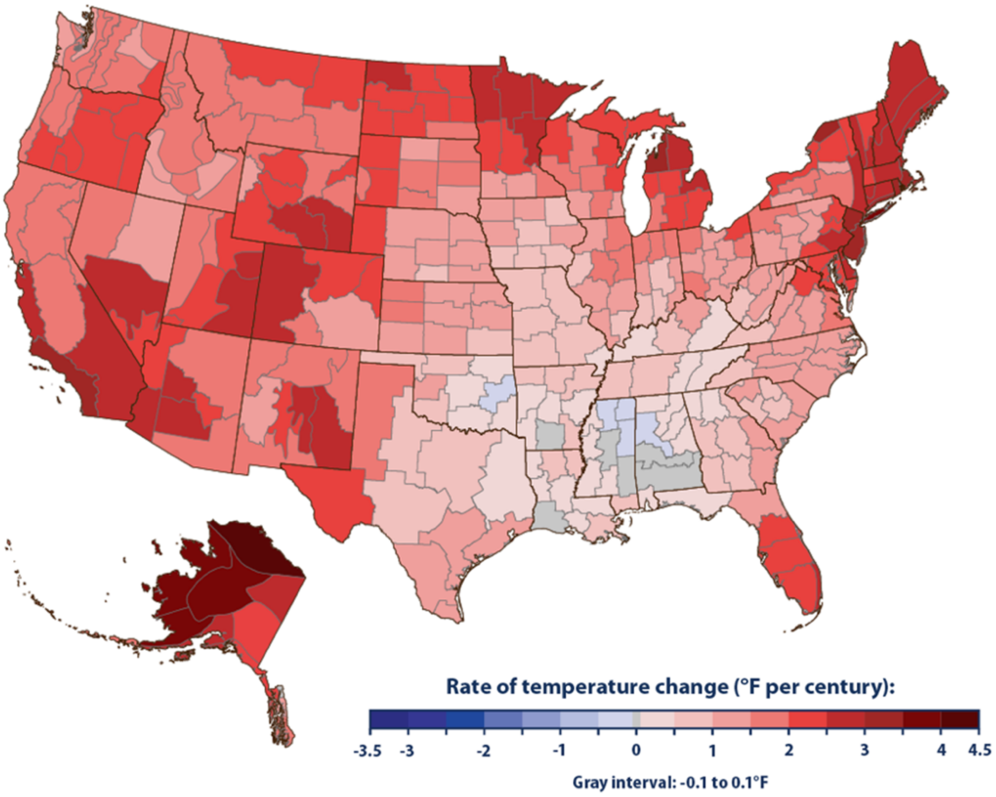
Rate of temperature change (°F per century):
-3.5
-3
-2
-1
0
1
2
3
4
4.5
Gray interval: -0.1 to 0.1°F

Figure 3.8 Rate of change in annual average air temperature with respect to the values observed in 1901 for the CONUS and 1925 for Alaska. Figure adapted from https://www.epa.gov/climate-indicators/climate-change-indicators-us-and-global-temperature.

Concerning runoff, an increase was observed in the Mississippi River Basin and Northeastern CONUS, while a decrease was typical of the Colorado River Basin. Moreover, regions with a higher availability of water ran into a decrease in ET more than regions with a limited amount of water. Overall, the western US is considered to be one of the regions in the world that is affected the most by climate change (Dettinger et al., 2015).

Future climatic scenarios suggest that the spatially variable trends observed so far are likely to persist (CCSP, 2008; Easterling et al., 2017). Moreover, also in the coming decades the change of climatic variables is predicted to vary across the country. Even though in large areas of the CONUS (particularly in the Northern region, but also the Eastern region) precipitation is projected to increase, some other areas (i.e., West and Southwest) will become drier as they will receive less rainfall (Easterling et al., 2017). On the other hand, the rise in temperature, affecting the whole CONUS, will determine an increase of evaporative demand, which in some areas of the country (e.g., in regions of the Colorado River Basin) will nullify the positive effect due to increasing precipitation, leading to an overall reduction of streamflow (Vose et al., 2017). Finally, in the coming decades some regions of the US will continue to experience extreme hydrologic events, such as prolonged and unprecedented heat waves and periods of drought, as well as heavy rainfall (CCSP, 2008; Vose et al., 2017; Brown et al., 2019a).

3.2 Input datasets

The study presented in this Thesis was conducted with the use of maps extracted from datasets derived from satellite imagery and in-situ observations. The following subsections describe the products that were selected for the extraction and processing of data used in RO1 and RO2.

3.2.1 Global Surface Water dataset

The Global Surface Water dataset detects the location and seasonality of water bodies of rivers, lakes, and wetlands at the global scale (Pekel et al., 2016). It was obtained from the collection of over three million Landsat satellite images observed during 37 years (i.e., from 1984 to 2020) at a 30 m spatial resolution. Therefore, it provides an unprecedented global-scale and high-resolution evaluation of surface water dynamics caused by both natural processes, such as flooding, sedimentation, and channel migration, and human influence, such as dam construction and water abstraction (Yamazaki & Trigg, 2016). This consistent global analysis of the Earth's water system includes multiple layers mapping different features of the spatial and temporal distribution of surface waters and obtained through the application of techniques of big data exploration and information extraction. Moreover, temporal profiles showing the historical evolution of surface water at a specific location (water history) are supplied as well as metadata storing information about the number of total observations and valid observations that can be used to estimate the level of reliability of each product.

The work conducted by Pekel et al. (2016) first computed the frequency with which water appeared to be present in each 30 by 30 m pixel of the images from the Landsat archive and they represented such information in the Surface Water Occurrence (SWO) product. The Occurrence Change Intensity layer depicts the location where SWO increased, decreased, or remained constant between two time windows, 1984-1999 and 2000-2020. The percentage values associated to each pixel of this product reveal both the direction and the intensity of the change in occurrence, and thus they represent any gain, loss, and constancy in persistence that occurred during the observational period. In particular, the intensity of change in SWO was calculated for pairs of the same months containing valid observations in both epochs (homologous pairs of months). Afterwards, the difference between the SWO of the two epochs was evaluated for each pair and finally the map of Occurrence Change Intensity was generated from the average of these differences among all months (locations without pairs of homologous months were not mapped). This layer was employed for the quantification of the change in surface water extent in the analysis of RO1 (see Section 4.1 of Chapter 4). The Recurrence product documents the frequency with which water reappeared from year to year over the time series, while the Seasonality layer illustrates the intra-annual behavior of surface water observed during a single year (2020) to discriminate permanent from seasonal water and quantify the duration of water persistency. The Transitions layer describes the change in seasonality between the last and first year of the time series and classifies pixels in three main classes: permanent water, seasonal water, and no water. The temporal profile associated to each pixel and the maps of SWO and recurrence allowed the definition of classes of water transitions. The last year of observation is always 2020, as in this year there is a high number of valid observations that allow to assess the presence or absence of water. The first year of observation, instead, is the first year of the time series during which a sufficient number of valid observations is found. Overall, eight classes of transition were defined: unchanging permanent water surfaces, new permanent water surfaces (conversion of land into permanent water), lost permanent water surfaces (conversion of permanent water into land), unchanging seasonal water surfaces, new seasonal water surfaces (conversion of land into seasonal water), lost seasonal water surfaces (conversion of a seasonal water into land), conversion of permanent water into seasonal water, and the conversion of seasonal water into permanent water. The Transitions layer was used to identify locations that experienced a loss of surface water in the analysis of RO2, while the SWO map was employed to support the analysis of the stability of the pixels classified with the transition classes selected to define the Surface Water Loss map (see Section 5.1 of Chapter 5 for more details). Finally, the Maximum Water Extent product outlines all the pixels where water was ever detected over the observational period. Also this layer aided the analysis of RO2.

3.2.2 Global Human Settlement dataset

The Global Human Settlement Layer (GHSL) project comprises various maps providing a multitemporal description of the human presence observed in the past at global scale and different spatial resolution (Corbane et al., 2019). This dataset was developed for the detection of the temporal evolution of the extent and spatial distribution of built-up areas and to derive information about population distribution using EO data between 1975 and 2014 from the Landsat collections (Melchiorri et al., 2019).

A machine learning technique was adopted to process Landsat data and classify each pixel of the images to extract maps of built-up areas observed in 1975, 1990, 2000, and 2014 with a 30 m spatial resolution. These four maps were then assembled into a single product that shows the multitemporal evolution of the extent of human settlements, the so-called GHS-BUILT layer. Four classes of built-up areas are depicted in GHS-BUILT layer: built-up developed from 2000 to 2014, built-up developed from 1990 to 2000, built-up developed from 1975 to 1990, and built-up developed before 1975. The combination of GHS-BUILT layer and census data allowed the definition of another product, the GHS-POP layer, which describes the presence and distribution of resident population (as number of inhabitants per cell) in four years (1975, 1990, 2000, and 2015) at a 250 m spatial resolution. The GHS-BUILT layer was used in the analysis of both ROs to determine the total extent of urban areas in different epochs, while the GHS-POP layer was employed in RO1 for the quantification of total population in the first and second epochs considered in the analysis (see Section 4.1 of Chapter 4 and Section 5.1 of Chapter 5 for more details). Finally, the GHSL project includes also maps showing the degree of urbanization in the four epochs, the GHS-SMOD package. The layers of this package combine the information contained in the GHS-BUILT and GHS-POP maps to distinguish different typologies of settlement at 1 km spatial resolution. In particular, three classes of settlement typology were identified, i.e., urban centre, urban cluster, and rural area, given by a specific combination of data of population size and densities of population and built-up area.

3.2.3 Irrigated Agriculture Dataset for the United States

The Irrigated Agriculture Dataset for the United States (MIrAD-US) provides irrigation data for four epochs (2002, 2007, 2012, and 2017) across the contiguous United States (CONUS) at a 250 m spatial resolution (Pervez & Brown, 2010), as shown in Figure 3.5 of Subsection 3.1.1 of this Chapter. This is a MODIS product as it is derived from images of the Moderate Resolution Imaging Spectroradiometer (MODIS) sensor, and it was employed to evaluate the extent of irrigated land in the two epochs considered in RO1 of this Thesis (see Section 4.1 of Chapter 4).

The irrigated agriculture extent depicted in the MIrAD-US was determined with a robust geospatial modeling approach that integrates three input data: statistics of irrigation at the county level for 2002 provided by the Census of Agriculture, the annual peak of the MODIS Normalized Difference Vegetation Index (NDVI) which gives an estimate of the maximum vegetation growth, and the land cover mask for agricultural lands derived from National Land Cover Dataset 2001 (NLCD). The NDVI is a widely used vegetation index that quantifies the photosynthetically active radiation (PAR) absorbed by plants, thus representing an indicator of biomes greenness and of vegetation health (Zhou et al., 2009; Huang et al., 2021). As such, this index is a key parameter of the geospatial modeling approach used for the assessment of the MIrAD-US product. Indeed, in order to guarantee the reliability of the modeling approach, it was hypothesized that within the same county the peak value of the NDVI is higher in irrigated than in non-irrigated crops. Moreover, the application of the model also relied on the assumption that the NDVI associated to the peak of the growing season varies for each crop and across the area of the US, and on the hypothesis that under drought conditions due to non-optimal precipitation the difference between the NDVI of an irrigated and non-irrigated crops increases. A possible caveat of the applied geostatistical modeling comes from the assumption that the NDVI would show significantly different values between irrigated and non-irrigated crops. This holds in the western and semiarid regions of the US, characterized by a dry climate, while the NDVI difference is less pronounced in humid regions, which receive more precipitation. As a result, the MIrAD-US product produced an accurate categorization of most of the irrigated lands concentrated in the West, but irrigated land in the humid eastern region may not be as accurately well detected. However, the overall mapping of irrigated land across humid areas is still superior to the existing products of irrigated agriculture in the CONUS (Pervez & Brown, 2010).

3.2.4 Daymet dataset

The Daymet data product supplies long-term, continuous, gridded estimates of daily weather and climatology variables that are derived from an ensemble of statistical modeling algorithms and computer software developed to interpolate and extrapolate daily ground-based meteorological observations over continental North America, Hawaii, and Puerto Rico. Data time series cover the period from 1980 to the most recent full calendar year (for Puerto Rico data are available from 1950). The surface weather parameters included in this dataset are daily minimum and maximum temperature, precipitation, vapor pressure, shortwave radiation, snow water equivalent, and daylength, and they are all sampled at a 1 km spatial resolution (Thornton et al., 2020a). Originally, Daymet data were generated to provide measurements of near-surface meteorological conditions in remote areas lacking of instrumentation, but now their scope of applicability has greatly expanded.

To deal with the large spatial extent and high data volume, the algorithm divides the study area in square tiles with side length of 2 degree, which are then processed individually. Interpolation and extrapolation techniques of input data collected at multiple instrumented sites involve the use of weights that encode the relationships between the location where weather variables need to be estimated and the sites of observation. The primary outputs of the Daymet algorithm are temperature and precipitation values which are obtained with two separate workflows. The secondary variables of daily total shortwave radiation, daily average water vapor pressure, and accumulated snowpack are empirically derived from the primary variables, while the duration of the daylight period (daylength) is computed as a function of location and time of the year.

The most recent version of Daymet data products is Version 4, in which several improvements regarding algorithm methods, sensor timing, and bias were introduced with respect to previous versions. Specifically, among the main improvements achieved in Version 4 there is the reduction in the timing bias of input reporting weather station measurements, refinements to the three-dimensional regression model techniques in the core algorithm, and a novel approach to handling high elevation temperature measurement biases. Data of total annual precipitation and maximum and minimum monthly temperature were acquired from Daymet Version 4 to extract maps of variations in climatic drivers for RO1 of this Thesis (see Section 4.1 of Chapter 4). This is the only dataset processed in this Thesis that is not derived from remote sensing data.

4 Research Objective 1: Anthropogenic and climatic drivers of surface water extent change

Water is an essential element for both human society and ecosystems, as it serves as a fundamental source on which several anthropogenic activities are dependent, while also representing the habitat of many aquatic ecosystems (Aznar-Sánchez et al., 2019). However, many regions of the World are already facing water scarcity, since the availability of water resources in these areas has become insufficient to meet the actual demand for water (Liu et al., 2017). This is mainly the result of the global increase of human pressure on surface water, especially on streams and river systems (Wada et al., 2013; Flávio et al., 2017; Ceola et al., 2019). Among the numerous anthropogenic activities causing large impacts on surface water resources, the most incisive are growing population and urbanization, as well as economic development, irrigation, and water-management policies (Flörke et al., 2013; Starr & Levison, 2014; Wada et al., 2016). In addition, the resulting degradation of riverine ecosystems and water shortages are further aggravated by climate change. Surface waters are extremely sensitive to any alteration of the climatic conditions, especially to changes in precipitation patterns and temperature and the occurrence of droughts and floods (Kundzewicz, 2008; Balling & Goodrich, 2011; Brunner et al., 2021). On the whole, these variations are expected to reduce renewable surface water resources, particularly in dry regions, increasing the competition for water in many different sectors (e.g., agriculture, industry, ecosystems) and the impacts on regional water, energy, and food security (IPCC, 2014). Therefore, both human activities and climate change can seriously stress surface water resources, endangering the ecological integrity of many freshwater ecosystems and emphasizing the risk of water scarcity (Kummu et al., 2016). Consequently, it is important to understand which anthropogenic and climatic factors are producing changes of surface water availability. This is the reason why RO1 evaluates the influence of the variations of three anthropogenic (urban area, population, and irrigated land) and two climatic (precipitation and temperature) drivers on surface water extent change to assess which factors are responsible for the surface water gains and losses that occurred between the time-windows 1984-1999 and 2000-2020 across the CONUS. The aim of this study is to answer to the following questions, already introduced in Chapter 1: (Q1a) how has the spatial extent of surface water changed in the last 40 years? (Q1b) What are the main anthropogenic and climatic factors governing the remotely-sensed change of surface water extent and where do they determine a gain/loss of surface water?

4.1 Surface water, human dynamics, and climatic data

The evaluation of the influence of changes in anthropogenic and climatic drivers on the variation of surface water that occurred between two epochs (the first one from 1984 to 1999 and the second one from 2000 to 2020) requires information regarding the extent of surface water, urban areas, and irrigated land, the distribution of population, total annual precipitation, and monthly temperature. These data were extracted for each epoch over the entire area of the CONUS and related maps were created.

The variation of surface water extent that occurred between the two epochs was defined using the Surface Water Occurrence Change Intensity layer from the Global Surface Water dataset (Pekel et al., 2016). As stated in the Subsection 3.2.1 of Chapter 3, this product shows where surface water occurrence increased, decreased or remained invariant between 1984-1999 and 2000-2020, describing both the direction of change (i.e., increase, decrease or no change in water occurrence) and its intensity in terms of percentage at a 30 m spatial resolution. For instance, -100% indicates a complete loss of occurrence (i.e., surface water, observed in a given pixel during the first epoch, is no longer observed in the second epoch), conversely 100% indicates a complete gain of occurrence (i.e., surface water in a given pixel is observed during the second epoch only), while 0 indicates no change of occurrence. In order to identify locations that experienced a significant net change of surface water extent between the first and second epoch, given by the difference between the total number of pixels of surface water gain and the total number of pixels of surface water loss within each river basin of the CONUS, a representative threshold value was selected based on a sensitivity analysis. Given a specific threshold of change in the frequency of water observation $\mathcal{E}_{thr}$, all the pixels of the Water Occurrence Change Intensity layer having a value between -100% and -$\mathcal{E}_{thr}$ identify locations that encountered a surface water loss between the first and second epoch, while those having a value between $\mathcal{E}_{thr}$ and 100% indicate locations of surface water gain. A 75% threshold was selected as a representative value. Figure 4.1b shows an example of the associated distribution of surface water gain and loss over the region around the Great Salt Lake, Utah. The sensitivity analysis on $\mathcal{E}_{thr}$ was performed by considering additional four threshold values equal to 25%, 50%, 70%, and 80%. With the 25% and 50% thresholds, all the river basins of the CONUS are found to experience a net surface water gain, meaning that the total number of pixels of surface water gain is always greater than the total number of pixels of surface water loss within each river basin. Even though these two threshold values identify a huge number of pixels experiencing either a loss or a gain in surface water, they are not representative of a remarkable changing condition. The thresholds of 70% and 80% produced results comparable to those obtained from the 75% threshold (i.e., two and one additional river basins with a net surface water gain, respectively). Therefore, the 75% value was selected as the fiducial threshold as it supplies a reliable balance between gain and loss of surface water, while the choice of a slightly larger or smaller threshold would not substantially affect the results of the analysis.

The extent of urban area and the distribution of population were derived from the GHS-BUILT and the GHS-POP layers (see also Subsection 3.2.2 of Chapter 3), respectively, which are both part of the GHSL dataset (Corbane et al., 2019). The GHS-BUILT layer provides a multi-temporal classification of built-up presence, showing the location of urban areas developed in four epochs (before 1975, between 1975 and 1990, between 1990 and 2000, and between 2000 and 2014) and it has a spatial resolution of 30 m. For this analysis, the extent of built-up area developed until 2000 and the fraction developed between 2000 and 2014 were extracted to define the Urban Area maps describing the level of urbanization associated to the first epoch and the additional development occurred between 2000 and 2014, respectively (Figure 4.1c). Specifically, the urbanization reached in 2000 was obtained by selecting all the pixels of the GHS-BUILT layer that are representative of the built-up area observed until 1975, between 1975 and 1990, and between 1990 and 2000, while urban area expansion that took place from 2000 to 2014 was derived from the extraction of the pixels that are classified as built-up areas observed between 2000 and 2014 (Figure 4.1c). The GHS-POP layer describes the distribution of population observed in four epochs (1975, 1990, 2000, and 2015) as the number of people per cell with a spatial resolution of 250 m. For this analysis, the number of inhabitants observed until 2000 and the number of inhabitants observed until 2015 were extracted to define the Population maps describing the distribution of population in the first and second epoch, respectively. As an example, Figure 4.1d shows the distribution of population found in 2015 around the area of the city of Los Angeles.

The extent of irrigated land was obtained from the Irrigated Agriculture Dataset for the United States (MODIS MIrAD-US, see also Subsection 3.2.3 of Chapter 3), which provides irrigation data for four epochs (2002, 2007, 2012, and 2017) at 250 m spatial resolution (Pervez & Brown, 2010). The areas of irrigated agriculture observed in 2002 and 2017 were here selected to define the Irrigated Land maps of the first and second epoch, respectively (Figure 4.1e).

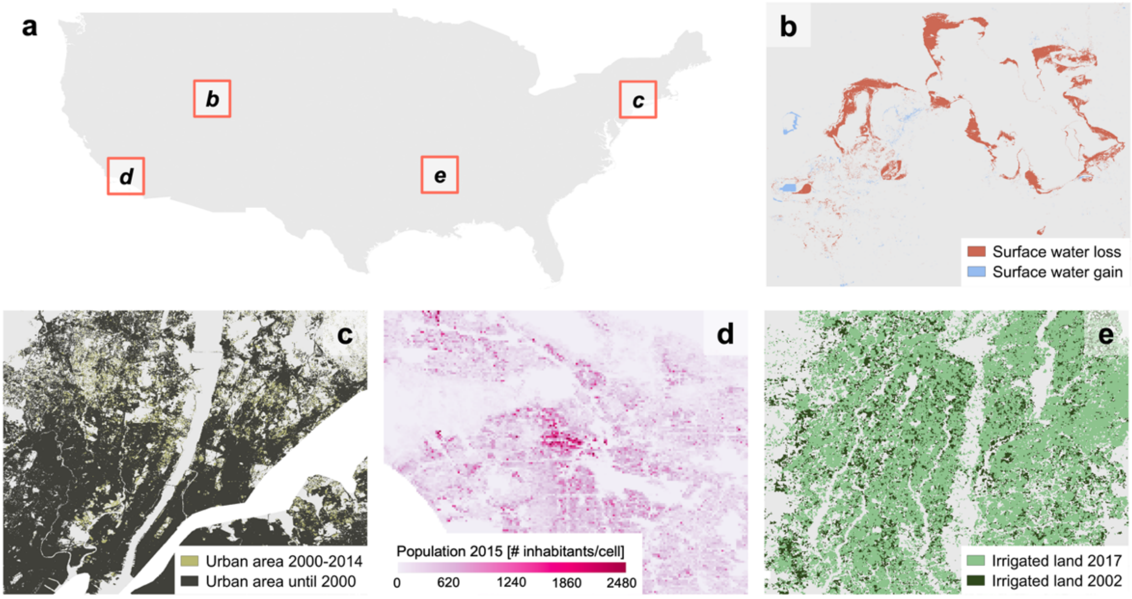

Figure 4.1 Maps of the change in surface water extent and its anthropogenic drivers over some representative regions of the CONUS. **a.** Map of the CONUS indicating the location of the zoom-in areas shown in panels b, c, d, and e. **b.** Zoom-in of the Surface Water Loss and Surfacer Water Gain maps over the region around the Great Salt Lake, Utah. **c.** Zoom-in of the maps of the fraction of urban area developed between 2000-2014 and the total urban area built until 2000 over the region around New York City, New York. **d.** Zoom-in of the Population map in 2015 over the region around the city of Los Angeles, California. **e.** Zoom-in of the maps of the irrigated land in 2017 and 2002 over the region between the city of Little Rock and the City of Memphis in Arkansas.

Finally, the total annual precipitation (in mm/yr) and the monthly maximum and minimum temperature (in °C) were both derived from the Daymet Version 4 dataset (see Subsection 3.2.4 of Chapter 3) and they both have a spatial resolution of 1 km (Thornton et al., 2020a, 2020b). In particular, the total annual precipitation was averaged over the two epochs to obtain the Mean Annual Precipitation maps of the first and second epoch. Regarding temperature, the monthly maximum and minimum temperature are calculated by Daymet as the average of the maximum and minimum daily temperatures (Thornton et al., 2020b). Starting from these values, the mean monthly temperature of each month of the two epochs was estimated as the average of the maximum and minimum temperatures of each month (Li et al., 2016), which was then averaged over the two epochs separately for each month to get the Mean Monthly Temperature maps of the first and second epoch. For more details on the calculation of both precipitation and temperature change see Section 4.2 of this Chapter.

4.2 Assessment of the change in surface water extent, anthropogenic and climatic contributors

The goal of RO1 of this Thesis is to examine the relation between changes in anthropogenic and climatic factors and the variation of surface water extent that occurred between two time windows, 1984-1999 (first epoch, ep1) and 2000-2020 (second epoch, ep2).

The extent of surface water (SW) represents the dependent variable, while the independent variables are the anthropogenic and climatic drivers, which are here considered to be the main factors responsible for changes in surface water extent. In particular, urban areas (URB), the distribution of population (POP), and irrigated land (IRR) represent the anthropogenic drivers, whereas precipitation (PCP) and temperature (TMP) represent the climatic drivers (Figure 4.2a).

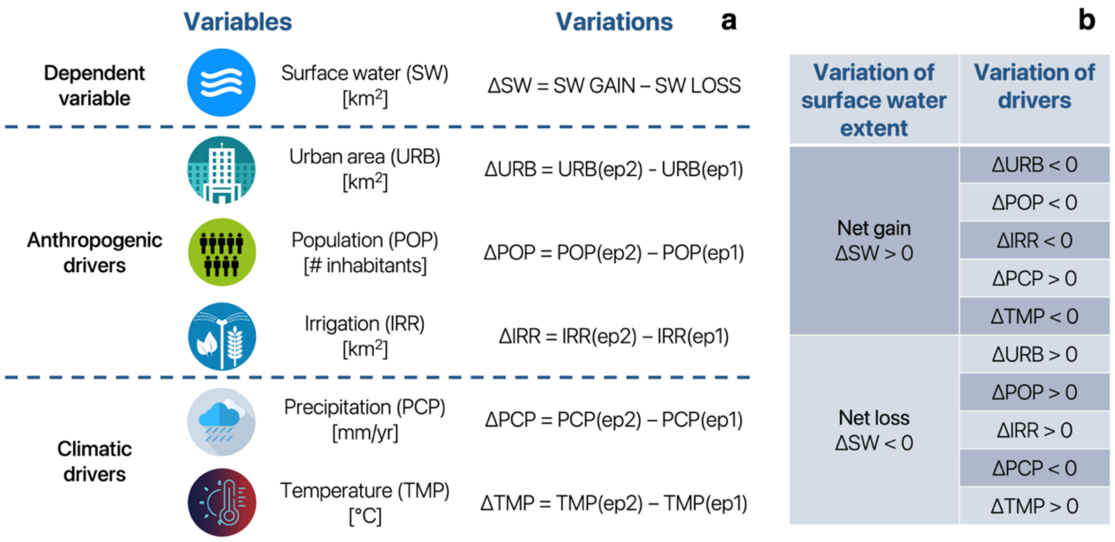
Variables
Variations
a
b
Dependent variable
Surface water (SW) [km²]
ΔSW = SW GAIN – SW LOSS
Anthropogenic drivers
Urban area (URB) [km²]
ΔURB = URB(ep2) - URB(ep1)
Population (POP) [# inhabitants]
ΔPOP = POP(ep2) – POP(ep1)
Irrigation (IRR) [km²]
ΔIRR = IRR(ep2) – IRR(ep1)
Climatic drivers
Precipitation (PCP) [mm/yr]
ΔPCP = PCP(ep2) – PCP(ep1)
Temperature (TMP) [°C]
ΔTMP = TMP(ep2) – TMP(ep1)
Variation of surface water extent
Variation of drivers
Net gain ΔSW > 0
ΔURB < 0
ΔPOP < 0
ΔIRR < 0
ΔPCP > 0
ΔTMP < 0
Net loss ΔSW < 0
ΔURB > 0
ΔPOP > 0
ΔIRR > 0
ΔPCP < 0
ΔTMP > 0

Figure 4.2 Schematic representation of the methodology adopted for the analysis of the influence of anthropogenic and climatic drivers on the variation of surface water extent. **a.** Definition of the variables involved in the analysis and the estimate of their variations between the first and second epoch. **b.** Variations in the anthropogenic and climatic drivers contributing to the net change in surface water extent (gain and loss) assumed in this analysis.

The variations of surface water extent, anthropogenic drivers, and climatic drivers that took place between the first and the second epoch were extracted from the maps defined in Section 4.1 of this Chapter. Specifically, the difference between the total gain and the total loss of surface water extent was computed to evaluate the net variation of surface water between the two epochs. A net surface water gain is detected when surface water gain is greater than surface water loss, while a net surface water loss is found when surface water gain is smaller than surface water loss. Similarly, the variations of each anthropogenic driver were estimated as the difference between the total amount of the driver found in the first and the second epoch. In particular, the difference between the Urban Area maps, Population maps, and Irrigated Land maps associated to the second and first epoch produced the respective change maps. The changes of the dependent variable and the anthropogenic drivers were then aggregated at the river basin level and within the climatic regions of the CONUS.

For the variations of the climatic drivers a slightly different approach was adopted. Indeed, the variation of precipitation was evaluated as the difference between the average total annual precipitation observed during the first and the second epoch, while the variation of temperature was estimated as the average of the mean monthly temperature anomaly found between the two epochs. As described in Section 4.1 of this Chapter, the total annual precipitation averaged over the 16 years between 1984-1999 and over the 21 years between 2000-2020 produced the Mean Annual Precipitation maps of the first and second epoch. The equation used to calculate the mean annual precipitation associated to the two epochs is the following:

$$PCP_{annual,avg}(epoch) = \left. \sum_{yr=yr,i}^{yr,f} PCP_{annual}^{yr} \middle/ n_{yr} \right. \tag{4.1}$$

where yr is from 1984 (yr,i) to 1999 (yr,f) for the first epoch, and from 2000 (yr,i) to 2020 (yr,f) for the second epoch, while n_{yr} is equal to 16 for the first epoch and 21 for the second epoch.

The Precipitation Change map (Figure 4.3a) showing the variation of precipitation is given by the difference of the mean total annual precipitation between the two epochs (i.e., between the Mean Annual Precipitation maps), as follows:

$$\Delta PCP = PCP_{annual,avg}(ep2) - PCP_{annual,avg}(ep1) \tag{4.2}$$

As already mentioned in Section 4.1 of this Chapter, the mean monthly temperature of each month of the two epochs was derived as the average of extreme temperatures, i.e., the daily maximum and minimum temperatures averaged over each month (Li et al., 2016). Afterwards, the average of the mean monthly temperatures over the 16 years of the first epoch (1984-1999) and over the 21 years of the second epoch (2000-2020) was computed to get the Mean Monthly Temperature maps of each month during the first and the second epoch, respectively, (e.g., maps of the mean monthly temperature of January of the first and second epoch, maps of the mean monthly temperature of February of the first and second epoch, and so on) using the following equation:

$$TMP^{m}_{monthly,avg}(epoch) = \sum_{yr=yr,i}^{yr,f} TMP^{yr}_{mean,\,m} \Big/ n_{yr} \qquad (m = 1, 2, \ldots, 12) \tag{4.3}$$

After that, the temperature anomaly for each month was calculated as the difference between the mean monthly temperatures of corresponding months in the first and the second epoch (e.g., temperature anomaly of January, temperature anomaly of February, and so on), and the monthly anomalies between the two epochs were averaged over the twelve months of the year to define the Temperature Change map (Figure 4.3b). This calculation was performed using the following equation:

$$\Delta TMP = \sum_{m=1}^{12} (TMP^{m}_{monthly,avg}(ep2) - TMP^{m}_{monthly,avg}(ep1))/12 \tag{4.4}$$

Contrary to the anthropogenic drivers, the variations of the climatic drivers were averaged over the area of the river basins and the climatic regions of the CONUS.

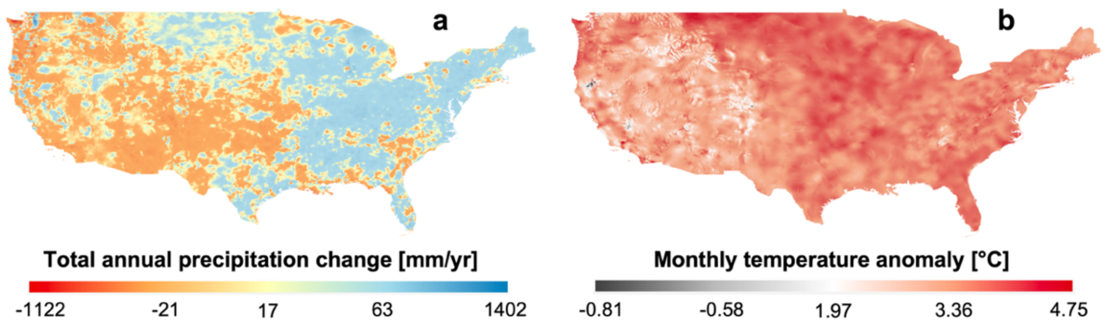
a
Total annual precipitation change [mm/yr]
-1122
-21
17
63
1402
b
Monthly temperature anomaly [°C]
-0.81
-0.58
1.97
3.36
4.75

Figure 4.3 Maps of the change in the climatic drivers over the CONUS. **a.** Precipitation Change map showing the change in the average total annual precipitation between 1984-1999 and 2000-2020. **b.** Temperature Change map showing the average monthly anomalies between 1984-1999 and 2000-2020.

In each river basin of the CONUS the direction of change of every anthropogenic and climatic driver was then compared to the direction of change of surface water extent to determine which drivers resulted to be responsible for the gain or loss of surface water. In order to contribute to a net surface water gain, it was assumed that all anthropogenic drivers must decrease, while precipitation and temperature have to increase and decrease, respectively. Whereas, in order to cause a net surface water loss, it was assumed that all anthropogenic drivers must increase, while precipitation and temperature have to decrease and increase, respectively (Figure 4.2b). The same variations of all the drivers and of surface water extent were also evaluated at the climatic region level to support the interpretation of the results.

4.3 Results

4.3.1 Change in surface water extent

The difference between the total gain and the total loss in surface water extent that took place between the first and the second epoch within the river basins of the CONUS provides an estimate of the variation of surface water resources, here also referred to as the net surface water change (Figure 4.4).

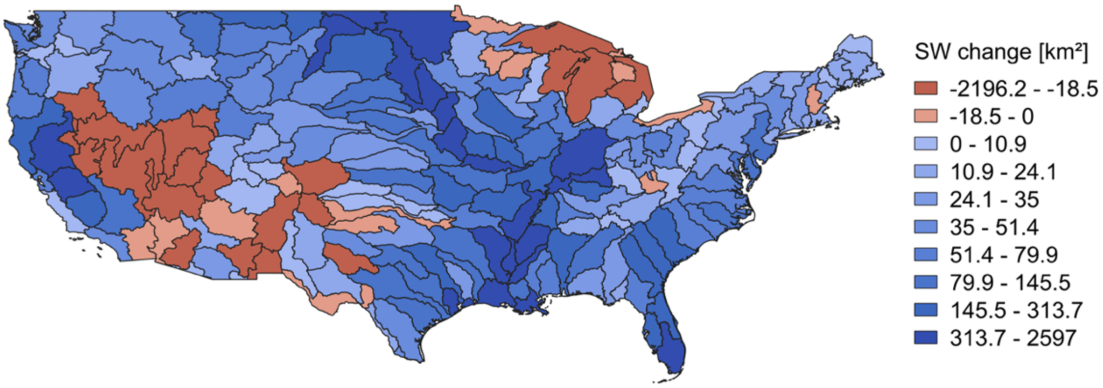

Figure 4.4 Spatial distribution of the net surface water change that occurred between the first (1984-1999) and the second (2000-2020) epoch across the river basins of the CONUS. River basins with a net surface water loss (total surface water loss greater than total surface water gain) are characterized by negative values (red shades), whereas positive values (blue shades) correspond to river basins with a net surface water gain (total surface water gain greater than total surface water loss).

The majority of the study area of the CONUS (i.e., 169 river basins, covering 78.64% of the CONUS area) experienced a net gain of surface water, meaning that the total surface water gain was greater than the total surface water loss. A net loss of surface water, indicating that the total surface water gain is smaller than the total surface water loss, is found in the remaining 35 river basins that encompass 21.36% of the study area. As expected, river basins located in the dry region of the southwestern US witnessed a reduction of their surface water resources. Another area of the country where surface water resulted to decrease corresponds to some river basins in northeastern US.

The evaluation of surface water extent change as a function of the main climatic regions of the CONUS (Figure 4.5) reveals that negative variations are mainly located in the arid zone, while the rest of the climatic regions experienced an overall increase in their surface water extent.

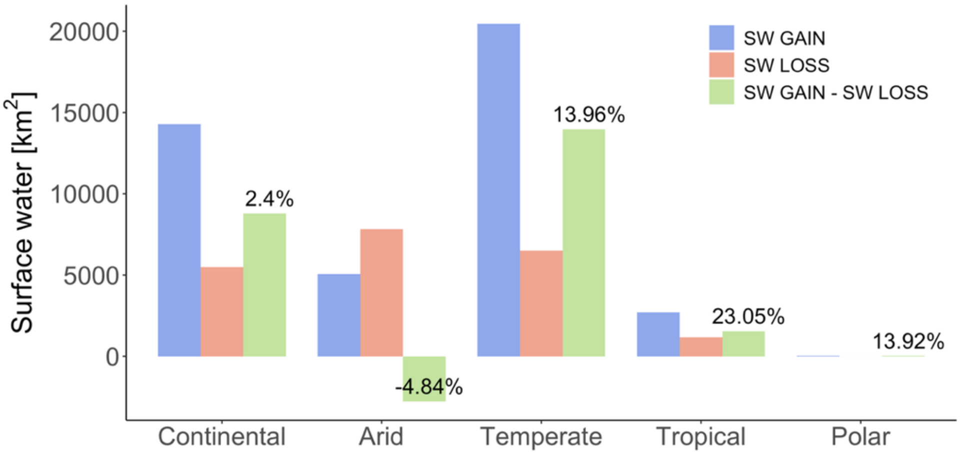

Figure 4.5 Histogram of the total amount of surface water gain (in blue), surface water loss (in red), and net surface water change (in green) across the main climatic regions of the CONUS. The net surface water change is given by the difference between the total gain and the total loss of surface water extent, so that a negative value indicates a net surface water loss, while a positive value indicates a net surface water gain. Percentage values reported above each bin of net surface water change represent the relative variation of surface water extent in the second epoch (2000-2020) with respect to the total extent observed in the first epoch (1984-1999).

A more detailed representation of the distribution of surface water gain, loss, and net variation of surface water in each subtype of the main climatic classes found in the CONUS is depicted in Figure 4.6. These histograms show that the subtypes "arid, desert, cold" and "arid, steppe, cold" of the arid climatic region are the ones having a net loss of surface water, with a reduction of surface water extent in the second epoch with respect to the that observed during the first epoch of -16.41% and -1.37%, respectively. These two subtypes of the arid climatic region are both characterized by a dry climate with a mean annual air temperature less than 18°C (cold), whereas the difference between them consists in the fact that the steppe (semi-desert) climate is slightly wetter than the desert climate, which explains why the greatest reduction in surface water extent was found in the "arid, desert, cold" climatic subtype (Beck et al., 2018).

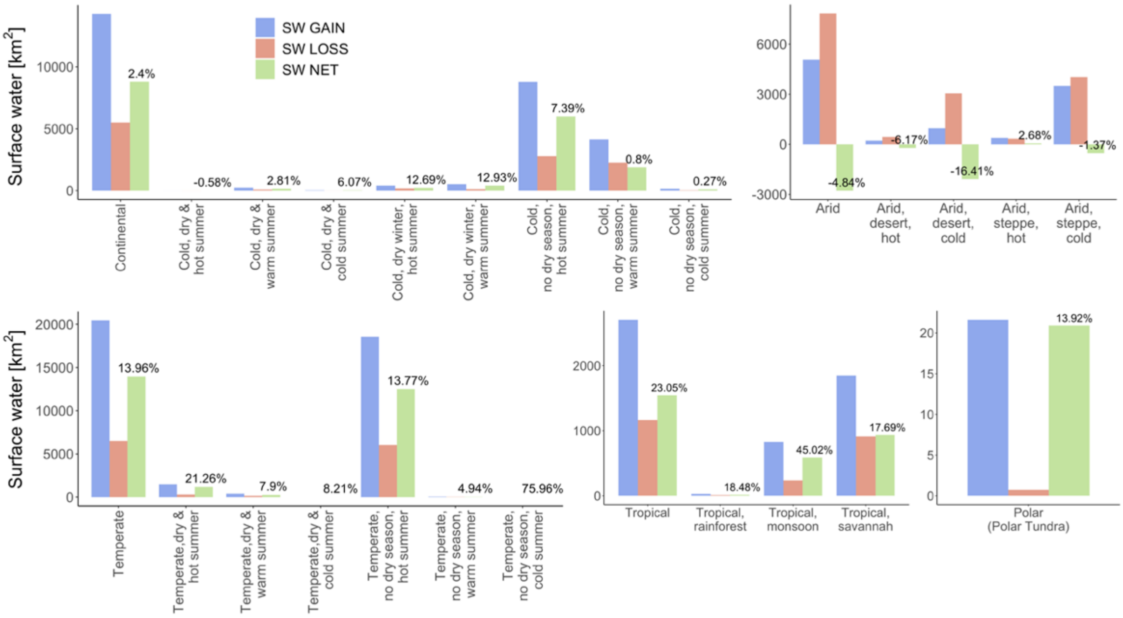

Figure 4.6 Histograms of the total amount of surface water gain (in blue), surface water loss (in red), and net surface water change (in green) across the subtypes of the main climatic regions of the CONUS. The net surface water change is given by the difference between the total gain and the total loss of surface water extent, so that a negative value indicates a net surface water loss, while a positive value indicates a net surface water gain. Percentage values reported above each bin of net surface water change represent the relative variation of surface water extent in the second epoch (2000-2020) with respect to the total extent observed in the first epoch (1984-1999).

4.3.2 Change in the anthropogenic and climatic drivers

The temporal variation of the anthropogenic drivers was obtained as the difference in time (i.e., second epoch minus first epoch) of total population and total extent of urban areas and irrigated land within each river basin of the CONUS. Figure 4.7 shows the spatial distribution of the values of change in urban area, population, and irrigated land across the river basins of the CONUS. Urban area expanded in all the river basins, as its extent increased from the first to the second epoch (Figure 4.7a). For this reason, urban area was not considered in the identification of the anthropogenic factors responsible for the variations in the extent of surface water. Therefore, from now on this analysis will include only two anthropogenic drivers (i.e., population and irrigated land). As previously mentioned, the most urbanized areas are found in the eastern US and along the West Coast. The total population increased in most of the river basins (167 river basins, covering 81.55% of the CONUS area), and those with a decrease in population (37 river basins) are mainly located in the northeastern and the central area of the country (Figure 4.7b). Finally, the extent of irrigated land increased in 136 river basins (67.47% of the CONUS area), while in the remaining 68 river basins irrigated agriculture decreased, especially in the western region of the CONUS (Figure 4.7c).

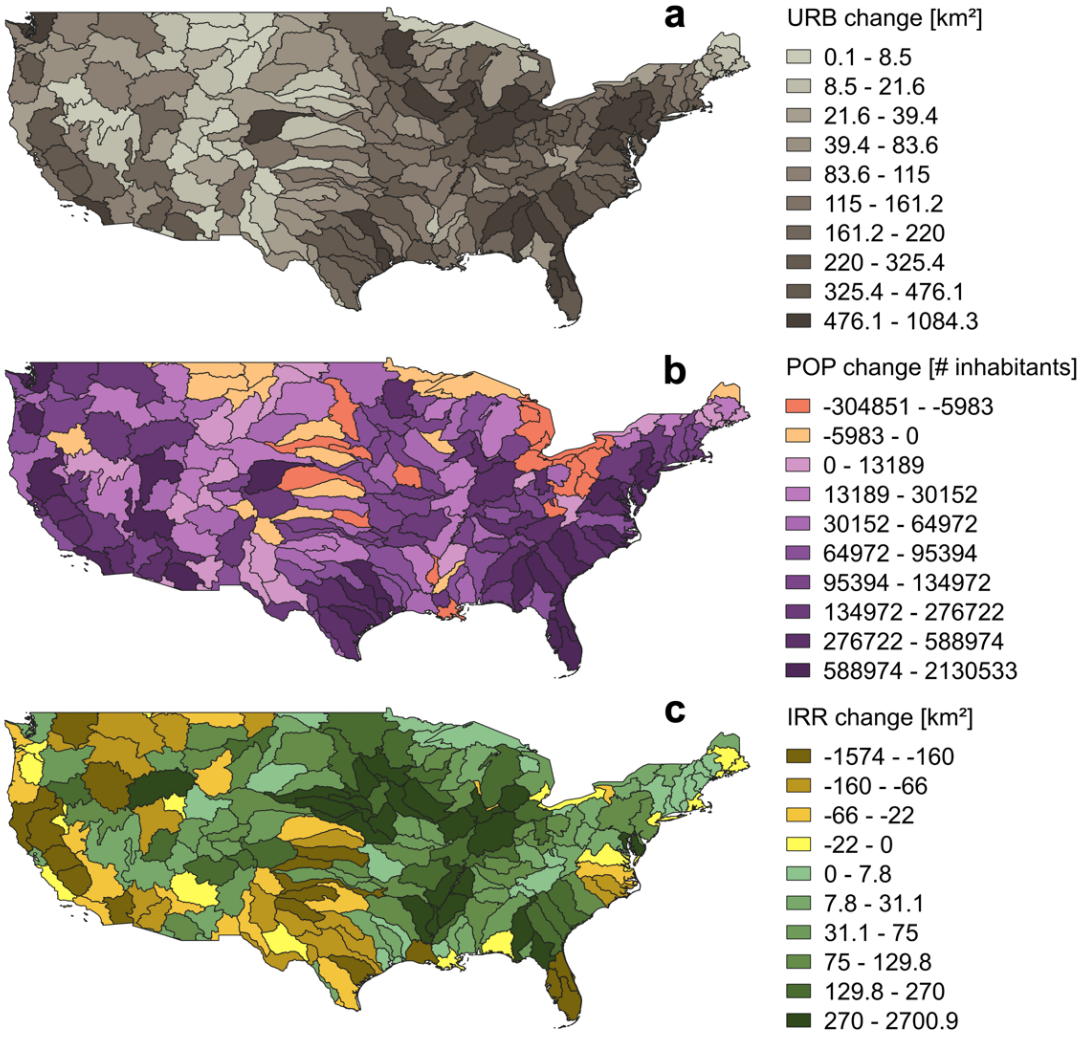
a
URB change [km²]
0.1 - 8.5
8.5 - 21.6
21.6 - 39.4
39.4 - 83.6
83.6 - 115
115 - 161.2
161.2 - 220
220 - 325.4
325.4 - 476.1
476.1 - 1084.3
b
POP change [# inhabitants]
-304851 - -5983
-5983 - 0
0 - 13189
13189 - 30152
30152 - 64972
64972 - 95394
95394 - 134972
134972 - 276722
276722 - 588974
588974 - 2130533
c
IRR change [km²]
-1574 - -160
-160 - -66
-66 - -22
-22 - 0
0 - 7.8
7.8 - 31.1
31.1 - 75
75 - 129.8
129.8 - 270
270 - 2700.9

Figure 4.7 Spatial distribution of the variations of the anthropogenic drivers that occurred between the two epochs considered in this study across the river basins of the CONUS. **a.** Change in urban area extent, defined as the difference in total built-up area extent within each river basin between the second and the first epoch. This variation is always positive since urban areas experienced only an expansion. **b.** Change in population, defined as the difference in total population within each river basin between the second and the first epoch. **c.** Change in irrigated land extent, defined as the difference in total irrigated land extent within each river basin between the second and the first epoch.

The variation of the climatic drivers was evaluated as the difference between the average values of the mean annual precipitation and the mean monthly temperature observed in the second and the first epoch averaged over the area of each river basin of the CONUS. Figure 4.8 shows the spatial distribution of the values of changes in precipitation and temperature across the river basins of the CONUS. The mean annual precipitation increased in 132 river basins (54.64% of the CONUS area), which for the large part are located in Eastern US, while the remaining 72 river basins with a negative variation of precipitation are found in Western US (Figure 4.8a). The mean monthly temperature anomaly has positive variations in most of the river basins of the CONUS (199 river basins, covering 96.68% of the CONUS area), with the exception of 5 river basins which experienced a small decrease in temperature, ranging from 0 to -0.32°C (Figure 4.8b). For this reason, temperature was not considered in the identification of the climatic factors responsible for the variations in the extent of surface water. Therefore, from now on this analysis will include only one climatic driver (i.e., precipitation).

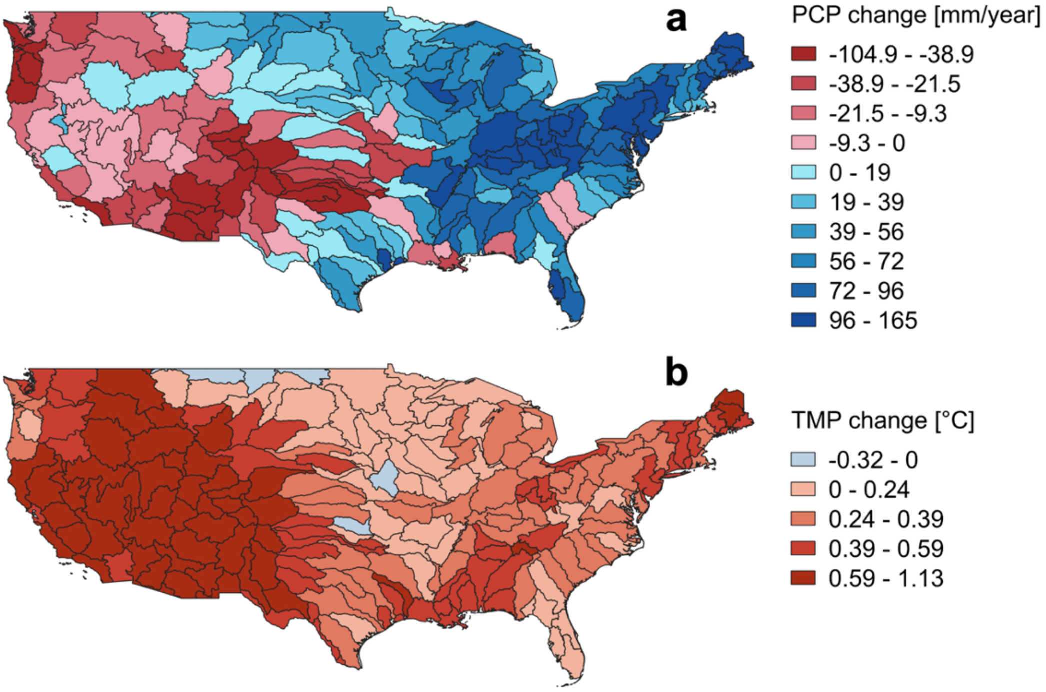

Figure 4.8 Spatial distribution of the variations of the climatic drivers that occurred between the two epochs considered in this study across the river basins of the CONUS. **a.** Change in precipitation, defined as the difference in mean annual precipitation averaged over each river basin between the second and the first epoch. **b.** Change in temperature, defined as the difference in mean monthly temperature anomaly averaged over each river basin between the second and the first epoch. Only five river basins experienced a decrease of the mean monthly temperature anomaly.

The variation of the anthropogenic and climatic drivers was also estimated across the main climatic regions of the CONUS (Figure 4.9). On the whole, population increased in all the climatic regions of the study area, while the extent of irrigated land experienced a general decrease within the continental and arid regions. Finally, on average mean annual precipitation decreased over the arid and polar regions and increased in the rest of the climatic zones.

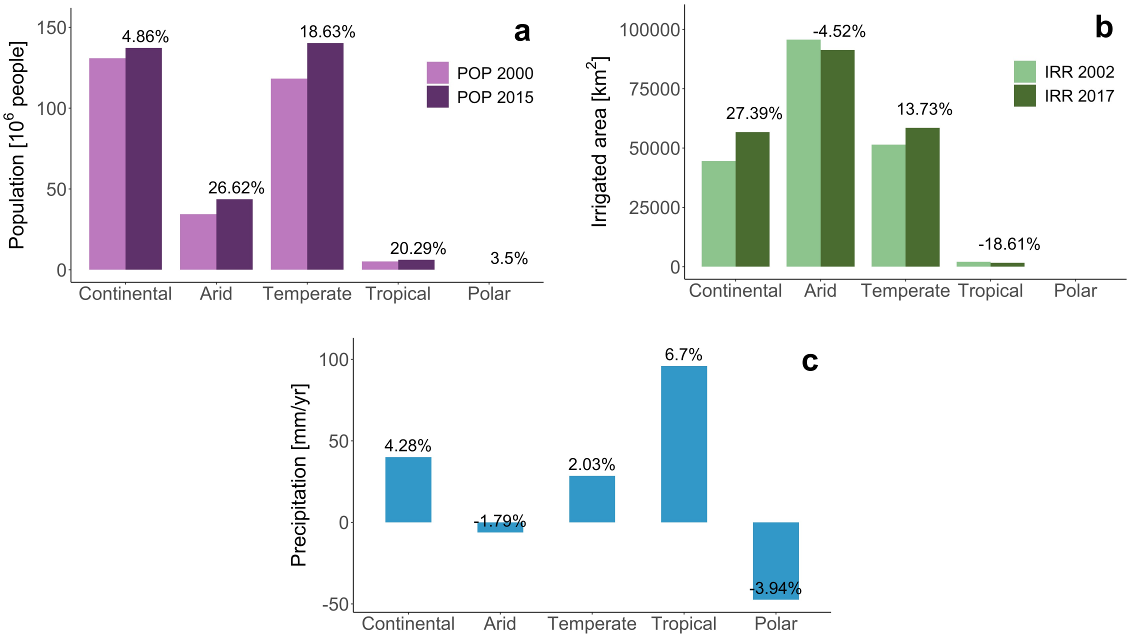

Figure 4.9 Histograms of the variation of the anthropogenic and climatic drivers across the main climatic regions of the CONUS. Percentages values reported above each bin of the population in 2015, irrigation in 2017, and precipitation change represent the relative variation of the driver in the second epoch (2000-2020) with respect to the first epoch (1984-1999). **a.** Total population in the first (POP 2000) and second epoch (POP 2015) found within each climatic region. **b.** Total extent of irrigated land in the first (IRR 2002) and second epoch (IRR 2017) found within each climatic region. **c.** Variation of the mean annual precipitation between the first (1984-1999) and second (2000-2020) epoch averaged over the area of each climatic region.

Similarly to surface water extent change, also the variation of the anthropogenic and climatic drivers was evaluated across the subtypes of the main climatic regions of the CONUS (Figure 4.10, Figure 4.11, and Figure 4.12).

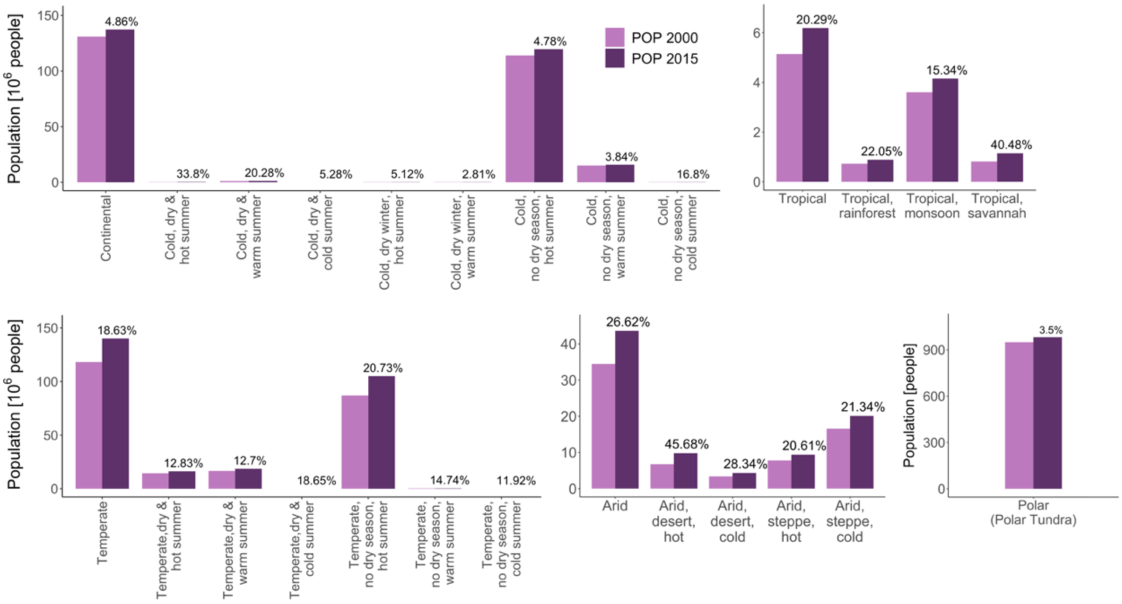

Figure 4.10 Histograms of the variation of the total population across the subtypes of the main climatic regions of the CONUS. Total population in the first epoch (POP 2000) is colored in light purple, while total population in the second epoch (POP 2015) is in dark purple. Percentages values reported above each bin of the population in 2015 represent the relative variation of total population in the second epoch with respect to the first epoch.

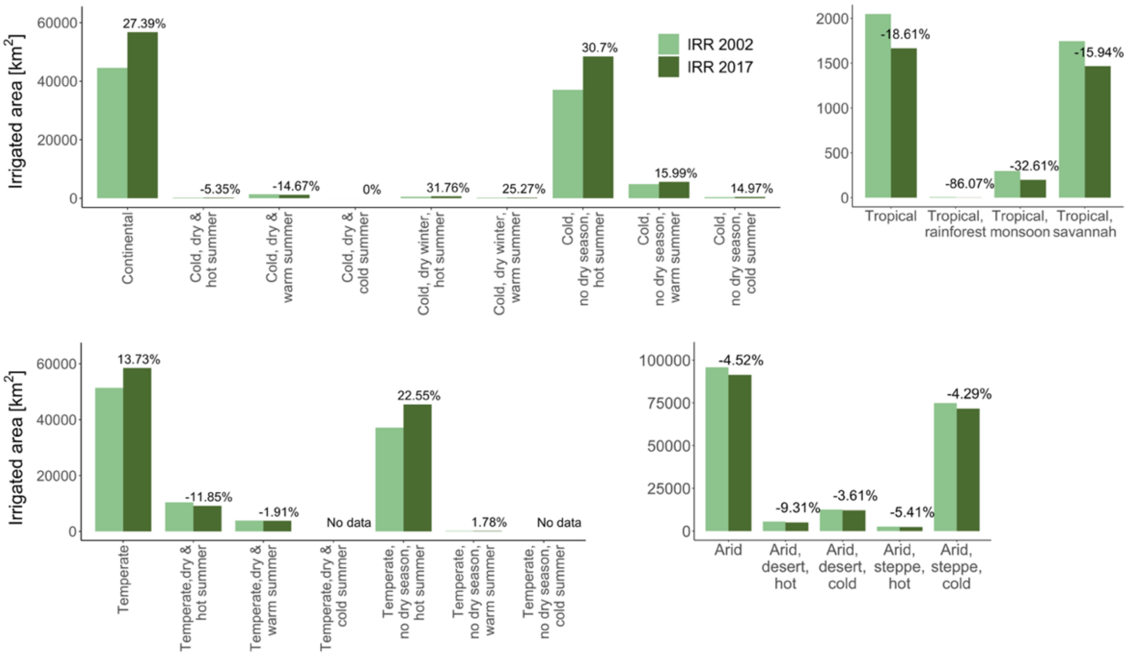

Figure 4.11 Histograms of the variation of the total irrigated land across the subtypes of the main climatic regions of the CONUS. Total irrigated land in the first epoch (IRR 2002) is colored in light green, while total irrigated land in the second epoch (IRR 2017) is in dark green. Percentages values reported above each bin of the irrigated land in 2017 represent the relative variation of total irrigated land in the second epoch with respect to the first epoch.

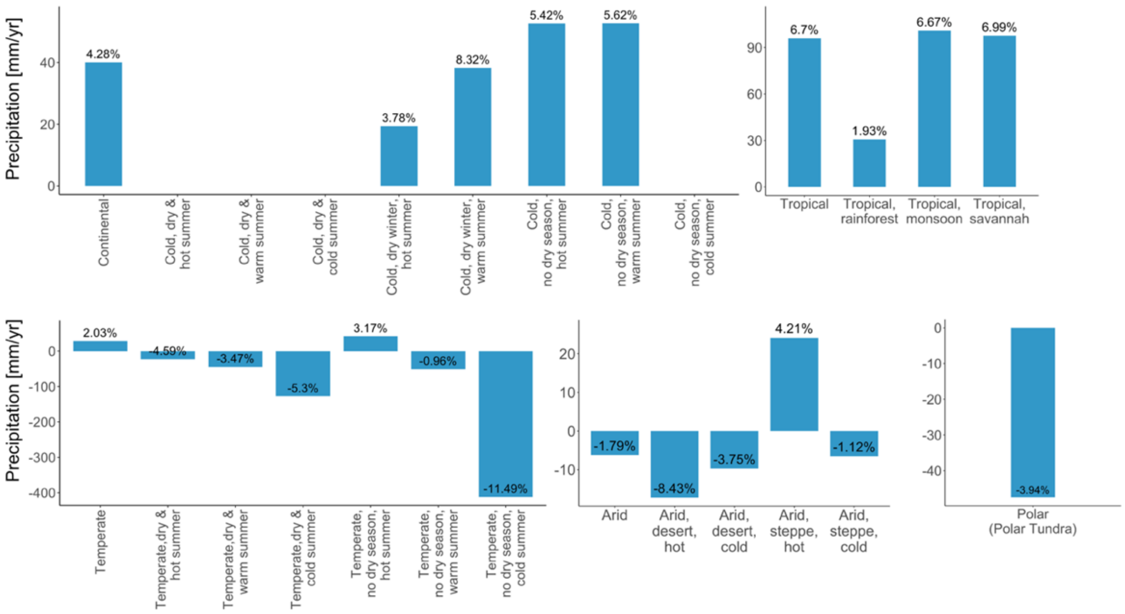

Figure 4.12 Histograms of the variation of the mean annual precipitation across the subtypes of the main climatic regions of the CONUS. Percentages values reported above each bin represent the relative variation of mean annual precipitation in the second epoch (2000-2020) with respect to the first epoch (1984-1999).

Population increased in all the subtypes of each climatic region, with the highest rates of growth found within the "temperate, no dry season, hot summer", the "arid, steppe, cold", and the "tropical, monsoon" subtype (Figure 4.10). The extent of irrigated land decreased in all the subtypes of the tropical and arid climates, with the greatest reduction in the "tropical, savannah" and the "arid, steppe, cold" subtypes, whereas in the continental and temperate regions there has been a general increase and the highest expansions of irrigated agriculture has been observed within the "cold, no dry season, hot summer" and the "temperate, no dry season, hot summer" subtypes (Figure 4.11). Precipitation increased in all the subtypes of the continental and tropical regions, with the "cold, no dry season, hot summer", the "cold, no dry season, warm summer", the "tropical, monsoon", and the "tropical, savannah" subtypes having the largest positive variation. In the subtypes of the temperate, arid, and polar regions an overall reduction of mean annual precipitation has been observed, especially in the "temperate, no dry season, cold summer" and the "arid, desert, hot" subtypes (Figure 4.12).

From the combination of the variation (increase or decrease) of the two anthropogenic (population and irrigated land) and the climatic driver (precipitation) here considered, the river basins of the CONUS were organized in eight groups, as summarized in Table 4.1.

Table 4.1 Number of river basins of the CONUS satisfying a specific combination of direction of change (increase or decrease) in the anthropogenic (population, POP, and irrigated land, IRR) and climatic (precipitation, PCP) drivers. A tick mark indicates that the condition expressed in the first row of the table is satisfied, while a cross mark indicates that the same condition is not satisfied (i.e., the opposite direction of variation in the driver is occurring).

# basins	POP(ep2) > POP(ep1)	IRR(ep2) > IRR(ep1)	PCP(ep2) < PCP(ep1)
32	✓	✓	✓
78	✓	✓	✗
33	✓	✗	✓
24	✓	✗	✗
3	✗	✓	✓
23	✗	✓	✗
4	✗	✗	✓
7	✗	✗	✗

Across the examined 204 river basins of the COUNS, 32 (21.15% of the CONUS area) show an increase in population and irrigated land and a decrease in precipitation, which may suggest a loss of surface water extent, whereas 8 out of 204 present a decrease in population and irrigated land and an increase in precipitation, which could trigger a net gain in surface water. Six additional combinations are found, where either the anthropogenic drivers (one or both) or the climatic driver seem to concur to a net loss or gain of surface water extent.

4.3.3 Contributors of changes in surface water extent

The aforementioned combinations of anthropogenic and climatic drivers were compared against the net change in surface water extent. More specifically, population and irrigated land are considered to contribute to a net gain of surface water extent when they are decreasing, while precipitation is supposed to be an effective driver of surface water gain when it increases from the first to the second epoch. Conversely, when considering basins with a net loss of surface water extent, increasing population and irrigated land and decreasing precipitation should be responsible of surface water loss.

The importance of the anthropogenic and climatic contributors to changes in surface water extent was assessed by evaluating the overlap between river basins experiencing a reduction (or expansion) in surface water extent and river basins with an increase (or decrease) in anthropogenic drivers and a decrease (or increase) in the climatic driver. Therefore, the results obtained so far were then summarized in two maps describing in which river basins the drivers resulted to be responsible of a net surface water gain (Figure 4.13) and a net surface water loss (Figure 4.14), respectively.

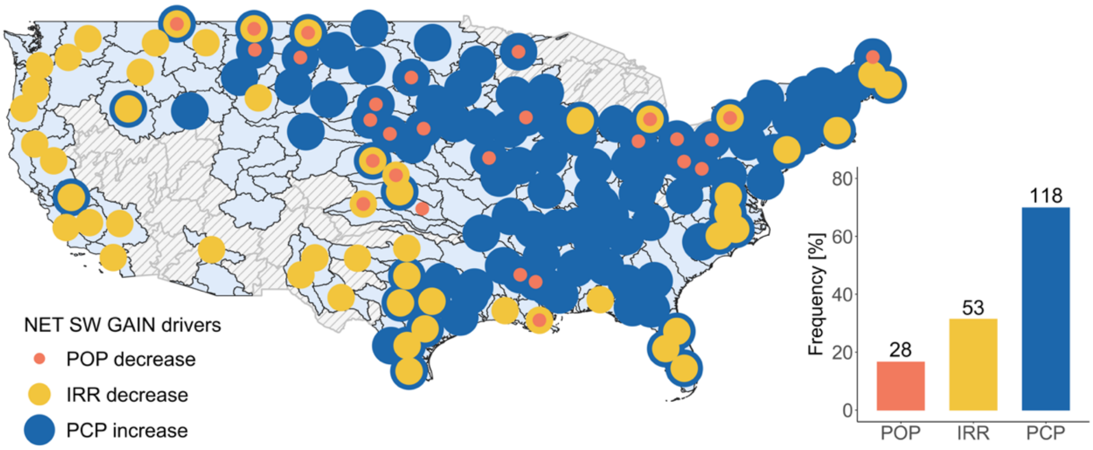

Figure 4.13 Spatial overlap of potential contributors to a net surface water gain. A gain of surface water extent is supposed to be triggered by decreasing population (orange circle) and irrigation (yellow circle), and increasing precipitation (blue circle). The histogram on the right shows the frequency of occurrence of each contributor to net surface water gain. The numbers over the bin of each contributor indicate the count of river basins affected by a net surface water gain and that specific contributor.

The most widespread driver of surface water gain is precipitation, followed by population and irrigation (see histogram in Figure 4.13). In particular, out of the 169 river basins with a net surface water gain, precipitation is found to increase in 118 river basins (covering 50.22% of the CONUS area), resulting to be the key driver of the expansion of surface water extent, especially in the eastern region of the US (Figure 4.13). Between the two anthropogenic drivers, irrigation is the most prominent one (53 river basins covering 26.36% of the CONUS area) and the reduction of irrigated land is mostly occurring in river basins located over the western region of the US (about 40% of the 53 river basins with an increasing irrigated land) and partially (almost 23% of the 53 river basins with an increasing irrigated land) along the East Coast (Zhang & Long, 2021). The selected anthropogenic and climatic drivers turned out to simultaneously contribute to the net gain of surface water extent observed in 6 river basins (covering 3.36% of the CONUS area), while in 24 river basins none of the drivers were contributors of the increase of surface water extent (covering 10.50% of the CONUS area).

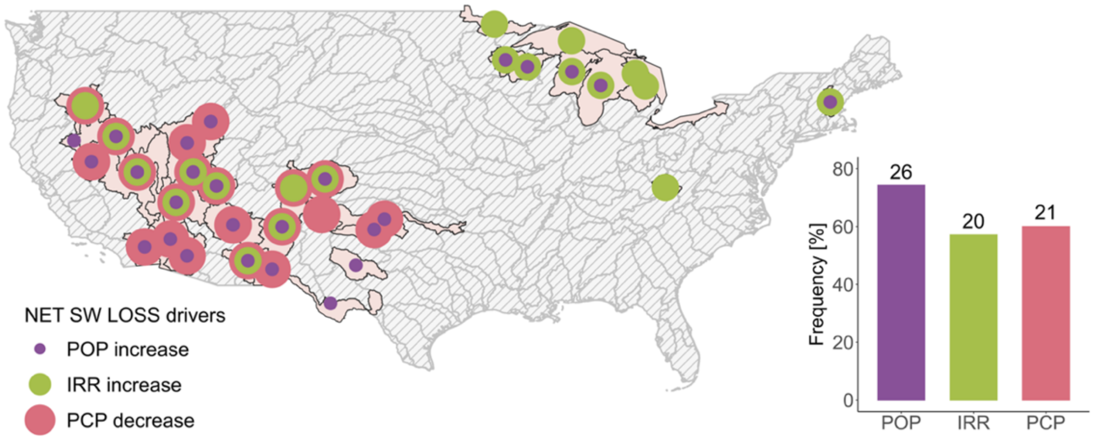

Figure 4.14 Spatial overlap of potential contributors to a net surface water loss. A loss of surface water extent is supposed to be triggered by increasing population (purple circle) and irrigation (green circle), and decreasing precipitation (pink circle). The histogram on the right shows the frequency of occurrence of each contributor to net surface water loss. The numbers over the bin of each contributor indicate the count of river basins affected by a net surface water loss and that specific contributor.

The most diffused driver of surface water loss is population, followed by precipitation and irrigation (see histogram in Figure 4.14). Specifically, out of the 35 river basins with a net loss of surface water, population increased in 26 river basins (covering 17.81% of the CONUS area), resulting to be the dominant driver of surface water loss either in the western and the eastern region of the US. A similar level of diffusion is also found for the increase in irrigated land and the decrease of precipitation, which contributed to the surface water loss of 20 (covering 15.19% of the CONUS area) and 21 (covering 16.94% of the CONUS area) river basins, respectively. In more detail, precipitation contributed to surface water loss in almost all the river basins (except one) of the southwestern region of the US, which are mainly characterized by an arid climate. Irrigation is another contributor to the decrease of surface water extent in some of the river basins of the southwestern area, although it mainly influenced the reduction of surface water found in all the 10 river basins located in the northeastern region of the US (Figure 4.14). The selected anthropogenic and climatic drivers resulted to simultaneously contribute to the net loss of surface water extent observed in 8 river basins (covering 10.65 % of the CONUS area), while in only 1 river basin none of the drivers were contributors to the reduction of surface water extent (covering 0.12 % of the CONUS area).

Similar results were obtained when the change in surface water extent was compared to the variations of the drivers within the main climatic regions of the CONUS and their subtypes

(Table 4.2). Specifically, in the tropical region and all its subtypes as well as in the "arid, steppe, hot" class the net gain of surface water resulted to be influenced by the combination of a reduction in irrigated land and an increase of precipitation. Precipitation increase is the only driver of the net gain of surface water found in the continental region and in some of its subtypes, in the temperate region, and the "temperate, no dry season, hot summer" class. The net surface water gain found in the "cold, dry & warm summer", the "temperate, dry & hot summer", and the "temperate, dry & warm summer" subtypes resulted to be generated by a reduction of irrigated land only. Finally, in the polar region, three subtypes of the temperate region, and two subtypes of the continental regions none of the drivers were observed to be contributing to the net surface water gain. Population growth and precipitation decrease resulted to contribute to the net surface water loss observed within the arid region, its subtypes, and in the "cold, dry & hot summer" class, confirming the findings obtained at the river basin level.

Overall, a heterogeneous contribution to surface water change (both gain and loss) was found to be induced by the considered anthropogenic and climatic drivers across the river basins of the CONUS. From the first to the second epoch most of the river basins has witnessed a net increase in the extent of surface water, indicating that the total loss has been compensated by the total gain, and this outcome can be mainly associated to an increase of precipitation and in some measure to a decrease of irrigated agriculture. However, in the river basins of the arid regions of southwestern US and in some river basins of the northeastern US the total gain did not counterbalance the total loss of surface water extent, producing a net loss of surface water, which was mostly caused by anthropogenic factors. In particular, population growth was the contributor governing the reduction of surface water extent. This result highlights the importance to shed light on the mechanisms of interaction between losses of surface water resources and human pressure, especially in view of future scenarios of urban population growth. For these reasons, RO2 illustrated in the next Chapter will focus only on losses of surface water, disregarding the overall net change of surface water extent obtained when considering also the contribution of possible surface water gains. Moreover, it will only examine the anthropogenic influence due to the presence of human settlements.

Table 4.2 Values of changes in surface water extent (SW), anthropogenic factors (population, POP, and irrigated land, IRR), and the climatic factor (precipitation, PCP) across the main climatic regions of the CONUS and their subtypes.

Climatic region/subtypes	**Area of CONUS [%]**	**ΔSW [km^2]**	**ΔPOP [# people]**	**ΔIRR [km^2]**	**ΔPCP [mm/yr]**
Continental	**40.47**	**8787.16 (2.40%)**	**6364175.37 (4.86%)**	**12196.13 (27.39%)**	**40.07 (4.28%)**
Cold, dry & hot summer	0.05	-0.51 (-0.58%)	88876.31 (33.80%)	-10.75 (-5.35%)	-15.61 (-2.85%)
Cold, dry & warm summer	2.69	153.07 (2.81%)	211046.55 (20.28%)	-201.06 (-14.67%)	-16.22 (-1.60%)
Cold, dry & cold summer	0.77	33.07 (6.07%)	228.04 (5.28%)	0.00 (0.00%)	-43.04 (-2.03%)
Cold, dry winter, hot summer	0.53	226.08 (12.69%)	10777.28 (5.12%)	154.81 (31.76%)	19.38 (3.78%)
Cold, dry winter, warm summer	0.58	403.60 (12.93%)	2580.18 (2.81%)	49.06 (25.27%)	38.21 (8.32%)
Cold, no dry season, hot summer	18.63	5991.05 (7.39%)	5451233.31 (4.78%)	11374.88 (30.70%)	52.63 (5.42%)
Cold, no dry season, warm summer	14.25	1872.93 (0.80%)	581856.41 (3.84%)	775.00 (15.99%)	52.71 (5.62%)
Cold, no dry season, cold summer	2.97	107.88 (0.27%)	17577.30 (16.80%)	54.19 (14.97%)	-21.47 (-2.98%)
Arid	**33.67**	**-2772.98 (-4.84%)**	**9167980.15 (26.62%)**	**-4330.06 (-4.52%)**	**-6.22 (-1.79%)**
Arid, desert, hot	2.30	-218.65 (-6.17%)	3074569.79 (45.68%)	-517.13 (-9.31%)	-17.23 (-8.43%)
Arid, desert, cold	5.65	-2083.05 (-16.41%)	956153.25 (28.34%)	-455.81 (-3.61%)	-9.69 (-3.75%)
Arid, steppe, hot	1.73	59.13 (2.68%)	1603766.01 (20.61%)	-141.88 (-5.41%)	24.10 (4.21%)
Arid, steppe, cold	23.98	-530.41 (-1.37%)	3533491.09 (21.34%)	-3215.25 (-4.29%)	-6.53 (-1.12%)
Temperate	**25.41**	**13961.84 (13.96%)**	**22036019.91 (18.63%)**	**7061.00 (13.73%)**	**28.48 (2.03%)**
Temperate, dry & hot summer	1.42	1180.51 (21.26%)	1846841.36 (12.83%)	-1231.31 (-11.85%)	-22.65 (-4.59%)
Temperate, dry & warm summer	2.51	259.66 (7.90%)	2097761.31 (12.70%)	-73.06 (-1.91%)	-44.35 (-3.47%)

Temperate, dry & cold summer	0.00	0.01 (8.21%)	0.19 (18.65%)	0.00 (0.00%)	-127.66 (-5.30%)
Temperate, no dry season, hot summer	21.19	12504.09 (13.77%)	18050062.70 (20.73%)	8363.19 (22.55%)	41.69 (3.17%)
Temperate, no dry season, warm summer	0.28	17.50 (4.94%)	41354.17 (14.74%)	2.19 (1.78%)	-51.15 (-0.96%)
Temperate, no dry season, cold summer	0.00	0.07 (75.96%)	0.17 (11.92%)	0.00 (0.00%)	-411.92 (-11.49%)
Tropical	**0.27**	**1543.27** **(23.05%)**	**1043244.20** **(20.29%)**	**-381.44** **(-18.61%)**	**95.91** **(6.70%)**
Tropical, rainforest	0.01	17.05 (18.48%)	159655.35 (22.05%)	-6.56 (-86.07%)	30.61 (1.93%)
Tropical, monsoon	0.08	590.18 (45.02%)	552493.50 (15.34%)	-96.75 (-32.61%)	100.81 (6.67%)
Tropical, savannah	0.18	936.04 (17.69%)	331095.35 (40.48%)	-278.13 (-15.94%)	97.55 (6.99%)
Polar (polar, tundra)	**0.18**	**20.90** **(13.92%)**	**33.20** **(3.50%)**	**0.00** **(0.00%)**	**-47.48** **(-3.94%)**

Note. A net surface water gain is highlighted in light blue, while a net loss of surface water is indicated in light red. Where drivers result to contribute to the net surface water gain/loss they are highlighted using the color convention adopted in Figure 4.13 and Figure 4.14. Percentages under variations values of surface water extent and its drivers indicate the relative change that occurred in the second epoch with respect to the first epoch.

5 Research Objective 2: Spatial distribution of surface water loss from urban areas

Urban areas host a significant fraction of population density and socio-economic activities relying on water supplies. It is well acknowledged that human societies have historically established along water bodies. In a recent study, Fang & Jawitz (2019) examined the evolution of human settlements location with respect to rivers that occurred in the CONUS between 1970 and 2010. They showed that cities of the US have been generally developed adjacent to major rivers and in arid regions the attractiveness of surface water resources is higher than in humid regions. Moreover, they noticed that urban areas are found to become less populated as the distance from rivers increases. Overall, by 2050 about 70% of the global population is expected to reside in cities and the resulting process of urban sprawl will likely affect both the quantity and quality of water resources surrounding urban areas worldwide (Padowski & Jawitz, 2012; McDonald et al., 2014; Boretti & Rosa, 2019; United Nations, 2019).

Surface water losses are known to expand in space as the nearest water sources get exhausted due to the development of new and existing urban areas (Padowski & Jawitz, 2012; Richter et al., 2013; Daniell et al., 2015; Hoekstra et al., 2018). Initially, local water from adjacent agricultural and rural regions is the main freshwater source for cities. However, while urban population grows and urban area expands, these local sources become insufficient to meet urban water needs, requiring the importation of freshwater from other river basins. As a result, the growth of urban water demand produces a progressive exploitation of freshwater sources, leading to a substantial reduction in water frequency observations close to urban areas, indicative of surface water loss, which in turn causes environmental, social, and economic impacts whose effects are going to affect increasingly larger areas (Richter et al., 2013; McDonald et al., 2014; Padowski & Gorelick, 2014). In particular, local surface water could be lost as a consequence of several human-induced processes, such as increasing water abstraction, groundwater exploitation, land drainage, and increased evaporation, with serious consequences for the integrity of freshwater ecosystems (Poff et al., 1997; Fitzhugh & Richter, 2004; Ceola et al., 2013; Sun & Caldwell, 2015; Pekel et al., 2016; Liyanage & Yamada, 2017;

Rodell et al., 2018). Indeed, surface water loss and river fragmentation due to a water-land transition have significant repercussions on riverine biodiversity and essential ecosystem services (McDonald et al., 2011c; Pekel et al., 2016; Grill et al., 2019; Botter & Durighetto, 2020). Such degradation of ecosystems and freshwater species has been extensively reported in the CONUS and it is expected to occur in other areas across the globe where the use of land and water is changing and population is growing (Fitzhugh & Richter, 2004). Therefore, it is crucial to gain a better understanding of the dynamics of interaction between urbanization and surface water, and in particular how the presence of human settlements influences the progressive loss of surface water resources, to find a balance between urban planning and water management policies that ensure water conservation and ecosystem protection (Vörösmarty et al., 2010; McDonald et al., 2011a; McGrane, 2016; Wada et al., 2016; Hoekstra et al., 2018; Paiva et al., 2020). All these pieces of evidence found in the literature are also confirmed by the results of the analysis illustrated in Chapter 4, which highlighted that the main factors responsible for a net surface water loss are the anthropogenic drivers, especially the increase of population.

The spatial interaction between two separate locations is primarily dependent on the geographical distance between them, and the intensity of such an interaction decreases as the locations are further away. This behavior is defined as the distance-decay effect and it is expressed in the First Law of Geography, which states that "everything is related to everything else, but near things are more related than distant things" (Tobler, 1970). Distance-decay is a fundamental concept in spatial sciences, and it has been widely applied to human and urban geography, spatial planning and analysis, as it allows to describe the occurrence or frequency of a pattern (Taylor, 1971; Fotheringham, 1981). For instance, in human geography distance-decay has been often used with a focus on transportation planning (Halás et al., 2014; Goel, 2018), ecological habitat variability and distribution (Goldmann et al., 2016), ecosystem services (Fernández, 2019), health risk assessment (Requia et al., 2016), and industry localization (Figueiredo et al., 2015).

Several studies on the proximity of human settlements to water have been carried out (Ceola et al., 2014; Fang et al., 2018; Mård et al., 2018; Fang & Jawitz, 2019; Liu et al., 2020). However, the spatial interaction between cities and surface water loss and its modeling through the distance-decay concept still remain to be explored. Moreover, this aspect has not been investigated with EO data, despite the availability of many consistent global products that accurately describe surface water dynamics and urban growth.

These are the reasons that motivate the analysis of the spatial interaction between built-up areas and surface water depletion. Specifically, this investigation aims at assessing the driving role of urban areas in the spatial distribution of surface water loss across the CONUS. It was assumed that irrigation and climatic factors, in particular precipitation change, did not contribute to surface water loss (i.e., water-land transition), which was also demonstrated by the outcomes of the previous analysis (i.e., RO1). Indeed, on average the total annual precipitation and the number of precipitation days have slightly increased in most of the CONUS, leading to a 0.5% increase of the total surface water area since 1984 (EPA, 2016; Pekel et al., 2016; Easterling et al., 2017; Bartels et al., 2020). Moreover, urban areas are considered to be a proxy of population as they are detected with a higher accuracy by remote sensing images. Actually, information on population distribution is derived from the combination of maps of urban areas developed from EO images and census data (see also Subsection 3.2.2 of Chapter 3 for more details). Finally, given that human settlements data of the GHSL dataset (Corbane et al., 2019) illustrate the evolution of urban areas until 2014 (as described in Subsection 3.2.2 of Chapter 3), the time period 1984-2018 was selected for the extraction of surface water loss data adopted in this analysis, instead of the 1984-2020 time window inspected in RO1, to optimize the overlap between data temporal coverage. The aim of this analysis is to provide an answer to the following questions, already introduced in Chapter 1: (Q2a) where does urbanization cause surface water loss? (Q2b) How does the frequency of surface water loss change as the distance from human settlements increases?

5.1 Surface water loss and urban area data

Also for the investigation of the spatial influence of urban areas on losses of surface water, datasets obtained from remote sensing data were processed to define two binary maps: the Surface Water Loss map and the Urbanization map (Palazzoli et al., 2021). The Surface Water Loss map identifies the geographical location of pixels that experienced a reduction in the frequency of water observations, leading to a conversion from water to land at the end of the period 1984-2018 (blue pixels in Figure 5.1). This map was derived from the Surface Water Transitions layer of the Global Surface Water dataset, which describes the changes in the seasonality of any surface water body open to the sky and larger than 30 m by 30 m as open water, including fresh and saltwater (Pekel et al., 2016). As already mentioned in Subsection 3.2.1 of Chapter 3, the Surface Water Transitions layer describes the evolution of surface water state that took place between the first and last year of observations time series, by showing any conversion among three states: permanent surface water, seasonal surface water, and land (i.e., areas without any water). The class of transition assigned to each water pixel is defined based on the variation of its frequency of observation. In this analysis the pixels classified as lost permanent, lost seasonal, ephemeral permanent, and ephemeral seasonal surface water were selected to identify locations that experienced a surface water loss (i.e., a water-land transition) during the time window from 1984 to 2018 and they were extracted to produce the Surface Water Loss map. Lost permanent (or seasonal) surface water indicates a conversion of permanent (or seasonal) water into land. Ephemeral permanent (or seasonal) surface water identifies locations where surface water resources are permanent (or seasonal) for some of the intervening years, but no water is detected in the first and last year of the observational period (Pekel et al., 2016). Although the nature of the factor that caused the presence or loss of surface water (either permanent, seasonal, or ephemeral) is not considered in this study, a check for the stability of each surface water state that we classified as lost was carried out by looking at the frequency of surface water occurrence between 1984 and 2018 provided by the Surface Water Occurrence layer (SWO) of the Global Surface Water dataset (Pekel et al., 2016), which has been already introduced in Subsection 3.2.1 of Chapter 3. In particular, the occurrence values associated to the pixels of the selected classes of surface water transition included in the Surface Water Loss map (i.e., lost permanent, lost seasonal, ephemeral permanent, and ephemeral seasonal) were extracted. Out of the 85,001,873 pixels of surface water loss considered in the study area of the CONUS, 12.90% are classified as lost permanent, 29.47% are lost seasonal, 1.92% are ephemeral permanent, and 55.71% are ephemeral seasonal. As expected, the distribution of the values of water occurrence associated to each class of surface water loss averaged over the river basins of the CONUS shows a decreasing trend from lost permanent, to ephemeral permanent, lost seasonal, and ephemeral seasonal, with median values equal to 50%, 30%, 18%, and 10%, respectively (Figure A3, Figure A4, and Figure A5). This outcome proves a significant presence of water in correspondence of the surface water loss pixels during the observation period, which eventually resulted to be lost in 2018. Moreover, the size-distribution of lost water areas was investigated through the identification of clusters of surface water loss. The number of surface water loss clusters results to grow moving from West to East (Figure A6a), while the spatial extent of the largest clusters of surface water loss increases in the opposite direction (Figure A6b). Finally, although the presence of human-managed surface water reservoirs and well fields was not explicitly considered in this analysis, surface water losses associated to such features are implicitly included in our Surface Water Loss map, as specified in the dataset used to derive this map (Pekel et al., 2016). In fact, dams reduce the variability of the downstream river flow (Granzotti et al., 2018), while well fields induce an increase of the groundwater recharge (Xu & Beekman, 2019), and both these effects imply a reduction in surface water extent.

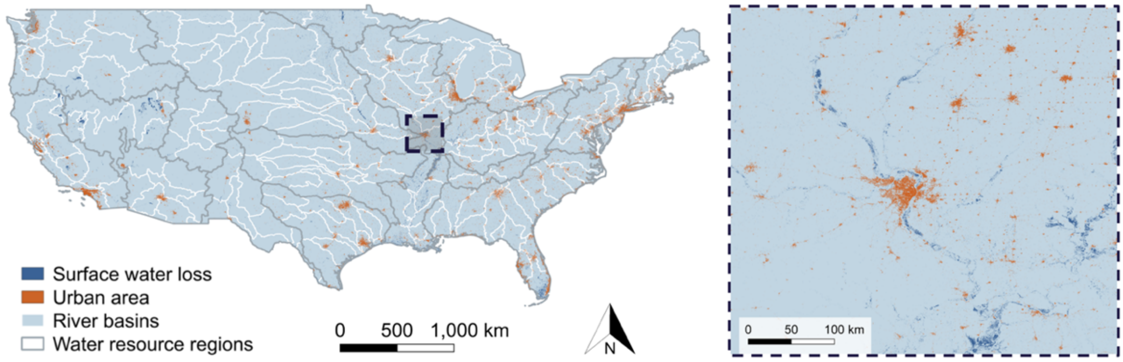

Figure 5.1 Surface water loss locations and urban areas across the river basins and water resource regions of the CONUS. Locations that experienced surface water loss are colored in blue. The extent of urban areas is shown in orange. The boundaries of the 204 river basins are depicted in white, while the 18 water resource regions are highlighted with a bold grey line. The dark blue dashed box represents a zoom-in over the area around the city of Saint Louis and the Mississippi River.

The Urbanization map describes the most recent extent of urban areas reached at the end of 2014 (orange pixels in Figure 5.1). As for the Urban Area maps defined in Section 4.1 of Chapter 4, also the Urbanization map was derived from the GHS-BUILT layer of the GHSL dataset (Corbane et al., 2019), by extracting all the pixels of built-up areas developed during all the four epochs (until 1975, from 1975 to 1990, from 1990 to 2000, and from 2000 to 2014), i.e., urban areas developed up to 2014. The maximum extent of the urban agglomerations derived from the Urbanization map and found within each river basin of the CONUS indicates the presence of larger urban clusters along the West coast and in the Eastern US (Figure A7).

5.2 Assessment of the spatial influence of urban areas on surface water loss

In this Thesis, the influence of urban areas on the spatial distribution of surface water loss across the CONUS was evaluated and modeled through the application of the distance-decay concept to data acquired from satellite sensors (Palazzoli et al., 2022). Surface water loss was defined as a reduction in water frequency observations, regardless of the cause (i.e., anthropogenic or climatic) and loss magnitude, that generates the conversion from water to land. Therefore, the observed frequency of occurrence of surface water loss with respect to distance from urban areas was examined in bins of 3 km across the CONUS (Figure 5.2a). Afterwards, the observed trend of the spatial distribution of surface water losses as a function of distance from urban areas was reproduced with a distance decay model (Figure 5.2b).

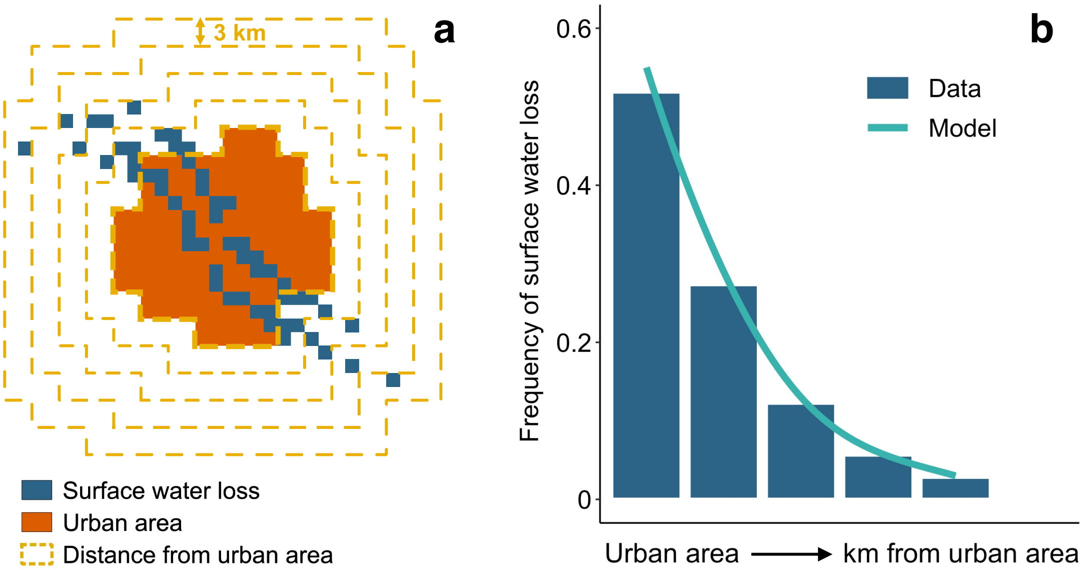

Figure 5.2 Schematic representation of the spatial interaction between surface water loss locations and urban areas hypothesized in this analysis. **a.** Geographical distribution of surface water loss and urban areas across 3 km wide distance classes. **b.** Comparison between observed and modeled frequency of occurrence of surface water loss, showing a decreasing pattern as the distance from urban areas increases.

5.2.1 Observed frequency of surface water loss occurrence

The geographical distance of surface water loss pixels from urban areas was estimated using the Euclidean distance, which measures the length of a straight line connecting pairs of locations. As a conservative approach, it was assumed that urban areas can reach all nearby surface water resources leading to a conversion from water to land, i.e., surface water loss. The assumption that all urban areas access the closest surface waters is a solid working hypothesis, as it reflects the strategy of cities to reduce the distance from which they import water resources (McDonald et al., 2011b). Although other physical factors (such as terrain elevation, road networks, and water supply systems) might have been considered in the definition of the distance metric, the Euclidean distance was adopted since it provides an objective and global reference while also being a relevant design driver for technological networks. Moreover, it represents the most common measure of geographical distance used in distance-decay applications (Halás et al., 2014; Goldmann et al., 2016; Artell et al., 2019). The Euclidean distance allows to define a simple model that reproduces the observed spatial interaction between surface water loss and urbanization, avoiding too many independent variables that would otherwise enter the distance-decay function, increasing its level of complexity and related model uncertainty. Finally, in the CONUS there are multiple urban areas located at different distances from each other and mutually interacting. Such an interaction is implicitly included in this analysis through the Euclidean distance, which is here considered to be a proxy of the radius of influence of cities.

The Euclidean distance of surface water loss from the boundaries of urban areas (Figure 5.2a) was computed across each spatial aggregation x here considered (i.e., river basin, $x = b$, water resource region, $x = WRR$, and the CONUS, $x = CONUS$). Afterwards, the values of distance were divided in bins having a constant width and counts of surface water loss pixels within each distance bin d_{ij} were aggregated to calculate the frequency of occurrence of surface water loss $f_x(d_{ij})$ (histogram in Figure 5.2b) as follows:

$$f_x\left(d_{ij}\right) = \frac{swl_x(d_{ij})}{swl_{x,tot}} \tag{5.1}$$

where $swl_x(d_{ij})$ is the count of surface water loss locations in the considered spatial aggregation x between distances i and j (with i and j ranging from 0 to $d_{x,max}$, i.e., the maximum distance reached in x), while $swl_{x,TOT}$ is the total count of surface water loss locations observed inside the considered spatial aggregation x.

The 3 km wide distance bin was selected based on the results of a sensitivity analysis that compared the frequency of occurrence of surface water loss obtained with aggregations at 1, 3, and 5 km wide distance bins. The width of 3 km resulted to be the optimal compromise between noise reduction and level of detail (Figure A8). This aggregation was applied until 99 km of distance from urban areas (i.e., 0-3 km, 3-6 km, …, 96-99 km distance bin).

In addition, the observed average distance of surface water loss locations from urban areas, $\langle d_x \rangle$, was estimated across each spatial aggregation x as follows:

$$\langle d_x \rangle = \frac{\sum_{k=1}^{swl_x} d_k}{swl_{x,tot}} \tag{5.2}$$

where d_k is the distance associated to a generic surface water loss location.

5.2.2 Distance-decay model of surface water loss occurrence

By assuming that the influence of urbanization on surface water loss locations declines as the distance of these locations from urban areas increases, a probabilistic model capable of reproducing this distance-decay behavior was defined (solid line in Figure 5.2b). The function describing the measure and shape of the decreasing spatial interaction is called distance-decay model or gravity model, and many forms of such models have been developed so far. Usually, gravity models do not have a linear shape and they are generated through a distance transformation of the original data, which generally leads to the adoption of a power or exponential law, as well as Pareto and log-normal functions (Taylor, 1971; Halás et al., 2014; Chen, 2015). Finally, sometimes it might result necessary to adopt more sophisticated functions, presenting a bell shape (i.e., an inflection point) and described by two parameters, such as the Weibull and squared Cauchy functions (Halás et al., 2014). Here, the distance-decay behavior was modeled with a truncated exponential probability distribution, which describes a decreasing trend of the frequency of occurrence of surface water loss pixels, so that the maximum probability of finding surface water loss occurs at a distance close to the urban agglomeration and exponentially declines with increasing distance. The selection of the exponential probability distribution is motivated by the fact that the exponential decay is among the most employed distance-decay functions, with several applications in different fields (Zhang, 2011; Martínez & Viegas, 2013; Figueiredo et al., 2015; Chen & Huang, 2018). Moreover, the truncated version of the function was adopted because, by definition, the distance reaches a finite maximum value $d_{x,max}$ in each spatial aggregation x, and it allows to consider the presence of multiple urban areas and their radius of influence.

The probability of occurrence of surface water loss locations as a function of the distance from urban areas, $p_x(d_{ij})$, across each spatial aggregation x reads as follows:

$$p_x(d_{ij}) = \alpha_x e^{-\beta_x d_{ij}} \tag{5.3}$$

where α_x [-] is the frequency of occurrence of surface water loss locations in the initial 3 km wide distance bin (0-3 km), and β_x (> 0 [km^{-1}]) represents the decay rate of the model, describing the rate of decline in spatial interaction. The higher β_x, the steeper is the decrease in $p_x(d_{ij})$ with increasing distance from urban areas.

The parameters α_x and β_x in Equation 5.3 were estimated through a non-linear regression of the probability of occurrence $p_x(d_{ij})$ versus the observed frequency of surface water loss locations $f_x(d_{ij})$, by assuming that at least values in three distance bins are available in order to get a robust fit ($d_{x,max} > 6$ km). The goodness of fit was assessed through the evaluation of the Pearson's correlation coefficient r. In addition, the standard error associated to the model fit derived for each spatial aggregation x was calculated to evaluate the distance of observed values from the regression line of the model. This value provides an estimate of the prediction interval with 5% significance level, evaluating prediction uncertainty.

Finally, the theoretical average distance of surface water loss locations from urban areas (i.e., the expected value of the truncated exponential distribution), $\langle \hat{d}_x \rangle$, was analytically derived from Equation 5.3 across each spatial aggregation x as follows:

$$\langle \hat{d}_x \rangle = \frac{1-e^{-\beta_x d_{x,max}}(1+\beta_x d_{x,max})}{\beta_x(1-e^{-\beta_x d_{x,max}})} \tag{5.4}$$

To check for the reliability of Equation 5.3 in reproducing the observed distance-decay pattern of surface water loss locations, the observed and the theoretical average distances, $\langle d_x \rangle$ from Equation 5.2 and $\langle \hat{d}_x \rangle$ from Equation 5.4, were compared for each spatial aggregation x.

5.2.3 Overall surface water extent *versus* surface water loss: comparison of distance decay patterns

The definition of the distance-decay model here presented is based on the reasonable assumption that all urban areas can access the closest surface water resources. Given this hypothesis, the decay of surface water loss was compared to the decay of the overall extent of surface water with distance from urban areas at the river basin level to further test if more surface water loss is occurring close to urban areas, rather than far from them. The overall extent of surface water was extracted from the Water Extent layer of the Global Surface Water dataset (Pekel et al., 2016), which has been already introduced in Subsection 3.2.1 of Chapter 3. To avoid biases due to large water bodies, the Euclidean distance from urban areas was calculated only at the boundaries of surface water bodies, which are also the resources that are the most likely to be exhausted because of human withdrawals. Similarly to the approach followed for the surface water loss decay, a non-linear regression was performed and the distance-decay model parameters were evaluated, based on the overall extent of surface water. A decay rate of surface water loss β_b larger (smaller) than the decay rate of the overall extent of surface water β_b^{sw} signals an area where more surface water loss is occurring close to (far from) urban areas.

5.2.4 Influence of climate

To investigate the influence of climate on the spatial interaction between urban areas and surface water losses, the spatial distribution of surface water loss locations and the associated variability of the model parameters at the river basin level, α_b and β_b, were investigated over the main Köppen-Geiger climatic zones (Beck et al., 2018), i.e., tropical, arid, temperate, continental, and polar (see Figure 3.1). The variability of parameters α_b and β_b in the climatic zones was evaluated as a weighted average given by the number of locations of surface water loss associated to each climatic zone found in every river basin of the CONUS. In particular, for a given climatic zone and river basin, the weight was defined as the ratio between the number of surface water loss locations within the portion of basin in that climatic zone (i.e., locations sharing the same values of α_b and β_b) and the total number of surface water loss locations found in the same climatic region.

Finally, also the distribution of the decay rate of the overall extent of surface water, β_b^{sw}, was evaluated across the Köppen-Geiger climatic regions to perform a comparison with the values previously found for the distance-decay of surface water loss, β_b.

5.3 Results

5.3.1 Observed spatial interaction between surface water loss and urban areas

It was found that the observed frequency of occurrence of surface water loss locations steadily decreases as the distance from urban areas increases across the whole study area, at the river basin, water resource region, and CONUS level. This result applies to any geographical position, climatic zone, and physiographic property. Figure 5.3 clearly shows this outcome for the CONUS (diamonds in Figure 5.3b) and for four water resource regions and related river basins (circles in Figure 5.3c-j). Similar results were also found for the remaining river basins and water resource regions, thus confirming that surface water losses are consistently located in the proximity of urban areas (see Figure 5.4 for the remaining 14 water resource regions).

5.3.2 Spatial interaction between surface water loss and urban areas: distance-decay model application

The probability of occurrence of surface water loss locations was then computed as a function of distance from urban areas. The application of the distance-decay model defined in Equation 5.3, based on the selected 3 km wide distance bin, shows that all 18 water resource regions and 191 river basins (covering 96% of the CONUS area) are successfully fitted by the distance-decay model (Figure 5.3a and Figure 5.4), with r values ranging from 0.974 to 0.999 and from 0.676 to 0.999, for the water resource regions and the river basins, respectively. In the remaining 13 river basins, Equation 5.3 could not be applied at the selected 3 km wide distance bin because of data paucity (i.e., $d_{x,max} \leq 6$ km, meaning that data are available in less than three distance bins). However, for these river basins, Figure 5.3a shows r values ($r \geq 0.952$) obtained with 1 km wide distance bins (see river basins with a dark grey line pattern). Data and model comparison for the four aforementioned water resource regions and related river basins are shown in Figure 5.3c-j. A statistically significant fit ($r = 0.997$) is also found when the distance-decay model is applied to the CONUS (Figure 5.3b), proving the reliability of the mathematical interpretation of the influence of urbanization on the spatial distribution of surface water loss at different levels of spatial aggregation described in Subsection 5.2.2 of Chapter 5. Table 5.1 provides the main physical and climatic properties and model parameters for the CONUS and the selected water resource regions and river basins shown in Figure 5.3. The entire list of the main physical and climatic properties and model parameters for the 18 water resource regions and the 204 river basins can be found in Table B1.

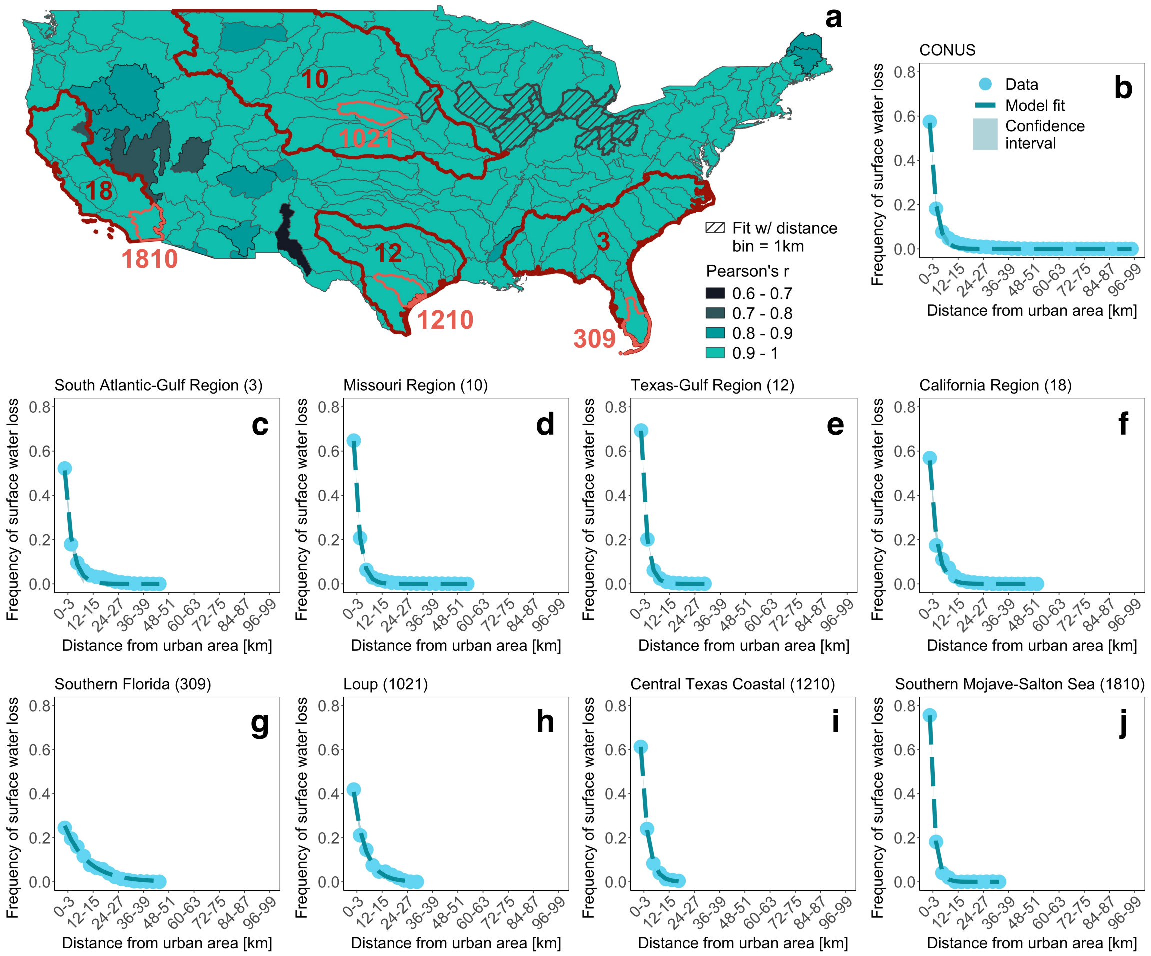

Figure 5.3 Performance of the distance-decay model reproducing the observed frequency of occurrence of surface water loss from urban areas, based on a 3 km wide distance bin. **a.** Spatial distribution of model performance, where river basins are colored according to their Pearson's correlation coefficient. River basins where the model fit is obtained with a distance bin of 1 km are indicated with a dark grey line pattern. Water resource regions (3, 10, 12, 18) and river basins (309, 1021, 1210, 1810) shown in panels c-j are highlighted with a thicker border. **b.** Frequency of occurrence of surface water loss locations and model fit obtained for the CONUS. Confidence intervals represent the standard error associated to the model fit. **c-f.** Frequency of occurrence of surface water loss locations and model fit obtained for the selected water resource regions. **g-j.** Frequency of occurrence of surface water loss locations and model fit obtained for the selected river basins.

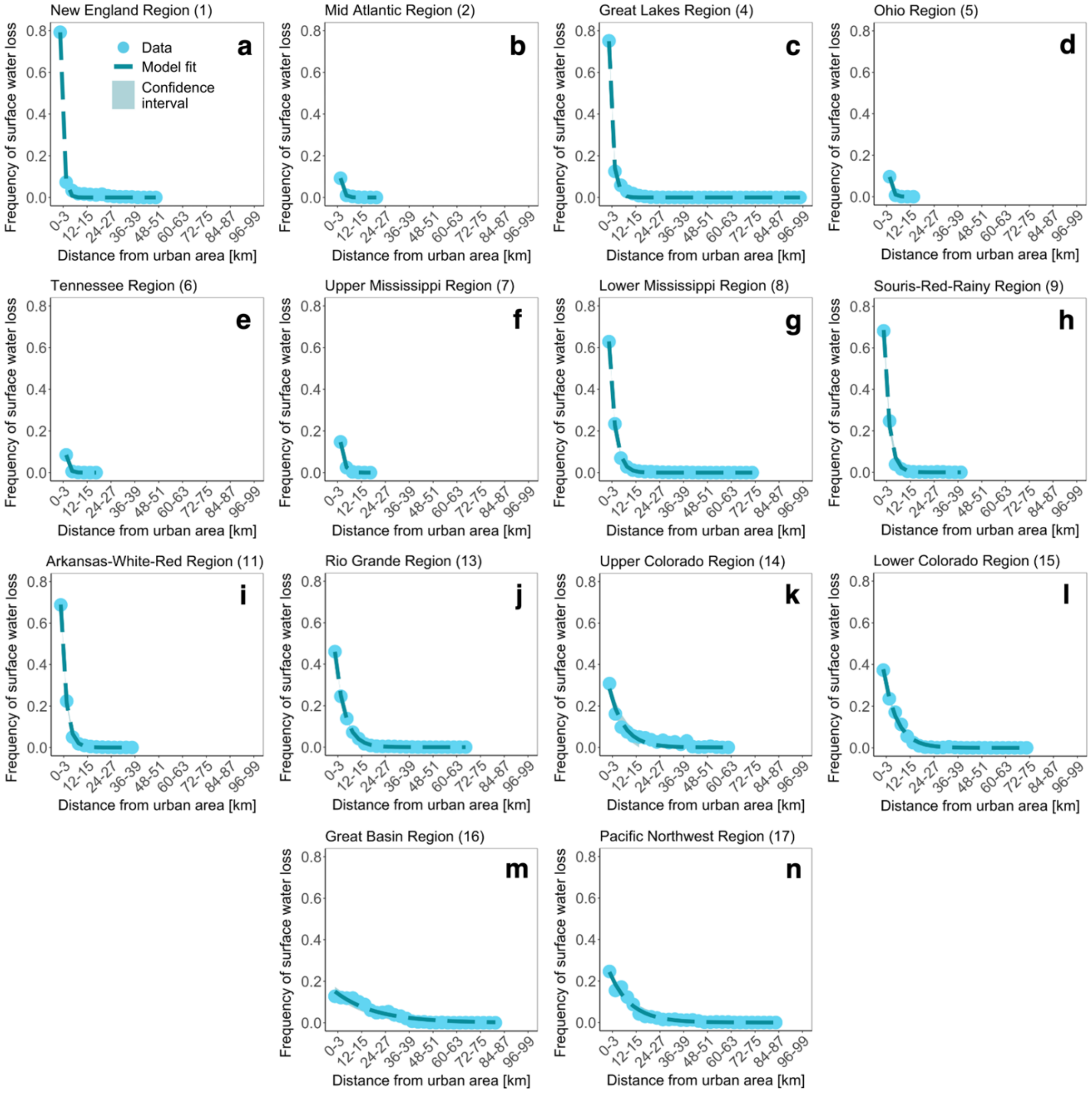

Figure 5.4 Performance of the distance-decay model reproducing the observed frequency of occurrence of surface water loss from urban areas in the 14 water resource regions of the CONUS (panels a-n) that are not shown in Figure 5.3, based on a 3 km wide distance bin.

Table 5.1 Main physical and climatic properties and model fit results, based on a 3 km wide distance bin, for the CONUS and four representative water resource regions and related river basins, shown in Figure 5.3.

Water resource region/river basin name (ID)	**Area [km^2]**	**Average elevation ± std dev [m]**	**Climatic regions and coverage percentage**	**α_x [-]**	**β_x [km^{-1}]**	**r**	**$\langle d_x \rangle$ [km]**	**$\langle \tilde{d}_x \rangle$ [km]**
CONUS	7,744,303	-	Continental (40.47%), Arid (33.67%), Temperate (25.41%), Tropical (0.27%), Polar (0.18%)	0.570	0.348	0.997	5.304	2.870
South Atlantic-Gulf Region (3)	695951	110 ± 118	Tropical (59.48%), Temperate (40.52%)	0.512	0.295	0.994	5.407	3.391
Southern Florida (309)	42136	12 ± 9	Tropical (59.48%), Temperate (40.52%)	0.255	0.093	0.996	8.992	10.140
Missouri Region (10)	1323835	996 ± 620	Continental (99.94%), Temperate (0.06%)	0.646	0.376	1.000	3.653	2.658
Loup (1021)	39214	825 ± 188	Continental (95.29%), Arid (4.71%)	0.408	0.182	0.995	5.946	5.380
Texas-Gulf Region (12)	464006	370 ± 348	Arid (85.42%), Temperate (14.58%)	0.692	0.407	1.000	2.703	2.457
Central Texas Coastal (1210)	44227	160 ± 170	Temperate (99.94%), Arid (0.06%)	0.613	0.318	1.000	3.189	3.099
California Region (18)	416156	888 ± 724	Temperate (77.67%), Arid (21.74%), Continental (0.59%)	0.558	0.312	0.993	4.245	3.202

Southern Mojave-Salton Sea (1810)	41361	548 ± 470	Arid (93.38%), Temperate (6.4%), Continental (0.22%)	0.756	0.475	1.000	2.244	2.103

Note. α_x and β_x are the distance-decay model parameters; r is the Pearson's correlation coefficient; $\langle d_x \rangle$ and $\langle \hat{d}_x \rangle$ are the observed and theoretical average distance, respectively. The first row reporting the values for the CONUS does not contain any ID nor the elevation with its standard deviation, which is not a significant information for such a large area.

The reliability of the distance-decay model was tested by comparing the observed and theoretical average distances of surface water loss locations from urban areas ($\langle d_x \rangle$ and $\langle \hat{d}_x \rangle$ from Equation 5.2 and Equation 5.4) in each level of spatial aggregation here considered, namely river basins, water resource regions, and CONUS. In what follows, results refer only to the CONUS, the 18 water resource regions, and the 191 river basins whose data were fitted by Equation 5.3 using a 3 km wide distance bin. Figure 5.5a shows that pairs of observed and theoretical average distances at the river basin level are well correlated, as the slope of the linear regression is equal to 1.00 ($R^2 = 0.84$, *p-value* << 0.05). A comparable and statistically significant correlation is also found for the 18 water resource regions (slope = 1.06, $R^2 = 0.87$, *p-value* << 0.05). The black diamond depicting the average distances for the CONUS falls marginally under the regression lines found for river basins and water resource regions, meaning that the distance-decay model underestimates the observed distance at which on average surface water loss occurs at the continental scale (see also values reported in Table 5.1). Results from the linear correlation demonstrate the consistency of the model in reproducing the observed spatial pattern, as the truncated exponential probability distribution is able to predict the distance from urban areas at which on average surface water loss may occur. Figure 5.5b depicts the comparison between the frequency distribution of the observed and theoretical average distance of surface water loss occurrence and it highlights that in the majority of the river basins surface water loss takes place in the proximity of urban areas, based on both the observed data and the model estimates. Specifically, it is noted that more than half of the river basins (109 out of 191) has an observed average distance smaller than 3 km (first bin of the histogram in Figure 5.5b).

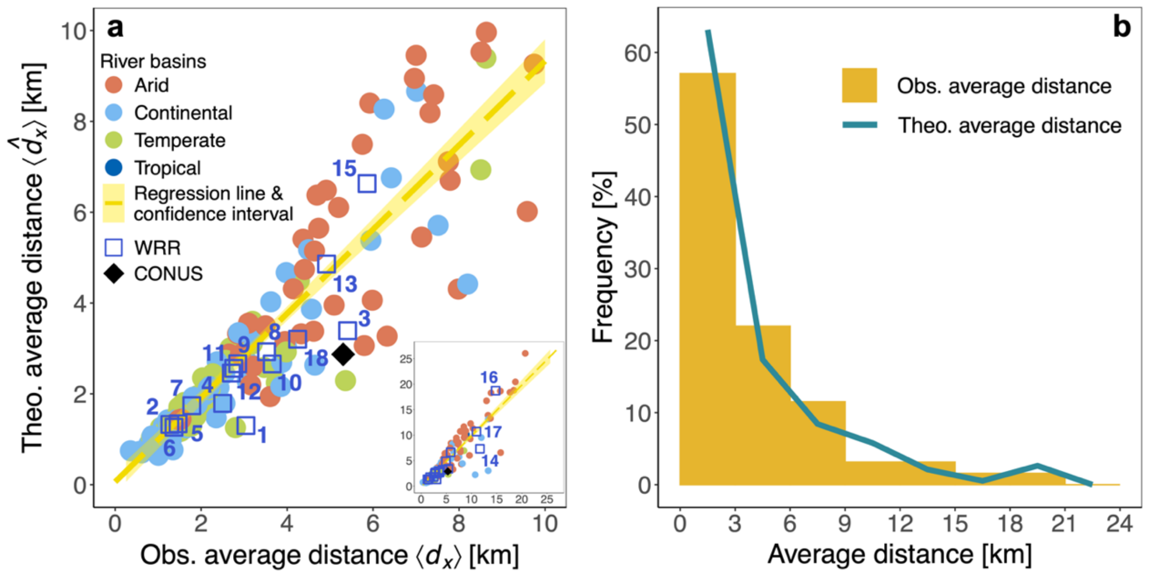

Figure 5.5 Comparison between the observed and theoretical average distance of surface water loss locations from urban areas ($\langle d_x\rangle$ and $\langle\hat{d}_x\rangle$) based on a 3 km wide distance bin and their frequency distribution. **a.** Correlation between observed and theoretical average distances of surface water loss locations. Results from the three levels of spatial aggregation (river basins, water resource regions, and the CONUS) are shown. Circles (whose color identifies the prevalent climatic region) show pairs of observed and theoretical distances obtained for the 191 river basins, blue squares are used to represent the 18 water resource regions (WRRs), while the black diamond identifies the same distances calculated for the CONUS. The linear regression between observed and theoretical distances at the river basin level is depicted by the yellow dashed line ($\langle\hat{d}_b\rangle = -0.13 + 1.00\ \langle d_b\rangle$) and its coefficient of determination R^2 is 0.84. The light yellow area represents the 95% confidence interval of the linear regression. The linear regression between observed and theoretical distances at the water resource region level (not shown) is the following: $\langle\hat{d}_{WRR}\rangle = -0.73 + 1.06\ \langle d_{WRR}\rangle$. **b.** Frequency distribution of observed and theoretical average distances of surface water loss locations at the river basin level.

To gain a deeper insight into the distance-decay behavior detected in the study area of the CONUS, the spatial variability and the frequency distribution of the model parameters α_x and β_x were further analyzed (Figure 5.6). Higher values of α_x and β_x imply a more concentrated loss of surface waters in the proximity of urban areas and a quicker decrease in surface water loss frequency as the distance from urban areas increases, respectively. As before, results refer only to the 18 water resource regions and 191 river basins for which Equation 5.3 fitted the data using a 3 km wide distance bin (i.e., river basins with a line pattern in Figure 5.3a are excluded). Values of α_b, as derived from river basins, range from 0.095 to 0.990, with the highest values found in river basins located in the eastern part of the CONUS and partially along the West Coast (Figure 5.6a), where the largest surface water withdrawals occurred (Dieter et al., 2018). Mean and median values of α_b are 0.651 and 0.724, respectively (Figure

5.6b), and 72% of the river basins presents more than half of surface water loss within 3 km from urban areas. In the 18 water resource regions α_{WRR} ranges from 0.151 to 0.908, with a mean value of 0.610 and a median equal to 0.666 (Figure 5.7a). For the CONUS, α_{CONUS} equals 0.570 (Table 5.1), thus confirming the concentration of surface water loss in the immediate proximity of urban areas.

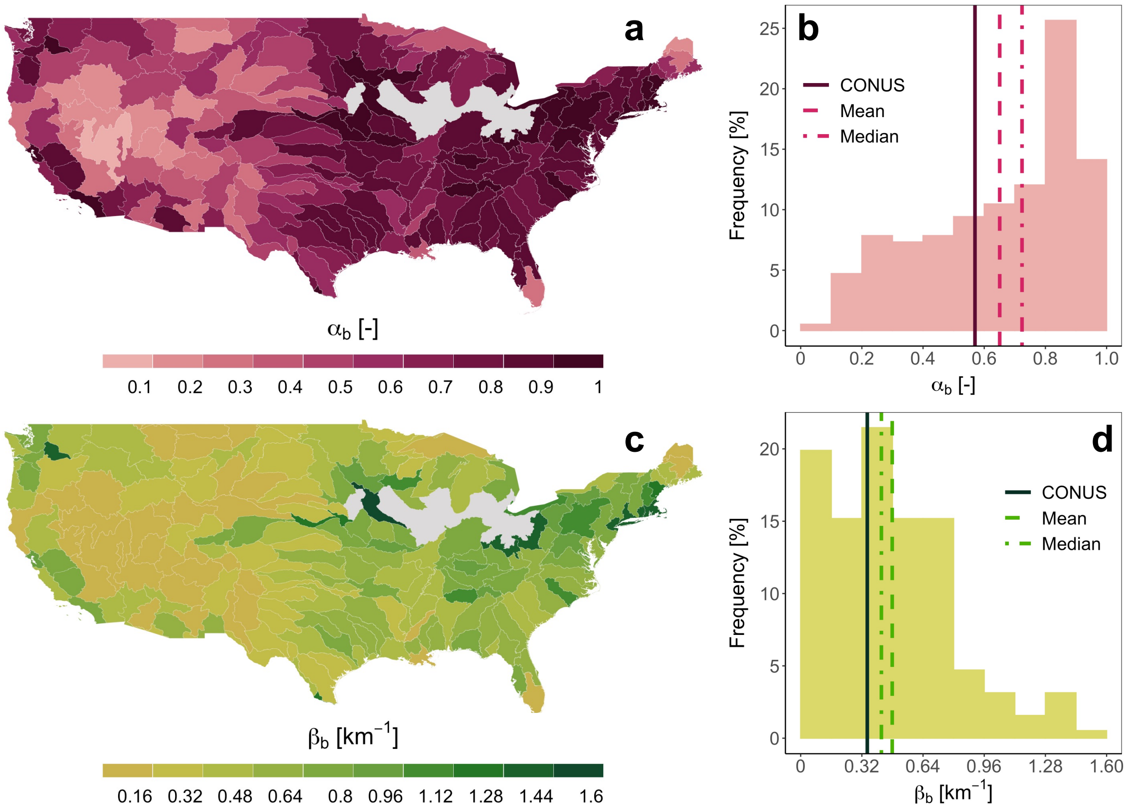

Figure 5.6 Spatial variability and frequency distribution of α_b and β_b parameters of the distance-decay model based on a 3 km wide distance bin and applied at the river basin level. **a.** Spatial variability of α_b. River basins that are not fitted by the model using a 3 km wide distance bin are indicated in light grey. **b.** Frequency distribution of α_b. The dashed line and the dot-dash line represent the mean and the median values, respectively, as derived from river basins, while the solid line depicts α_{CONUS}. **c.** The same as panel a, but for the decay rate β_b. **d.** The same as panel b, but for the decay rate β_b.

Regarding the decay rate β_x, values at the river basin level β_b range from 0.028 to 1.546 km^{-1}, with the highest values mainly found across the eastern part of the CONUS (Figure 5.6c), where most of urban areas are located (US Census, 2021). Mean and median values are 0.479 km^{-1} and 0.422 km^{-1}, respectively, with the majority of river basins (92%) showing a value smaller than 1 km^{-1} (Figure 5.6d). In the remaining 8% of the river basins, where $\beta_b > 1$ km^{-1}, a rapid decrease of surface water loss in space is found, indicating that the interaction between human settlements and surface water resources takes place over a shorter distance and, thus, only surface water resources close to cities are affected by urban areas.

In the 18 water resource regions β_{WRR} ranges from 0.050 to 0.790, with a mean value of 0.407 and a median equal to 0.376 (Figure 5.7b). For the CONUS, β_{CONUS} is equal to 0.348 km^{-1} (Table 5.1). Results based on 1 and 5 km wide distance bins are shown in Figure B1 and Figure B2 for river basins, and in Figure B3 and Figure B4 for water resource regions.

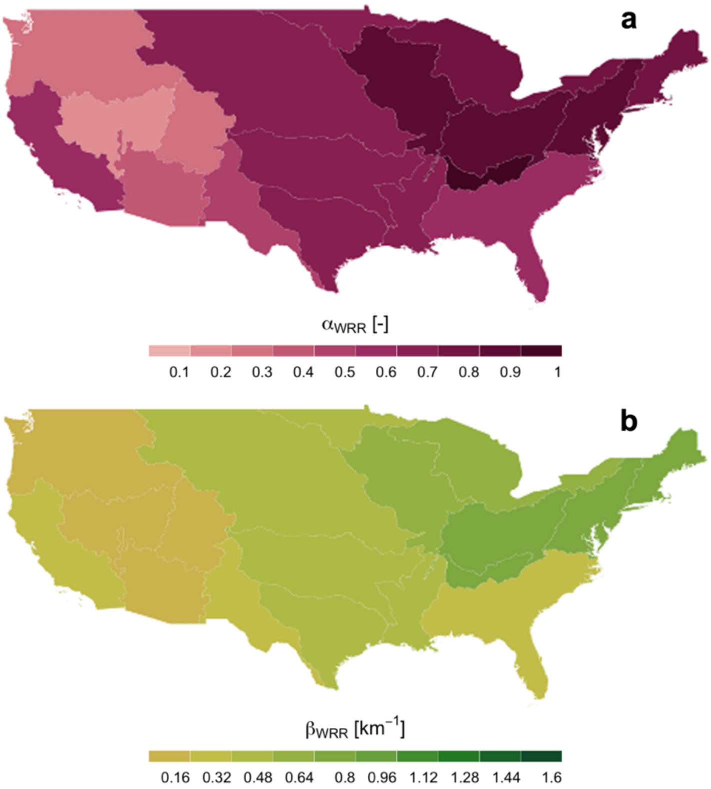

Figure 5.7 Spatial variability of α_{WRR} and β_{WRR} parameters of the distance-decay model based on a 3 km wide distance bin and applied at the water resource region level. **a.** Spatial variability of α_{WRR}. **b.** Spatial variability of β_{WRR}.

In addition, it was verified if the variability of α_b and β_b model parameters reflects heterogeneities of urban attributes, such as total urban population, urban population change, and urban area change. To this aim, data of urban population and urban area were extracted from the GHS-POP and GHS-BUILT layers provided by the GHSL dataset (Corbane et al., 2019), and described in Subsection 3.2.2 of Chapter 3. Since population and built-up area data from GHSL dataset are available only for 1975, 1990, 2000, and 2015 (2014 for built-up area), it was assumed that urban population detected in 1990 and 2015 and urban area found in 1990 and 2014 are a reasonable representation of the urban population and the level of urbanization during the first and last year of the period 1984-2018. The difference between urban population (or urban area) values in 2015 (or 2014) and 1990 was used to quantify urban population (or urban area) change.

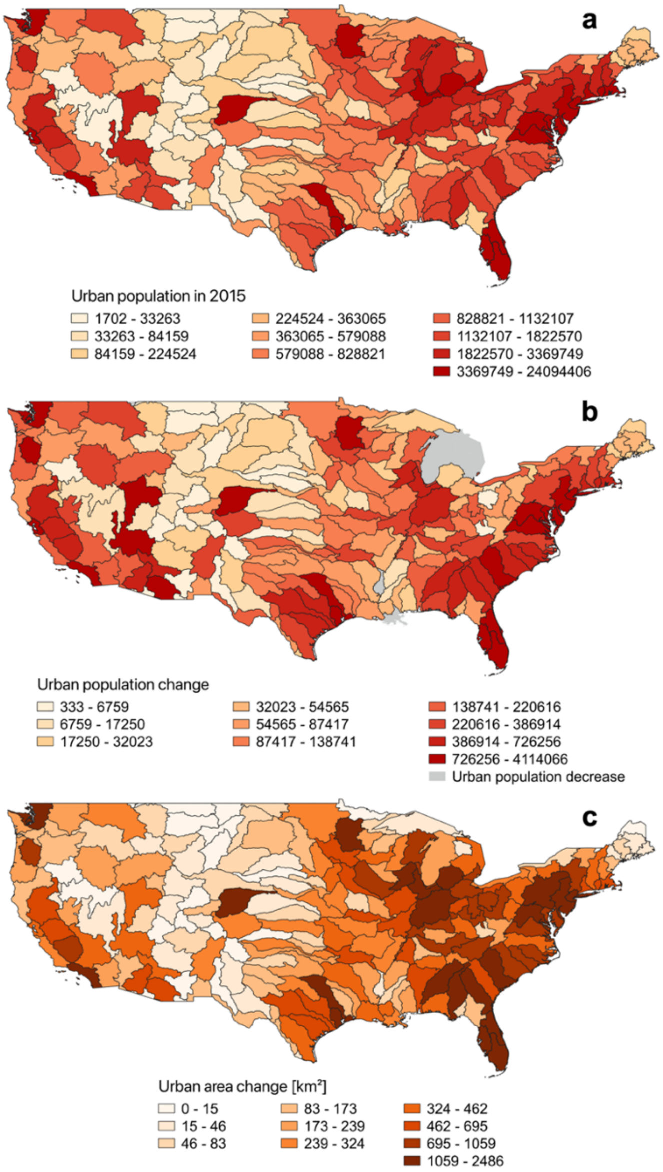
a
Urban population in 2015
1702 - 33263
33263 - 84159
84159 - 224524
224524 - 363065
363065 - 579088
579088 - 828821
828821 - 1132107
1132107 - 1822570
1822570 - 3369749
3369749 - 24094406
b
Urban population change
333 - 6759
6759 - 17250
17250 - 32023
32023 - 54565
54565 - 87417
87417 - 138741
138741 - 220616
220616 - 386914
386914 - 726256
726256 - 4114066
Urban population decrease
c
Urban area change [km²]
0 - 15
15 - 46
46 - 83
83 - 173
173 - 239
239 - 324
324 - 462
462 - 695
695 - 1059
1059 - 2486

Figure 5.8 Spatial distribution of urban attributes within river basins of the CONUS. **a.** Total urban population in 2015. **b.** Urban population change between 1990 and 2015. River basins that experienced a decrease in the number of inhabitants are highlighted in light grey and the reduction of their urban population change ranges from -225842 and -253. **c.** Urban area change between 1990 and 2014.

The general spatial distribution of urban population in 2015, urban population change, and urban area change at the river basin scale (Figure 5.8) is in agreement with the spatial trend observed for the model parameters α_b and β_b at the river basin level (Figure 5.6a and Figure 5.6c), with higher urban population in 2015, urban population change, and urban area change along the East and West Coast. Indeed, when urban population in 2015, the urban population change and urban area change values are represented against α_b and β_b parameters (Figure 5.9), a mild correlation is found between these variables, with the highest coefficient of determination R^2 associated to the total urban population of 2015 and urban area change.

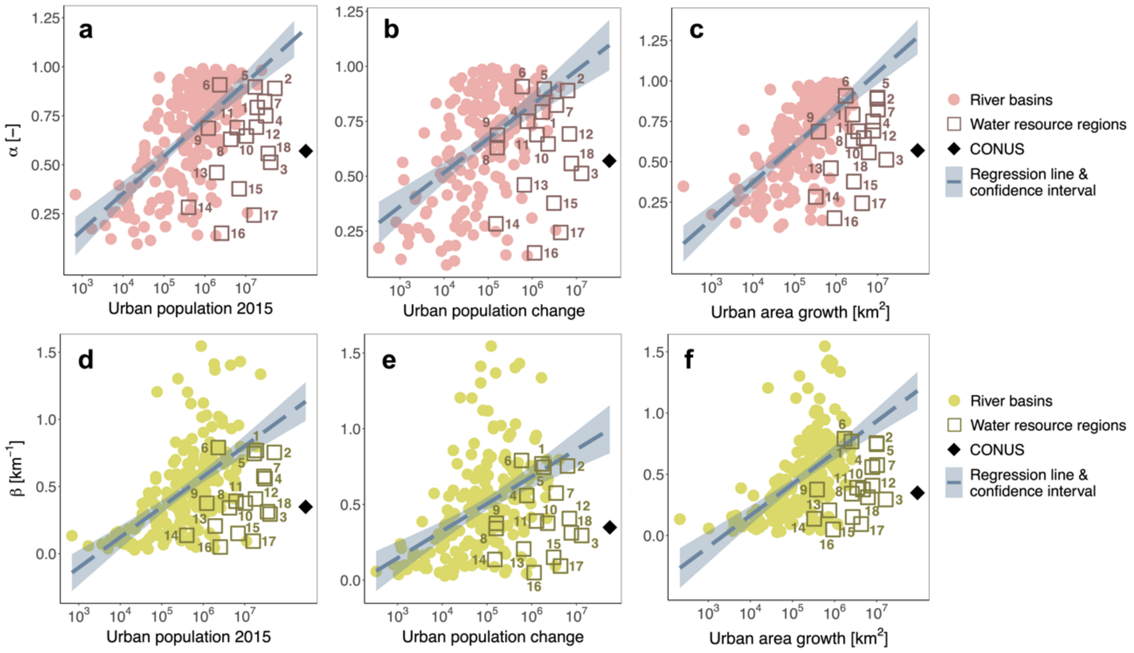

Figure 5.9 Correlation between urban attributes and α_x and β_x parameters of the distance-decay model for the three levels of spatial aggregation (river basins, water resource regions, and the CONUS). Circles show pairs of urban attributes and α_x and β_x parameters obtained for the 191 river basins, squares are used to represent the 18 water resource regions, while the black diamond identifies the same values calculated for the CONUS. **a.** Correlation between total urban population in 2015 and α_x. The linear regression between total urban population and α_b parameter at the river basin level is depicted by the grey dashed line ($\alpha_b = -0.40 + 0.08\, pop_{2015,b}$) and its coefficient of determination R^2 is 0.38. **b.** Correlation between urban population change and α_x. The linear regression between urban population change and α_b parameter at the river basin level is depicted by the grey dashed line ($\alpha_b = -0.10 + 0.07\, \Delta pop_b$) and its coefficient of determination R^2 is 0.25. **c.** Correlation between urban area change and α_x. The linear regression between urban area change and α_b parameter at the river basin level is depicted by the grey dashed line ($\alpha_b = -0.53 + 0.10\, \Delta urb_b$) and its coefficient of determination R^2 is 0.42. **d.** The same as panel a, but for the decay rate β_x. The equation of the linear regression is: $\beta_b = -4.64 + 0.28\, pop_{2015,b}$ with $R^2 = 0.37$. **e.** The same as panel b, but for the decay rate β_x. The equation of the linear regression is: $\beta_b = -3.62 + 0.23\, \Delta pop_b$ with $R^2 = 0.24$. **f.** The same as panel c, but for the decay rate β_x. The equation of the linear regression is: $\beta_b = -4.97 + 0.33\, \Delta urb_b$ with $R^2 = 0.39$.

Finally, the maximum extent of urban agglomerations in each river basin of the CONUS was analyzed to inspect whether river basins having larger urban clusters experienced a more pronounced loss in surface water close to their urban areas. An evident influence of the maximum extent of urban clusters did not emerge from such analysis (Figure 5.10). However, as the variability (i.e., the interquartile range) and the 75th percentile of the extent of urban agglomerations increase, the decay rate β_b increases as well (Figure 5.11), highlighting the presence of a steeper decay in surface water loss moving away from urban areas in river basins having larger urban agglomerations.

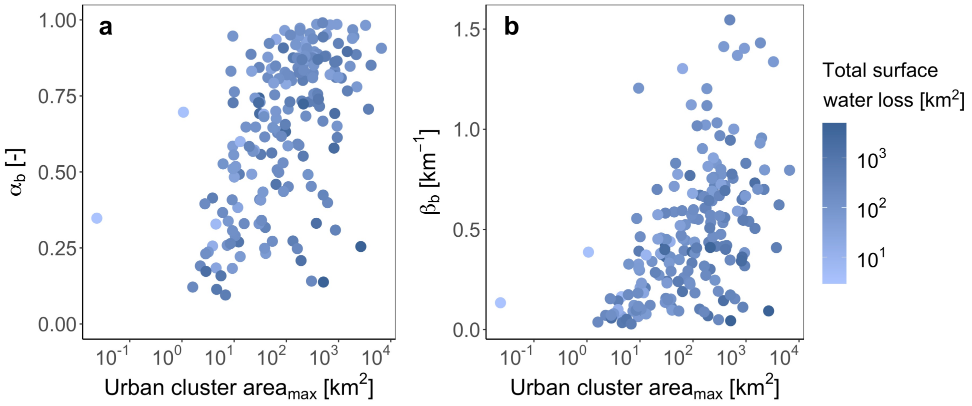

Figure 5.10 Correlation between the extent of the largest urban clusters and α_b and β_b parameters for the 191 river basins of the CONUS where the distance-decay model was applied using a 3 km wide distance bin. Points are colored based on the total extent of surface water loss observed in each river basin. **a.** Correlation between the extent of the largest urban clusters and α_b (coefficient of determination $R^2 = 0.30$). **b.** Correlation between the extent of the largest urban clusters and β_b (coefficient of determination $R^2 = 0.26$).

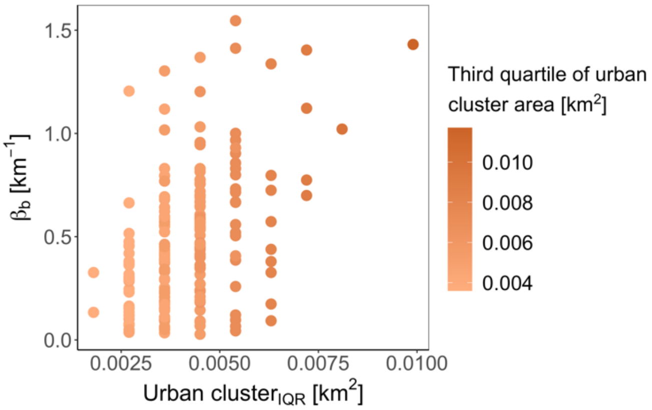

Figure 5.11 Correlation between the interquartile range of the extent of urban clusters and β_b parameter for the 191 river basins of the CONUS where the distance-decay model was applied using a 3 km wide distance bin (coefficient of determination $R^2 = 0.14$). Points are colored based on the third quartile value of the urban agglomeration areas in each river basin.

5.3.3 Overall surface water extent *versus* surface water loss: comparison of distance decay patterns

The overall implication inferred from the analysis of the observed frequency of surface water loss occurrence and from the application of the distance-decay model was verified by comparing the distance-decay of surface water loss and distance-decay associated to the overall extent of surface water with respect to distance from urban areas to check whether surface water loss is occurring close to human settlements rather than far away from them. The spatial distribution of the overall extent of surface water first proves that also the occurrence of surface water bodies is more frequent close to urban areas and exponentially declines with increasing distance, confirming what has been generally recognized about the proximity of human settlements to water sources. More importantly, in all the aforementioned 191 river basins where the distance-decay model was applied using a 3 km wide distance bin, the spatial decline of the frequency of surface water loss is steeper than the decline observed for the overall extent of surface water. In particular, Figure 5.12 depicts the spatial distribution of the difference between the two parameters. This difference is always positive, revealing that the decay rate of surface water loss (β_b) is consistently larger than the decay rate of the overall extent of surface water (β_b^{sw}).

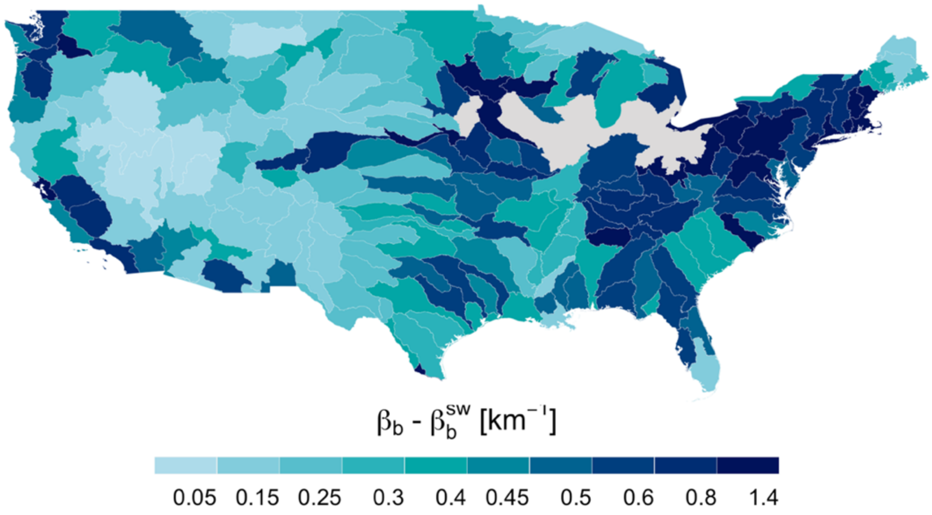

Figure 5.12 Spatial distribution of the difference between the decay rate associated to the distance-decay of surface water loss (β_b) and the overall extent of surface water (β_b^{sw}) across 191 river basins of the CONUS where the distance-decay model was applied using a 3 km wide distance bin. River basins that are not fitted by the model using a 3 km wide distance bin are indicated in light grey.

Figure 5.13 instead shows the variability of the two parameters and also in this case the decay rate of surface water loss (β_b) presents higher values than the decay rate of the overall extent of surface water (β_b^{sw}). These results clearly demonstrate that more surface water loss is occurring close to urban areas rather than far from them in all the rivers basins of the CONUS. The same outcome is also confirmed when the comparison between the decay rates is performed at the climatic region level (see Subsection 5.3.4 of this Chapter and Figure 5.15).

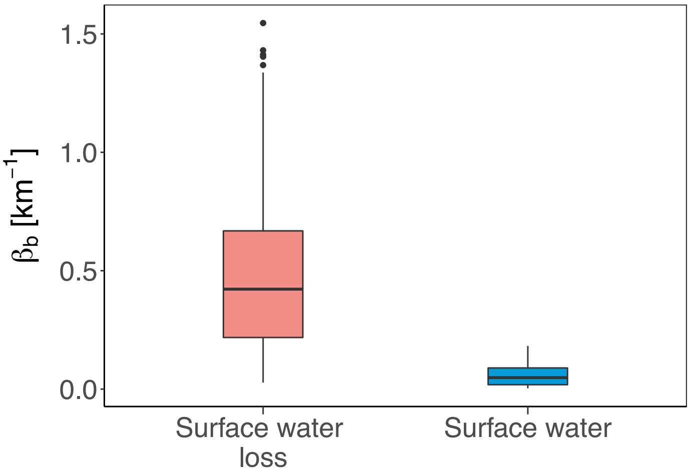

Figure 5.13 Variability of the decay rate at the river basin level associated to the distance-decay of surface water loss (β_b) and the overall extent of surface water (β_b^{sw}).

5.3.4 Influence of climate

To investigate the role played by climate, the spatial distribution of surface water loss locations and the associated variability of the model parameters α_b and β_b were evaluated over the main Köppen-Geiger climatic zones, i.e., tropical, arid, temperate, continental, and polar (Beck et al., 2018). More than one third of the surface water loss locations (37.13%) are located in the temperate region, with the remaining falling in the arid (29.37%), continental (27.5%), and tropical (5.99%) regions. Less than 0.01% of surface water loss occurs within the polar zone, which from now on is not considered for further analysis. Afterwards, the variability of model parameters α_b and β_b was analyzed in the climatic zones where locations of surface water loss are found, and their weighted average associated to each climatic zone was estimated (Figure 5.14), as described in Subsection 5.2.4 of this Chapter.

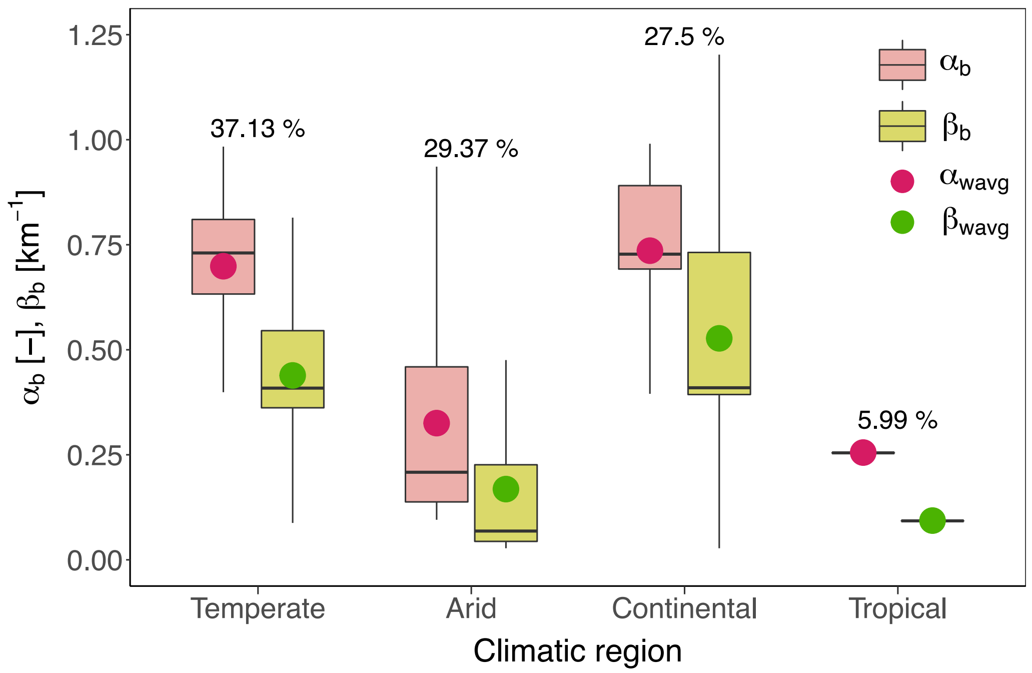

Figure 5.14 Variability of α_b and β_b parameters of the distance-decay model applied at the river basin level across the main climatic regions of the CONUS. The boxplot edges indicate the first and third quartiles, with the thick horizontal line representing the median value. Colored circles illustrate the weighted average of the parameters associated to each climatic region. The percentage of surface water loss locations falling in each climatic region is also indicated.

The highest values of α_b and β_b parameters are found in the temperate and continental climatic regions. In the continental region, the weighted average of α_b is equal to 0.736 (1st, 2nd, 3rd quartiles equal to 0.692, 0.728, and 0.891, respectively), while the weighted average of β_b is equal to 0.527 (1st, 2nd, 3rd quartiles equal to 0.393, 0.410, and 0.732, respectively). The temperate region shows slightly smaller values, with the weighted average of α_b equal to 0.699 (1st, 2nd, 3rd quartiles equal to 0.633, 0.730, and 0.810, respectively), and the weighted average of β_b equal to 0.439 (1st, 2nd, 3rd quartiles equal to 0.362, 0.409, and 0.545, respectively). Across these two climatic zones, characterized by abundant water resources, surface water loss is concentrated close to urban areas (i.e., the majority of surface water loss is located within a 3 km distance) and its frequency of occurrence is rapidly decreasing in space. Therefore, localized and concentrated impacts of urban areas on surface water loss are typical of temperate and continental climatic regions, as also shown in Figure 5.5a, where the theoretical and observed average distances of surface water loss occurrence present generally smaller values for river basins characterized by a temperate and continental climate compared to those with an arid and tropical climate.

The arid region presents significantly smaller values of α_b and β_b parameters. In particular, the weighted average of α_b is equal to 0.325 (1st, 2nd, 3rd quartiles equal to 0.138, 0.208, and 0.459, respectively), while the weighted average of β_b is equal to 0.168 (1st, 2nd, 3rd quartiles equal to 0.044, 0.068, and 0.226, respectively). Across the arid region, characterized by a limited availability of surface water resources, surface water loss is more uniformly distributed across all distance classes, with only a 16% of surface water loss within a 3 km distance from urban areas on average. Indeed, the frequency of occurrence of surface water loss in space shows a decreasing trend, although dampened when compared to temperate and continental regions. Therefore, arid climates are characterized by more distributed impacts of urban areas on surface water loss, which typically affect larger areas around cities (see also Figure 5.5a). The tropical region shows the lowest average values of α_b (0.255) and β_b (0.093 km^{-1}). However, surface water loss locations associated to this climatic region belong to one river basin only, thus limiting its representativeness.

Finally, from the evaluation of the distribution of the overall surface water extent across the main climatic regions of the CONUS emerged that the fraction of total surface water extent locations that lies on the continental, temperate, arid, tropical, and polar climatic regions is 67.30%, 20.36%, 10.95%, 1.36%, and 0.03%, respectively. Moreover, the decay rate of the overall extent of surface water (β_b^{sw}) was assessed across the Köppen-Geiger climatic regions to carry out a comparison with the distribution found for the decay rate of surface water loss (β_b). The values of the decay rate of the overall surface water extent are always smaller than those of the surface water loss across each climatic zone (Figure 5.15). This result further confirms that more surface water loss is occurring close to urban areas, rather than far away from them, within the river basins of the CONUS.

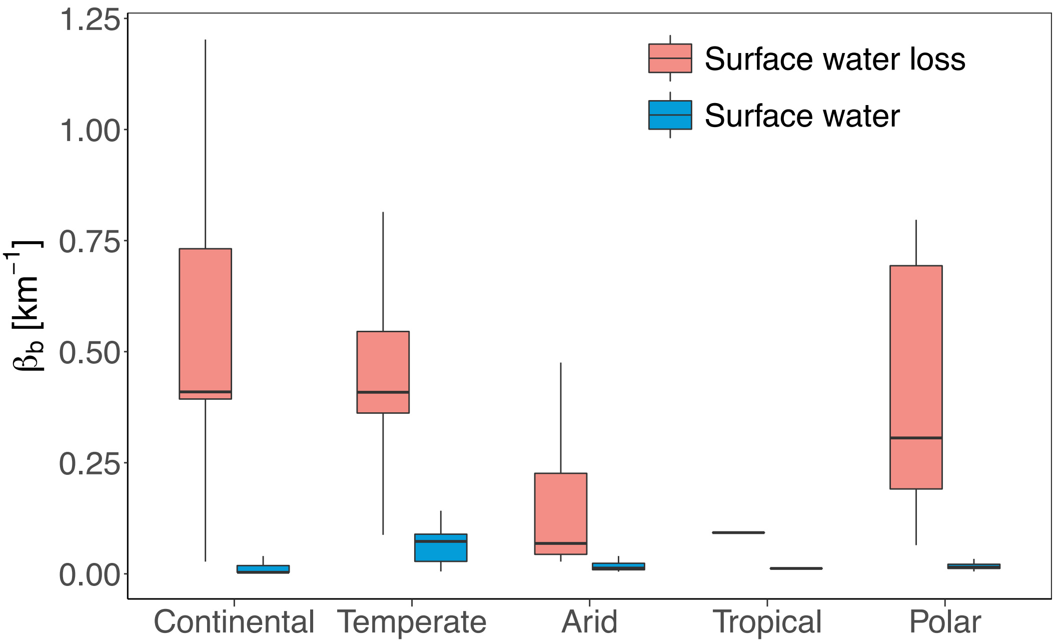

Figure 5.15 Variability of the decay rate at the river basin level associated to the distance-decay of surface water loss (β_b) and to the overall extent of surface water (β_b^{sw}) across the main climatic regions of the CONUS.

6 Conclusions

Water is a finite resource highly vulnerable to human behavior and climate. The increasing water demand induced by population growth and socio-economic development will progressively reduce freshwater and enhance the global competition for it (Padowski & Gorelick, 2014; Boretti & Rosa, 2019; Erler et al., 2019). In addition, water stress is amplified by climate change impacts, mostly by variations of precipitation and temperature and extreme events like droughts and heatwaves (Wanders et al., 2015). The depletion of surface water affects not only human activities, but also many ecosystems whose preservation heavily relies on these resources (Sun & Caldwell, 2015; Liyanage & Yamada, 2017; Aznar-Sánchez et al., 2019). Hence, new sustainable strategies are needed to increase water use efficiency, diminish water demand, and guarantee water conservation (Cosgrove & Loucks, 2015; Mekonnen & Hoekstra, 2016).

The United States are among the countries of the World that have already witnessed the effects of population growth and climate change on water supply (Wada & Bierkens, 2014). Although over the past years water use in the US has adapted to water supplies avoiding the occurrence of water shortages, in the future water availability is expected to be substantially reduced by demographic expansion, decreasing precipitation, and rising temperature, while water demand will continue to increase, posing new serious challenges for water management and sustainable development (Brown et al., 2019a). Within this context, surface waters in the US are extremely endangered, since they represent the national main source of freshwater withdrawals (Dieter et al., 2018).

Moreover, given that the main drivers of the global increase of water demand are projected to be urbanization and economic development, it is necessary to further analyze the influence of urbanization on surface water depletion (Wada et al., 2017). Indeed, urban areas are responsible for the emergence of local hotspots of surface water loss that cannot be explained by climate change alone, and this suggests the need to examine the spatial interaction between human settlements and surface water losses (Fitzhugh & Richter, 2004; Hoekstra et al., 2018).

Learning from data observations and defining analytical models that successfully reproduce the observed patterns is key to sustainable water policy strategies. In this context, RO1 of this Thesis explored the interlink between the variation in surface water extent and the change in anthropogenic and climatic variables that occurred in the contiguous United States (CONUS) in the period 1984-2020. Since population growth was found to be the dominant driver, especially across arid climates, RO2 aimed at explaining the dynamics of interaction between surface water depletion and human settlements by evaluating the spatial distribution of surface water losses that took place between 1984 and 2018.

6.1 Achievements

In order to identify the most influencing factors of the change in surface water extent, gains and losses of surface water that occurred in the period 2000-2020 (second epoch) with respect to the amount of surface water found in the period 1984-1999 (first epoch) were measured across the river basins of the CONUS and their difference was then computed to obtain the net variation of surface water extent. A net gain is found when the total gain exceeds the total loss of surface water, whereas a net loss is found when the total gain is less than the total loss of surface water. Afterwards, this variation was compared to changes that took place between the same epochs in three anthropogenic (urban area, population, and irrigated land) and two climatic (precipitation and temperature) factors, that are here considered to be potential drivers of surface water gain and loss. The surface water loss and anthropogenic drivers were estimated using remotely sensed data, while the climatic drivers were derived from observation-based estimates. All data variations were aggregated at the river basin level. Since urban areas expanded across the whole CONUS and temperature turned out to be increasing in almost all the river basins of the CONUS (199 river basins, covering 96.68% of the CONUS area), these factors were not considered in the subsequent analysis for the definition of the predominant anthropogenic and climatic contributors to the increase and decrease of surface water extent. The remaining three drivers were assumed to potentially contribute to an increase (decrease) in surface water extent if a decreasing (increasing) pattern was observed for population and irrigated land, and an increasing (decreasing) trend characterized precipitation. Then, the overlap of contributors across river basins of the CONUS was assessed.

A general increase in surface water extent was found in the majority of the river basins of the CONUS, with some exceptions in the southwestern and northeastern regions, which are characterized by a net surface water loss. The net gain of surface water resulted to be mainly produced by an increase in precipitation over the eastern area of the US and a decrease in irrigated land along the West Coast. Conversely, the net loss of surface water mostly corresponds to an increase of population, with the additional contribution of precipitation decrease in the river basins of the southwestern region and an expansion of irrigated land in the river basins of the northeastern region. The same correspondence was also confirmed at the level of the climatic zones of the CONUS, as in all the climatic regions/subtypes experiencing a net loss of surface water, i.e., the arid region and the majority of its subtypes as well as in the "cold, dry & hot summer" subtype of the continental region, population turned out to be the dominant driver along with precipitation decrease.

The findings of this first analysis proved that population growth is the major driver of surface water loss, hence an additional investigation of the influence of built-up areas on surface water depletion was carried out. It is generally known that urban areas access surface water sources located in the surrounding of cities to meet their water demand. As local surface waters are exhausted, cities need to withdraw water from sources located farther away. The consequent progressive depletion of local surface waters in the proximity of human settlements highlights the importance of getting a more comprehensive understanding of the spatial interaction between urban areas and locations that experienced a loss of surface water. This is the reason why RO2 examines and models the spatial distribution of surface water losses that occurred between 1984 and 2018 within the CONUS as a function of distance from urban areas. Also in this case, data of built-up area and surface water loss were extracted from datasets obtained from EO sensors. The frequency of occurrence of surface water loss represented as a function of distance from urban areas revealed that surface water loss is more frequent close to human settlements and exponentially declines as the distance from urban areas increases at the river basin, water resource region, and CONUS levels. Therefore, a distance-decay model was developed with a truncated exponential probability distribution, defining a theoretical characterization and a statistically significant modeling of the observed declining trend. The adopted distance-decay model demonstrates that urban areas produce an exponentially increasing stress on surface water resources in the proximity of cities. The presence of a steeper distance-decay trend of surface water loss compared to the distance-decay obtained for the overall extent of surface water confirms once again that more surface water loss in the CONUS occurred adjacent to urban areas. The reliability of the distance-decay model was established through the comparison between the observed distance from urban areas at which on average surface water losses occurred and the corresponding theoretical distance derived from the exponential function of the model. The statistically significant correlation between observed and theoretical values of the average distance of occurrence of surface water loss demonstrates the consistency of the model in reproducing the spatial distribution of locations of surface water loss. Moreover, it was also noticed that surface water losses decline faster in river basins with larger urban agglomerations, highlighting that the influence of human settlements increases with the extent of urban clusters. Finally, distinct patterns in the distance-decay of surface water loss were found across the main climatic zones of the CONUS. In particular, localized and concentrated impacts of urban areas on surface water loss resulted to be typical of the temperate and continental climatic regions, whereas areas with arid climates were found to be characterized by more widespread impacts distributed over larger distances from cities. The model here developed and applied over the study area of the CONUS looks promising as it represents a valuable analytical tool that describes the observed spatial distribution of surface water loss locations with respect to urban areas and supplies useful indications about the interaction that can potentially be found in other study areas with similar social and climatic conditions.

In conclusion, the overall methodology adopted to achieve both ROs of this Thesis provides baseline information for the definition of sustainable management practices that guarantee a balance between urban population growth, urban water demand, and water needs for the environment.

6.2 Constraints

Despite these major achievements, the following limitations need to be acknowledged. In the study related to RO1, water availability is intended as the extent of surface water that is physically available, neglecting its volume and other equally critical aspects, such as water quality and water delivery, which can impact both humans and the environment. Moreover, groundwater resources are not included in this analysis, although they represent another important source for human activities and natural ecosystems. Notwithstanding the level of accuracy of data related to population and urbanization processes, the information about irrigation practices is not as much exhaustive and more specific data about irrigated agriculture would be useful to understand where and when this driver produces high water stress. Finally, the results from RO2 might be limited by the assumption of the ideal condition that only the geographic distance, estimated in terms of Euclidean distance, controls the spatial interaction between urban areas and surface water resources, disregarding the influence of other factors of interaction, such as infrastructures, industries, power generation plants, and pipeline networks.

6.3 Recommendations

The extension of the proposed research objectives to new study areas and at the global scale would allow to explore how the availability of surface water resources is affected by the simultaneous influence of anthropogenic and climatic factors in other regions of the world having socio-economic, hydrologic, morphologic, and climatic conditions that are different from those found within the CONUS. The outcomes obtained from the analysis of the drivers of surface water change suggest that in the future it might be beneficial to focus this investigation on local areas where surface water resources are more vulnerable to human dynamics and climate variability. For instance, particular attention should be paid to the southwestern US, which is exceedingly sensitive to changes in temperature and thus vulnerable to drought, since even a small decrease in water availability in this already arid region can stress natural systems and further threaten water supplies (Dieter et al., 2018). Other example of US regions that require additional analysis are the California Central Valley and the Mississippi Floodplain where a decrease in the use of water for irrigation practices has been observed in the period 2000-2020, and the zone of the High Plain Aquifer where instead water use in irrigation has first increased and then decreased over the same period (Zhang & Long, 2021). From a methodological viewpoint, it would be useful to conduct further investigations for the attribution of surface water availability changes to anthropogenic and climatic drivers through a cross-validation procedure, such as machine-learning algorithms. The definition of predictive models would allow the simulation of future availability of surface water resources under specific scenarios of socio-economic conditions and climate change.

Moreover, given that the distance-decay model yielded an excellent description of the spatial interaction between human settlements and surface water depletion in the CONUS, it would be interesting to apply this approach to other study areas to verify its reliability. To increase the level of detail of the distance-decay model and to recognize the specific role played by features and practices that impact surface water availability, such as dams and groundwater withdrawals, future work might also inspect the relation between surface water loss locations and the geographical position of reservoirs and well fields. This additional information may be useful to support the identification of the optimal location for water withdrawals, but a careful assessment will be needed to reach a balance between model complexity and uncertainty. Finally, future investigations should consider the effects due to the transfer of industrial activities from urban areas to peri-urban and suburban areas that occurred during the last decades which is expected to further increase urban population with respect to population of rural areas.

References

Acharya, T., Lee, D., Yang, I. & Lee, J. (2016) "Identification of Water Bodies in a Landsat 8 OLI Image Using a J48 Decision Tree," *Sensors*, 16(7), p. 1075. doi:10.3390/s16071075.

Afaq, Y. & Manocha, A. (2021) "Analysis on change detection techniques for remote sensing applications: A review," *Ecological Informatics*, 63, p. 101310. doi:10.1016/j.ecoinf.2021.101310.

Ambika, A.K., Wardlow, B. & Mishra, V. (2016) "Remotely sensed high resolution irrigated area mapping in India for 2000 to 2015," *Scientific Data*, 3(1), p. 160118. doi:10.1038/sdata.2016.118.

Anderson, R.G., Lo, M.-H. & Famiglietti, J.S. (2012) "Assessing surface water consumption using remotely-sensed groundwater, evapotranspiration, and precipitation," *Geophysical Research Letters*, 39(16), p. n/a-n/a. doi:10.1029/2012GL052400.

Artell, J., Ahtiainen, H. & Pouta, E. (2019) "Distance decay and regional statistics in international benefit transfer," *Ecological Economics*, 164, p. 106383. doi:10.1016/j.ecolecon.2019.106383.

Asokan, A. & Anitha, J. (2019) "Change detection techniques for remote sensing applications: a survey," *Earth Science Informatics*, 12(2), pp. 143–160. doi:10.1007/s12145-019-00380-5.

Averyt, K., Meldrum, J., Caldwell, P., Sun, G., McNulty, S., Huber-Lee, A. & Madden, N. (2013) "Sectoral contributions to surface water stress in the coterminous United States," *Environmental Research Letters*, 8(3), p. 035046. doi:10.1088/1748-9326/8/3/035046.

Aznar-Sánchez, J.A., Velasco-Muñoz, J.F., Belmonte-Ureña, L.J. & Manzano-Agugliaro, F. (2019) "The worldwide research trends on water ecosystem services," *Ecological Indicators*, 99, pp. 310–323. doi:10.1016/j.ecolind.2018.12.045.

Baldocchi, D., Dralle, D., Jiang, C. & Ryu, Y. (2019) "How Much Water Is Evaporated Across California? A Multiyear Assessment Using a Biophysical Model Forced With Satellite Remote Sensing Data," *Water Resources Research*, 55(4), pp. 2722–2741. doi:https://doi.org/10.1029/2018WR023884.

Balling, R.C. & Goodrich, G.B. (2011) "Spatial analysis of variations in precipitation intensity in the USA," *Theoretical and Applied Climatology*, 104(3–4), pp. 415–421. doi:10.1007/s00704-010-0353-0.

Bartels, R.J., Black, A.W. & Keim, B.D. (2020) "Trends in precipitation days in the United States," *International Journal of Climatology*, 40(2), pp. 1038–1048. doi:10.1002/joc.6254.

Bastiaanssen, W.G.., Molden, D.J. & Makin, I.W. (2000) "Remote sensing for irrigated agriculture: examples from research and possible applications," *Agricultural Water Management*, 46(2), pp. 137–155. doi:10.1016/S0378-3774(00)00080-9.

Bazzi, H., Baghdadi, N., Ienco, D., El Hajj, M., Zribi, M., Belhouchette, H., Escorihuela, M.J.

& Demarez, V. (2019) “Mapping Irrigated Areas Using Sentinel-1 Time Series in Catalonia, Spain,” *Remote Sensing*, 11(15), p. 1836. doi:10.3390/rs11151836.

Beck, H.E., Zimmermann, N.E., McVicar, T.R., Vergopolan, N., Berg, A. & Wood, E.F. (2018) “Present and future Köppen-Geiger climate classification maps at 1-km resolution,” *Scientific Data*, 5(1), p. 180214. doi:10.1038/sdata.2018.214.

Bekele, A.A., Pingale, S.M., Hatiye, S.D. & Tilahun, A.K. (2019) “Impact of climate change on surface water availability and crop water demand for the sub-watershed of Abbay Basin, Ethiopia,” *Sustainable Water Resources Management*, 5(4), pp. 1859–1875. doi:10.1007/s40899-019-00339-w.

Bernhofen, M. V., Trigg, M.A., Sleigh, P.A., Sampson, C.C. & Smith, A.M. (2021) “Global flood exposure from different sized rivers,” *Natural Hazards and Earth System Sciences*, 21(9), pp. 2829–2847. doi:10.5194/nhess-21-2829-2021.

Bhaskar, A.S., Hopkins, K.G., Smith, B.K., Stephens, T.A. & Miller, A.J. (2020) “Hydrologic Signals and Surprises in U.S. Streamflow Records During Urbanization,” *Water Resources Research*, 56(9). doi:10.1029/2019WR027039.

Bierkens, M.F.P. (2015) “Global hydrology 2015: State, trends, and directions,” *Water Resources Research*, 51(7), pp. 4923–4947. doi:10.1002/2015WR017173.

Bigelow, D.P., Plantinga, A.J., Lewis, D.J. & Langpap, C. (2017) “How Does Urbanization Affect Water Withdrawals? Insights from an Econometric-Based Landscape Simulation,” *Land Economics* , 93(3), pp. 413–436. doi:10.3368/le.93.3.413.

Boretti, A. & Rosa, L. (2019) “Reassessing the projections of the World Water Development Report,” *npj Clean Water*, 2(1), p. 15. doi:10.1038/s41545-019-0039-9.

Botter, G. & Durighetto, N. (2020) “The Stream Length Duration Curve: A Tool for Characterizing the Time Variability of the Flowing Stream Length,” *Water Resources Research*, 56(8), p. e2020WR027282. doi:https://doi.org/10.1029/2020WR027282.

Bounoua, L., Nigro, J., Zhang, P., Thome, K. & Lachir, A. (2018) “Mapping urbanization in the United States from 2001 to 2011,” *Applied Geography*, 90, pp. 123–133. doi:10.1016/j.apgeog.2017.12.002.

Brown, T.C., Mahat, V. & Ramirez, J.A. (2019a) “Adaptation to Future Water Shortages in the United States Caused by Population Growth and Climate Change,” *Earth’s Future*, 7(3), pp. 219–234. doi:10.1029/2018EF001091.

Brown, V.M., Keim, B.D. & Black, A.W. (2019b) “Climatology and Trends in Hourly Precipitation for the Southeast United States,” *Journal of Hydrometeorology*, 20(8), pp. 1737–1755. doi:10.1175/JHM-D-19-0004.1.

Brunner, M.I., Swain, D.L., Gilleland, E. & Wood, A.W. (2021) “Increasing importance of temperature as a contributor to the spatial extent of streamflow drought,” *Environmental Research Letters*, 16(2), p. 024038. doi:10.1088/1748-9326/abd2f0.

Cai, G., Ren, H., Yang, L., Zhang, N., Du, M. & Wu, C. (2019) "Detailed Urban Land Use Land Cover Classification at the Metropolitan Scale Using a Three-Layer Classification Scheme," *Sensors*, 19(14), p. 3120. doi:10.3390/s19143120.

CCSP (2008) *The Effects of Climate Change on Agriculture, Land Resources, Water Resources, and Biodiversity*. Washington, DC., USA. Available at: https://www.fs.fed.us/rm/pubs_other/rmrs_2008_backlund_p003.pdf.

Ceola, S., Hödl, I., Adlboller, M., Singer, G., Bertuzzo, E., Mari, L., Botter, G., Waringer, J., Battin, T.J. & Rinaldo, A. (2013) "Hydrologic Variability Affects Invertebrate Grazing on Phototrophic Biofilms in Stream Microcosms," *PLoS ONE*. Edited by M.R. Liles, 8(4), p. e60629. doi:10.1371/journal.pone.0060629.

Ceola, S., Laio, F. & Montanari, A. (2014) "Satellite nighttime lights reveal increasing human exposure to floods worldwide," *Geophysical Research Letters*, 41(20), pp. 7184–7190. doi:https://doi.org/10.1002/2014GL061859.

Ceola, S., Laio, F. & Montanari, A. (2015) "Human-impacted waters: New perspectives from global high-resolution monitoring," *Water Resources Research*, 51(9), pp. 7064–7079. doi:10.1002/2015WR017482.

Ceola, S., Laio, F. & Montanari, A. (2019) "Global-scale human pressure evolution imprints on sustainability of river systems," *Hydrology and Earth System Sciences*, 23(9), pp. 3933–3944. doi:10.5194/hess-23-3933-2019.

Chen, M., Nabih, S., Brauer, N.S., Gao, S., Gourley, J.J., Hong, Z., Kolar, R.L. & Hong, Y. (2020) "Can Remote Sensing Technologies Capture the Extreme Precipitation Event and Its Cascading Hydrological Response? A Case Study of Hurricane Harvey Using EF5 Modeling Framework," *Remote Sensing*, 12(3), p. 445. doi:10.3390/rs12030445.

Chen, Y. (2015) "The distance-decay function of geographical gravity model: Power law or exponential law?," *Chaos, Solitons & Fractals*, 77, pp. 174–189. doi:https://doi.org/10.1016/j.chaos.2015.05.022.

Chen, Y. & Huang, L. (2018) "A scaling approach to evaluating the distance exponent of the urban gravity model," *Chaos, Solitons & Fractals*, 109, pp. 303–313. doi:https://doi.org/10.1016/j.chaos.2018.02.037.

Chen, Y., Lv, Z., Huang, B. & Jia, Y. (2018) "Delineation of Built-Up Areas from Very High-Resolution Satellite Imagery Using Multi-Scale Textures and Spatial Dependence," *Remote Sensing*, 10(10), p. 1596. doi:10.3390/rs10101596.

Coleman, R.W., Stavros, N., Hulley, G. & Parazoo, N. (2020) "Comparison of Thermal Infrared-Derived Maps of Irrigated and Non-Irrigated Vegetation in Urban and Non-Urban Areas of Southern California," *Remote Sensing*, 12(24), p. 4102. doi:10.3390/rs12244102.

Collados-Lara, A.-J., Fassnacht, S.R., Pardo-Igúzquiza, E. & Pulido-Velazquez, D. (2020) "Assessment of High Resolution Air Temperature Fields at Rocky Mountain National Park by

Combining Scarce Point Measurements with Elevation and Remote Sensing Data," *Remote Sensing*, 13(1), p. 113. doi:10.3390/rs13010113.

Cooley, S.W., Ryan, J.C. & Smith, L.C. (2021) "Human alteration of global surface water storage variability," *Nature*, 591(7848), pp. 78–81. doi:10.1038/s41586-021-03262-3.

Corbane, C., Pesaresi, M., Kemper, T., Politis, P., Florczyk, A.J., Syrris, V., Melchiorri, M., Sabo, F. & Soille, P. (2019) "Automated global delineation of human settlements from 40 years of Landsat satellite data archives," *Big Earth Data*, 3(2), pp. 140–169. doi:10.1080/20964471.2019.1625528.

Cosgrove, W.J. & Loucks, D.P. (2015) "Water management: Current and future challenges and research directions," *Water Resources Research*, 51(6), pp. 4823–4839. doi:10.1002/2014WR016869.

CRED (2020) *Natural Disasters 2019*. Brussels. Available at: https://emdat.be/%0Dsites/default/files/adsr_2019.pdf.

Daher, B., Lee, S.-H., Kaushik, V., Blake, J., Askariyeh, M.H., Shafiezadeh, H., Zamaripa, S. & Mohtar, R.H. (2019) "Towards bridging the water gap in Texas: A water-energy-food nexus approach," *Science of The Total Environment*, 647, pp. 449–463. doi:https://doi.org/10.1016/j.scitotenv.2018.07.398.

Dang, Q., Lin, X. & Konar, M. (2015) "Agricultural virtual water flows within the United States," *Water Resources Research*, 51(2), pp. 973–986. doi:10.1002/2014WR015919.

Daniell, K.A., Rinaudo, J.-D., Chan, N.W.W., Nauges, C. & Grafton, Q. (2015) "Understanding and Managing Urban Water in Transition," in, pp. 1–30. doi:10.1007/978-94-017-9801-3_1.

Dari, J., Quintana-Seguí, P., Escorihuela, M.J., Stefan, V., Brocca, L. & Morbidelli, R. (2021) "Detecting and mapping irrigated areas in a Mediterranean environment by using remote sensing soil moisture and a land surface model," *Journal of Hydrology*, 596, p. 126129. doi:10.1016/j.jhydrol.2021.126129.

Delpla, I., Jung, A.-V., Baures, E., Clement, M. & Thomas, O. (2009) "Impacts of climate change on surface water quality in relation to drinking water production," *Environment International*, 35(8), pp. 1225–1233. doi:https://doi.org/10.1016/j.envint.2009.07.001.

Demarez, V., Helen, F., Marais-Sicre, C. & Baup, F. (2019) "In-Season Mapping of Irrigated Crops Using Landsat 8 and Sentinel-1 Time Series," *Remote Sensing*, 11(2), p. 118. doi:10.3390/rs11020118.

Dettinger, M., Udall, B. & Georgakakos, A. (2015) "Western water and climate change," *Ecological Applications*, 25(8), pp. 2069–2093. doi:10.1890/15-0938.1.

Di Baldassarre, G., Mazzoleni, M. & Rusca, M. (2021) "The legacy of large dams in the United States," *Ambio*, 50(10), pp. 1798–1808. doi:10.1007/s13280-021-01533-x.

Dieter, C.A., Maupin, M.A., Caldwell, R.R., Harris, M.A., Ivahnenko, T.I., Lovelace, J.K., Barber, N.L. & Linsey, K.S. (2018) *Estimated use of water in the United States in 2015*, *Circular*. Reston, VA. doi:10.3133/cir1441.

Donchyts, G., Schellekens, J., Winsemius, H., Eisemann, E. & van de Giesen, N. (2016) "A 30 m Resolution Surface Water Mask Including Estimation of Positional and Thematic Differences Using Landsat 8, SRTM and OpenStreetMap: A Case Study in the Murray-Darling Basin, Australia," *Remote Sensing*, 8(5), p. 386. doi:10.3390/rs8050386.

Dooge, J.C.I. (2009) *Fresh Surface Water*, *Encyclopedia of Life Support Systems*. Available at: https://www.epa.gov/report-environment/fresh-surface-water (Accessed: November 9, 2021).

Duan, K., Caldwell, P. V, Sun, G., McNulty, S.G., Zhang, Y., Shuster, E., Liu, B. & Bolstad, P. V (2019) "Understanding the role of regional water connectivity in mitigating climate change impacts on surface water supply stress in the United States," *Journal of Hydrology*, 570, pp. 80–95. doi:https://doi.org/10.1016/j.jhydrol.2019.01.011.

Duran-Encalada, J.A., Paucar-Caceres, A., Bandala, E.R. & Wright, G.H. (2017) "The impact of global climate change on water quantity and quality: A system dynamics approach to the US–Mexican transborder region," *European Journal of Operational Research*, 256(2), pp. 567–581. doi:https://doi.org/10.1016/j.ejor.2016.06.016.

Easterling, D.R., Arnold, J.R., Knutson, T., Kunkel, K.E., LeGrande, A.N., Leung, L.R., Vose, R.S., Waliser, D.E. & Wehner, M.F. (2017) *Ch. 7: Precipitation Change in the United States. Climate Science Special Report: Fourth National Climate Assessment, Volume I.* Washington, DC. doi:10.7930/J0H993CC.

EPA (2016) *Climate change indicators in the United States. Fourth edition.* Available at: www.epa.gov/climate-indicators.

Erler, A.R., Frey, S.K., Khader, O., D'Orgeville, M., Park, Y., Hwang, H., Lapen, D.R., Richard Peltier, W. & Sudicky, E.A. (2019) "Simulating Climate Change Impacts on Surface Water Resources Within a Lake-Affected Region Using Regional Climate Projections," *Water Resources Research*, 55(1), pp. 130–155. doi:10.1029/2018WR024381.

Ermida, S.L., Soares, P., Mantas, V., Göttsche, F.-M. & Trigo, I.F. (2020) "Google Earth Engine Open-Source Code for Land Surface Temperature Estimation from the Landsat Series," *Remote Sensing*, 12(9), p. 1471. doi:10.3390/rs12091471.

Everard, M. & Moggridge, H.L. (2012) "Rediscovering the value of urban rivers," *Urban Ecosystems*, 15(2), pp. 293–314. doi:10.1007/s11252-011-0174-7.

Fang, Y., Ceola, S., Paik, K., McGrath, G., Rao, P.S.C., Montanari, A. & Jawitz, J.W. (2018) "Globally Universal Fractal Pattern of Human Settlements in River Networks," *Earth's Future*, 6(8), pp. 1134–1145. doi:https://doi.org/10.1029/2017EF000746.

Fang, Y. & Jawitz, J.W. (2019) "The evolution of human population distance to water in the

USA from 1790 to 2010," *Nature Communications*, 10(1), p. 430. doi:10.1038/s41467-019-08366-z.

FAO (2012) *Coping with water scarcity An action framework for agriculture and food security*. Rome.

FAO (2017) *Water for Sustainable Food and Agriculture - A report produced for the G20 Presidency of Germany*. Rome. Available at: https://www.fao.org/3/i7959e/i7959e.pdf.

FAO (2020) *The State of Food and Agriculture 2020*. FAO. doi:10.4060/cb1447en.

Faroughi, M., Karimimoshaver, M., Aram, F., Solgi, E., Mosavi, A., Nabipour, N. & Chau, K.-W. (2020) "Computational modeling of land surface temperature using remote sensing data to investigate the spatial arrangement of buildings and energy consumption relationship," *Engineering Applications of Computational Fluid Mechanics*, 14(1), pp. 254–270. doi:10.1080/19942060.2019.1707711.

Ferguson, I.M. & Maxwell, R.M. (2012) "Human impacts on terrestrial hydrology: climate change versus pumping and irrigation," *Environmental Research Letters*, 7(4), p. 044022. doi:10.1088/1748-9326/7/4/044022.

Fernández, I.C. (2019) "A multiple-class distance-decaying approach for mapping temperature reduction ecosystem services provided by urban vegetation in Santiago de Chile," *Ecological Economics*, 161, pp. 193–201. doi:https://doi.org/10.1016/j.ecolecon.2019.03.029.

Figueiredo, O., Guimarães, P. & Woodward, D. (2015) "Industry localization, distance decay, and knowledge spillovers: Following the patent paper trail," *Journal of Urban Economics*, 89, pp. 21–31. doi:https://doi.org/10.1016/j.jue.2015.06.003.

Firoozi, F., Mahmoudi, P., Jahanshahi, S.M.A., Tavousi, T., Liu, Y. & Liang, Z. (2020) "Modeling changes trend of time series of land surface temperature (LST) using satellite remote sensing productions (case study: Sistan plain in east of Iran)," *Arabian Journal of Geosciences*, 13(10), p. 367. doi:10.1007/s12517-020-05314-w.

Fitzhugh, T.W. & Richter, B.D. (2004) "Quenching Urban Thirst: Growing Cities and Their Impacts on Freshwater Ecosystems," *BioScience*, 54(8), pp. 741–754. doi:10.1641/0006-3568(2004)054[0741:QUTGCA]2.0.CO;2.

Flávio, H.M., Ferreira, P., Formigo, N. & Svendsen, J.C. (2017) "Reconciling agriculture and stream restoration in Europe: A review relating to the EU Water Framework Directive," *Science of The Total Environment*, 596–597, pp. 378–395. doi:10.1016/j.scitotenv.2017.04.057.

Florczyk, A.J., Melchiorri, M., Zeidler, J., Corbane, C., Schiavina, M., Freire, S., Sabo, F., Politis, P., Esch, T. & Pesaresi, M. (2020) "The Generalised Settlement Area: mapping the Earth surface in the vicinity of built-up areas," *International Journal of Digital Earth*, 13(1), pp. 45–60. doi:10.1080/17538947.2018.1550121.

Flörke, M., Kynast, E., Bärlund, I., Eisner, S., Wimmer, F. & Alcamo, J. (2013) "Domestic and industrial water uses of the past 60 years as a mirror of socio-economic development: A global simulation study," *Global Environmental Change*, 23(1), pp. 144–156.

doi:10.1016/j.gloenvcha.2012.10.018.

Flörke, M., Schneider, C. & McDonald, R.I. (2018) "Water competition between cities and agriculture driven by climate change and urban growth," *Nature Sustainability*, 1(1), pp. 51–58. doi:10.1038/s41893-017-0006-8.

Fotheringham, A.S. (1981) "Spatial Structure and Distance-Decay Parameters," *Annals of the Association of American Geographers*, 71(3), pp. 425–436. doi:https://doi.org/10.1111/j.1467-8306.1981.tb01367.x.

Garrick, D., De Stefano, L., Yu, W., Jorgensen, I., O'Donnell, E., Turley, L., Aguilar-Barajas, I., Dai, X., de Souza Leão, R., Punjabi, B., Schreiner, B., Svensson, J. & Wight, C. (2019) "Rural water for thirsty cities: a systematic review of water reallocation from rural to urban regions," *Environmental Research Letters*, 14(4), p. 043003. doi:10.1088/1748-9326/ab0db7.

Georgakakos, A., Fleming, P., Dettinger, M., Peters-Lidard, C., Richmond, T. (T. C.., Reckhow, K., White, K. & Yates, D. (2014) *Ch. 3: Water Resources. Climate Change Impacts in the United States: The Third National Climate Assessment.* Washington, DC. doi:10.7930/J0G44N6T.

Goel, R. (2018) "Distance-decay functions of travel to work trips in India," *Data in Brief*, 21, pp. 50–58. doi:https://doi.org/10.1016/j.dib.2018.09.096.

Goldmann, K., Schröter, K., Pena, R., Schöning, I., Schrumpf, M., Buscot, F., Polle, A. & Wubet, T. (2016) "Divergent habitat filtering of root and soil fungal communities in temperate beech forests," *Scientific Reports*, 6(1), p. 31439. doi:10.1038/srep31439.

Graf, L., Bach, H. & Tiede, D. (2020) "Semantic Segmentation of Sentinel-2 Imagery for Mapping Irrigation Center Pivots," *Remote Sensing*, 12(23), p. 3937. doi:10.3390/rs12233937.

Granzotti, R.V., Miranda, L.E., Agostinho, A.A. & Gomes, L.C. (2018) "Downstream impacts of dams: shifts in benthic invertivorous fish assemblages," *Aquatic Sciences*, 80(3), p. 28. doi:10.1007/s00027-018-0579-y.

Grill, G., Lehner, B., Thieme, M., Geenen, B., Tickner, D., Antonelli, F., Babu, S., Borrelli, P., Cheng, L., Crochetiere, H., Ehalt Macedo, H., Filgueiras, R., Goichot, M., Higgins, J., Hogan, Z., Lip, B., McClain, M.E., Meng, J., Mulligan, M., Nilsson, C., Olden, J.D., Opperman, J.J., Petry, P., Reidy Liermann, C., Sáenz, L., Salinas-Rodríguez, S., Schelle, P., Schmitt, R.J.P., Snider, J., Tan, F., Tockner, K., Valdujo, P.H., van Soesbergen, A. & Zarfl, C. (2019) "Mapping the world's free-flowing rivers," *Nature*, 569(7755), pp. 215–221. doi:10.1038/s41586-019-1111-9.

Grizzetti, B., Pistocchi, A., Liquete, C., Udias, A., Bouraoui, F. & van de Bund, W. (2017) "Human pressures and ecological status of European rivers," *Scientific Reports*, 7(1), p. 205. doi:10.1038/s41598-017-00324-3.

Haddeland, I., Skaugen, T. & Lettenmaier, D.P. (2006) "Anthropogenic impacts on continental surface water fluxes," *Geophysical Research Letters*, 33(8). doi:https://doi.org/10.1029/2006GL026047.

Halás, M., Klapka, P. & Kladivo, P. (2014) "Distance-decay functions for daily travel-to-work flows," *Journal of Transport Geography*, 35, pp. 107–119. doi:https://doi.org/10.1016/j.jtrangeo.2014.02.001.

He, C., Liu, Z., Gou, S., Zhang, Q., Zhang, J. & Xu, L. (2019) "Detecting global urban expansion over the last three decades using a fully convolutional network," *Environmental Research Letters*, 14(3), p. 034008. doi:10.1088/1748-9326/aaf936.

Hoekstra, A.Y., Buurman, J. & van Ginkel, K.C.H. (2018) "Urban water security: A review," *Environmental Research Letters*, 13(5), p. 053002. doi:10.1088/1748-9326/aaba52.

Hoerling, M., Eischeid, J., Perlwitz, J., Quan, X.-W., Wolter, K. & Cheng, L. (2016) "Characterizing Recent Trends in U.S. Heavy Precipitation," *Journal of Climate*, 29(7), pp. 2313–2332. doi:10.1175/JCLI-D-15-0441.1.

Hong, Y., Tang, G., Ma, Y., Huang, Q., Han, Z., Zeng, Z., Yang, Y., Wang, C. & Guo, X. (2018) "Remote Sensing Precipitation: Sensors, Retrievals, Validations, and Applications," in, pp. 1–23. doi:10.1007/978-3-662-47871-4_4-1.

Hoogeveen, J., Faurès, J.-M., Peiser, L., Burke, J. & van de Giesen, N. (2015) "GlobWat – a global water balance model to assess water use in irrigated agriculture," *Hydrology and Earth System Sciences*, 19(9), pp. 3829–3844. doi:10.5194/hess-19-3829-2015.

Huang, C., Chen, Y., Zhang, S. & Wu, J. (2018) "Detecting, Extracting, and Monitoring Surface Water From Space Using Optical Sensors: A Review," *Reviews of Geophysics*, 56(2), pp. 333–360. doi:https://doi.org/10.1029/2018RG000598.

Huang, S., Tang, L., Hupy, J.P., Wang, Y. & Shao, G. (2021) "A commentary review on the use of normalized difference vegetation index (NDVI) in the era of popular remote sensing," *Journal of Forestry Research*, 32(1), pp. 1–6. doi:10.1007/s11676-020-01155-1.

IPCC (2014) "Freshwater resources," in *Climate Change 2014: Impacts, Adaptation, and Vulnerability. Part A: Global and Sectoral Aspects. Contribution of Working Group II to the Fifth Assessment Report of the Intergovernmental Panel on Climate Change*. Cambridge: Cambridge University Press., pp. 229–270. doi:doi:10.1017/CBO9781107415379.008.

IPCC, Masson-Delmotte, V., Zhai, P., Pirani, A., Connors, S.L., Péan, C., Berger, S., Caud, N., Chen, Y., Goldfarb, L., Gomis, M.I., Huang, M., Leitzell, K., Lonnoy, E., Matthews, J.B.R., Maycock, T.K., Waterfield, T., Yelekçi, O., Yu, R. & B., Z. (2021) *Climate Change 2021: The Physical Science Basis. Contribution of Working Group I to the Sixth Assessment Report of the Intergovernmental Panel on Climate Change*, *Cambridge University Press*. Available at: https://www.ipcc.ch/report/ar6/wg1/.

Jenkins, W.A., Murray, B.C., Kramer, R.A. & Faulkner, S.P. (2010) "Valuing ecosystem services from wetlands restoration in the Mississippi Alluvial Valley," *Ecological Economics*, 69(5), pp. 1051–1061. doi:https://doi.org/10.1016/j.ecolecon.2009.11.022.

Karthikeyan, L., Chawla, I. & Mishra, A.K. (2020) "A review of remote sensing applications in agriculture for food security: Crop growth and yield, irrigation, and crop losses," *Journal of Hydrology*, 586, p. 124905. doi:10.1016/j.jhydrol.2020.124905.

Kaushal, S., Gold, A. & Mayer, P. (2017) "Land Use, Climate, and Water Resources—Global Stages of Interaction," *Water*, 9(10), p. 815. doi:10.3390/w9100815.

Khatri, N. & Tyagi, S. (2015) "Influences of natural and anthropogenic factors on surface and groundwater quality in rural and urban areas," *Frontiers in Life Science*, 8(1), pp. 23–39. doi:10.1080/21553769.2014.933716.

Kifle Arsiso, B., Mengistu Tsidu, G., Stoffberg, G.H. & Tadesse, T. (2017) "Climate change and population growth impacts on surface water supply and demand of Addis Ababa, Ethiopia," *Climate Risk Management*, 18, pp. 21–33. doi:10.1016/j.crm.2017.08.004.

Konapala, G., Mishra, A.K., Wada, Y. & Mann, M.E. (2020) "Climate change will affect global water availability through compounding changes in seasonal precipitation and evaporation," *Nature Communications*, 11(1), p. 3044. doi:10.1038/s41467-020-16757-w.

Kummu, M., de Moel, H., Ward, P.J. & Varis, O. (2011) "How Close Do We Live to Water? A Global Analysis of Population Distance to Freshwater Bodies," *PLoS ONE*. Edited by M. Perc, 6(6), p. e20578. doi:10.1371/journal.pone.0020578.

Kummu, M., Guillaume, J.H.A., de Moel, H., Eisner, S., Flörke, M., Porkka, M., Siebert, S., Veldkamp, T.I.E. & Ward, P.J. (2016) "The world's road to water scarcity: shortage and stress in the 20th century and pathways towards sustainability," *Scientific Reports*, 6(1), p. 38495. doi:10.1038/srep38495.

Kundzewicz, Z.W. (2008) "Climate change impacts on the hydrological cycle," *Ecohydrology & Hydrobiology*, 8(2), pp. 195–203. doi:https://doi.org/10.2478/v10104-009-0015-y.

Levizzani, V. & Cattani, E. (2019) "Satellite Remote Sensing of Precipitation and the Terrestrial Water Cycle in a Changing Climate," *Remote Sensing*, 11(19), p. 2301. doi:10.3390/rs11192301.

Li, C., Sun, G., Caldwell, P. V, Cohen, E., Fang, Y., Zhang, Y., Oudin, L., Sanchez, G.M. & Meentemeyer, R.K. (2020) "Impacts of Urbanization on Watershed Water Balances Across the Conterminous United States," *Water Resources Research*, 56(7), p. e2019WR026574. doi:https://doi.org/10.1029/2019WR026574.

Li, L. & Zha, Y. (2019) "Estimating monthly average temperature by remote sensing in China," *Advances in Space Research*, 63(8), pp. 2345–2357. doi:10.1016/j.asr.2018.12.039.

Li, Z., Wang, K., Zhou, C. & Wang, L. (2016) "Modelling the true monthly mean temperature from continuous measurements over global land," *International Journal of Climatology*, 36(4), pp. 2103–2110. doi:10.1002/joc.4445.

Liu, J., Yang, H., Gosling, S.N., Kummu, M., Flörke, M., Pfister, S., Hanasaki, N., Wada, Y., Zhang, X., Zheng, C., Alcamo, J. & Oki, T. (2017) "Water scarcity assessments in the past, present, and future," *Earth's Future*, 5(6), pp. 545–559. doi:10.1002/2016EF000518.

Liu, X., Huang, Y., Xu, X., Li, X.X., Li, X.X., Ciais, P., Lin, P., Gong, K., Ziegler, A.D., Chen, A., Gong, P., Chen, J., Hu, G., Chen, Y., Wang, S., Wu, Q., Huang, K., Estes, L. & Zeng, Z. (2020) "High-spatiotemporal-resolution mapping of global urban change from 1985 to 2015," *Nature Sustainability*, 3(7), pp. 564–570. doi:10.1038/s41893-020-0521-x.

Liyanage, C.P. & Yamada, K. (2017) "Impact of Population Growth on the Water Quality of Natural Water Bodies," *Sustainability* . doi:10.3390/su9081405.

Lund, J., Medellin-Azuara, J., Durand, J. & Stone, K. (2018) "Lessons from California's 2012–2016 Drought," *Journal of Water Resources Planning and Management*, 144(10), p. 04018067. doi:10.1061/(ASCE)WR.1943-5452.0000984.

Lyons, W.B. (2014) "Water and urbanization," *Environmental Research Letters*, 9(11), p. 111002. doi:10.1088/1748-9326/9/11/111002.

MacDonald, G.M. (2010) "Water, climate change, and sustainability in the southwest," *Proceedings of the National Academy of Sciences*, 107(50), pp. 21256–21262. doi:10.1073/pnas.0909651107.

Mancosu, N., Snyder, R.L., Kyriakakis, G. & Spano, D. (2015) "Water Scarcity and Future Challenges for Food Production," *Water* . doi:10.3390/w7030975.

Marconcini, M., Metz-Marconcini, A., Üreyen, S., Palacios-Lopez, D., Hanke, W., Bachofer, F., Zeidler, J., Esch, T., Gorelick, N., Kakarla, A., Paganini, M. & Strano, E. (2020) "Outlining where humans live, the World Settlement Footprint 2015," *Scientific Data*, 7(1), p. 242. doi:10.1038/s41597-020-00580-5.

Mård, J., Di Baldassarre, G. & Mazzoleni, M. (2018) "Nighttime light data reveal how flood protection shapes human proximity to rivers," *Science Advances*, 4(8). doi:10.1126/sciadv.aar5779.

Martínez, L.M. & Viegas, J.M. (2013) "A new approach to modelling distance-decay functions for accessibility assessment in transport studies," *Journal of Transport Geography*, 26, pp. 87–96. doi:https://doi.org/10.1016/j.jtrangeo.2012.08.018.

McDonald, R.I., Douglas, I., Revenga, C., Hale, R., Grimm, N., Grönwall, J. & Fekete, B. (2011a) "Global Urban Growth and the Geography of Water Availability, Quality, and Delivery," *AMBIO*, 40(5), pp. 437–446. doi:10.1007/s13280-011-0152-6.

McDonald, R.I., Douglas, I., Grimm, N., Hale, R., Revenga, C., Gronwall, J. & Fekete, B. (2011b) "Implications of fast urban growth for freshwater provision," *Ambio*, 40, pp. 437–447.

McDonald, R.I., Green, P., Balk, D., Fekete, B.M., Revenga, C., Todd, M. & Montgomery, M. (2011c) "Urban growth, climate change, and freshwater availability," *Proceedings of the National Academy of Sciences*, 108(15), pp. 6312–6317. doi:10.1073/pnas.1011615108.

McDonald, R.I., Weber, K., Padowski, J., Flörke, M., Schneider, C., Green, P.A., Gleeson, T., Eckman, S., Lehner, B., Balk, D., Boucher, T., Grill, G. & Montgomery, M. (2014) "Water on an urban planet: Urbanization and the reach of urban water infrastructure," *Global*

Environmental Change, 27, pp. 96–105. doi:https://doi.org/10.1016/j.gloenvcha.2014.04.022.

McGrane, S.J. (2016) "Impacts of urbanisation on hydrological and water quality dynamics, and urban water management: a review," *Hydrological Sciences Journal*, 61(13), pp. 2295–2311. doi:10.1080/02626667.2015.1128084.

McKinnon, K.A. & Deser, C. (2021) "The Inherent Uncertainty of Precipitation Variability, Trends, and Extremes due to Internal Variability, with Implications for Western U.S. Water Resources," *Journal of Climate*, 34(24), pp. 9605–9622. doi:10.1175/JCLI-D-21-0251.1.

Mekonnen, M.M. & Hoekstra, A.Y. (2016) "Four billion people facing severe water scarcity," *Science Advances*, 2(2). doi:10.1126/sciadv.1500323.

Melchiorri, M., Florczyk, A., Freire, S., Schiavina, M., Pesaresi, M. & Kemper, T. (2018) "Unveiling 25 Years of Planetary Urbanization with Remote Sensing: Perspectives from the Global Human Settlement Layer," *Remote Sensing*, 10(5), p. 768. doi:10.3390/rs10050768.

Melchiorri, M., Pesaresi, M., Florczyk, A., Corbane, C. & Kemper, T. (2019) "Principles and Applications of the Global Human Settlement Layer as Baseline for the Land Use Efficiency Indicator—SDG 11.3.1," *ISPRS International Journal of Geo-Information*, 8(2), p. 96. doi:10.3390/ijgi8020096.

Mueller, N., Lewis, A., Roberts, D., Ring, S., Melrose, R., Sixsmith, J., Lymburner, L., McIntyre, A., Tan, P., Curnow, S. & Ip, A. (2016) "Water observations from space: Mapping surface water from 25 years of Landsat imagery across Australia," *Remote Sensing of Environment*, 174, pp. 341–352. doi:10.1016/j.rse.2015.11.003.

Nair, S., Johnson, J. & Wang, C. (2013) "Efficiency of Irrigation Water Use: A Review from the Perspectives of Multiple Disciplines," *Agronomy Journal*, 105(2), pp. 351–363. doi:10.2134/agronj2012.0421.

Nie, W., Zaitchik, B.F., Rodell, M., Kumar, S. V., Arsenault, K.R. & Badr, H.S. (2021) "Irrigation Water Demand Sensitivity to Climate Variability Across the Contiguous United States," *Water Resources Research*, 57(3). doi:10.1029/2020WR027738.

O'Driscoll, M., Clinton, S., Jefferson, A., Manda, A. & McMillan, S. (2010) "Urbanization Effects on Watershed Hydrology and In-Stream Processes in the Southern United States," *Water* . doi:10.3390/w2030605.

Okello, C., Tomasello, B., Greggio, N., Wambiji, N. & Antonellini, M. (2015) "Impact of Population Growth and Climate Change on the Freshwater Resources of Lamu Island, Kenya," *Water*, 7(12), pp. 1264–1290. doi:10.3390/w7031264.

Oki, T. & Kanae, S. (2006) "Global Hydrological Cycles and World Water Resources," *Science*, 313(5790), pp. 1068–1072. doi:10.1126/science.1128845.

Ozdogan, M., Yang, Y., Allez, G. & Cervantes, C. (2010) "Remote Sensing of Irrigated Agriculture: Opportunities and Challenges," *Remote Sensing*, 2(9), pp. 2274–2304. doi:10.3390/rs2092274.

Padowski, J.C. & Jawitz, J.W. (2012) "Water availability and vulnerability of 225 large cities in the United States," *Water Resources Research*, 48(12). doi:https://doi.org/10.1029/2012WR012335.

Padowski, J.C. & Gorelick, S.M. (2014) "Global analysis of urban surface water supply vulnerability," *Environmental Research Letters*, 9(10), p. 104004. doi:10.1088/1748-9326/9/10/104004.

Pageot, Y., Baup, F., Inglada, J., Baghdadi, N. & Demarez, V. (2020) "Detection of Irrigated and Rainfed Crops in Temperate Areas Using Sentinel-1 and Sentinel-2 Time Series," *Remote Sensing*, 12(18), p. 3044. doi:10.3390/rs12183044.

Paiva, A.C. da E., Nascimento, N., Rodriguez, D.A., Tomasella, J., Carriello, F. & Rezende, F.S. (2020) "Urban expansion and its impact on water security: The case of the Paraíba do Sul River Basin, São Paulo, Brazil," *Science of The Total Environment*, 720, p. 137509. doi:https://doi.org/10.1016/j.scitotenv.2020.137509.

Palazzoli, I., Montanari, A. & Ceola, S. (2021) "Surface Water Loss map and Urbanization map." Zenodo. doi:10.5281/zenodo.4472831.

Palazzoli, I., Montanari, A. & Ceola, S. (2022) "Influence of urban areas on surface water loss in the contiguous United States," *AGU Advances*, (3), p. e2021AV000519, in press.

Paterson, W., Rushforth, R., Ruddell, B., Konar, M., Ahams, I., Gironás, J., Mijic, A. & Mejia, A. (2015) "Water Footprint of Cities: A Review and Suggestions for Future Research," *Sustainability*, 7(7), pp. 8461–8490. doi:10.3390/su7078461.

Pekel, J.-F., Cottam, A., Gorelick, N. & Belward, A.S. (2016) "High-resolution mapping of global surface water and its long-term changes," *Nature*, 540(7633), pp. 418–422. doi:10.1038/nature20584.

Pendergrass, A.G., Knutti, R., Lehner, F., Deser, C. & Sanderson, B.M. (2017) "Precipitation variability increases in a warmer climate," *Scientific Reports*, 7(1), p. 17966. doi:10.1038/s41598-017-17966-y.

Pervez, M.S. & Brown, J.F. (2010) "Mapping Irrigated Lands at 250-m Scale by Merging MODIS Data and National Agricultural Statistics," *Remote Sensing*, 2(10), pp. 2388–2412. doi:10.3390/rs2102388.

Petpongpan, C., Ekkawatpanit, C. & Kositgittiwong, D. (2020) "Climate Change Impact on Surface Water and Groundwater Recharge in Northern Thailand," *Water* . doi:10.3390/w12041029.

Pimentel, D., Houser, J., Preiss, E., White, O., Fang, H., Mesnick, L., Barsky, T., Tariche, S., Schreck, J. & Alpert, S. (1997) "Water Resources: Agriculture, the Environment, and Society," *BioScience*, 47(2), pp. 97–106. doi:10.2307/1313020.

Poff, N.L., Allan, J.D., Bain, M.B., Karr, J.R., Prestegaard, K.L., Richter, B.D., Sparks, R.E. & Stromberg, J.C. (1997) "The Natural Flow Regime," *BioScience*, 47(11), pp. 769–784.

doi:10.2307/1313099.

Prakash, S. & Norouzi, H. (2020) "Land surface temperature variability across India: a remote sensing satellite perspective," *Theoretical and Applied Climatology*, 139(1–2), pp. 773–784. doi:10.1007/s00704-019-03010-8.

Regan, P. (2012) "Call to stewardship," in. Available at: https://www.researchgate.net/publication/286384014_CALL_TO_STEWARDSHIP.

Requia, W.J., Roig, H.L., Adams, M.D., Zanobetti, A. & Koutrakis, P. (2016) "Mapping distance-decay of cardiorespiratory disease risk related to neighborhood environments," *Environmental Research*, 151, pp. 203–215. doi:https://doi.org/10.1016/j.envres.2016.07.038.

Richter, B.D., Abell, D., Bacha, E., Brauman, K., Calos, S., Cohn, A., Disla, C., O'Brien, S.F., Hodges, D., Kaiser, S., Loughran, M., Mestre, C., Reardon, M. & Siegfried, E. (2013) "Tapped out: how can cities secure their water future?," *Water Policy*, 15(3), pp. 335–363. doi:10.2166/wp.2013.105.

Rodell, M., Famiglietti, J.S., Wiese, D.N., Reager, J.T., Beaudoing, H.K., Landerer, F.W. & Lo, M.-H. (2018) "Emerging trends in global freshwater availability," *Nature*, 557(7707), pp. 651–659. doi:10.1038/s41586-018-0123-1.

Rost, S., Gerten, D., Bondeau, A., Lucht, W., Rohwer, J. & Schaphoff, S. (2008) "Agricultural green and blue water consumption and its influence on the global water system," *Water Resources Research*, 44(9). doi:10.1029/2007WR006331.

Schaffer-Smith, D., Swenson, J.J., Barbaree, B. & Reiter, M.E. (2017) "Three decades of Landsat-derived spring surface water dynamics in an agricultural wetland mosaic; Implications for migratory shorebirds," *Remote Sensing of Environment*, 193, pp. 180–192. doi:10.1016/j.rse.2017.02.016.

Seaber, P.R., Kapinos, F.P. & Knapp, G.L. (1987) *Hydrologic unit maps*, *Water Supply Paper*. doi:10.3133/wsp2294.

Seydi, S.T., Hasanlou, M. & Amani, M. (2020) "A New End-to-End Multi-Dimensional CNN Framework for Land Cover/Land Use Change Detection in Multi-Source Remote Sensing Datasets," *Remote Sensing*, 12(12), p. 2010. doi:10.3390/rs12122010.

Sheffield, J., Wood, E.F., Pan, M., Beck, H., Coccia, G., Serrat-Capdevila, A. & Verbist, K. (2018) "Satellite Remote Sensing for Water Resources Management: Potential for Supporting Sustainable Development in Data-Poor Regions," *Water Resources Research*, 54(12), pp. 9724–9758. doi:10.1029/2017WR022437.

Shen, H., Jiang, Y., Li, T., Cheng, Q., Zeng, C. & Zhang, L. (2020) "Deep learning-based air temperature mapping by fusing remote sensing, station, simulation and socioeconomic data," *Remote Sensing of Environment*, 240, p. 111692. doi:10.1016/j.rse.2020.111692.

Shiklomanov, I. (1993) *World fresh water resources*, *Water in crisis a guide to the world's fresh water* *resources*. Edited by Peter H. Gleick. Oxford University Press. Available at: https://www.quarks.de/wp-content/uploads/Water_in_Crisis_Chapter_2_Oxford_Univers.pdf.

Smedema, L.K., Abdel-Dayem, S. & Ochs, W.J. (2000) "Drainage and Agricultural Development," *Irrigation and Drainage Systems*, 14(3), pp. 223–235. doi:10.1023/A:1026570823692.

Starr, G. & Levison, J. (2014) "Identification of Crop Groundwater and Surface Water Consumption Using Blue and Green Virtual Water Contents at a Subwatershed Scale," *Environmental Processes*, 1(4), pp. 497–515. doi:10.1007/s40710-014-0040-8.

Sun, G. & Caldwell, P. (2015) "Impacts of Urbanization on Stream Water Quantity and Quality in the United States," *Water Resources IMPACT*, 17(1), pp. 17–20. Available at: https://www.jstor.org/stable/wateresoimpa.17.1.0017.

Sun, X. & Lall, U. (2015) "Spatially coherent trends of annual maximum daily precipitation in the United States," *Geophysical Research Letters*, 42(22), pp. 9781–9789. doi:https://doi.org/10.1002/2015GL066483.

Taylor, P.J. (1971) "Distance Transformation and Distance Decay Functions," *Geographical Analysis*, 3(3), pp. 221–238. doi:https://doi.org/10.1111/j.1538-4632.1971.tb00364.x.

Thornton, M.M., Shrestha, R., Wei, Y., Thornton, P.E., Kao, S. & Wilson, B.E. (2020a) "Daymet: Annual Climate Summaries on a 1-km Grid for North America, Version 4." ORNL Distributed Active Archive Center. doi:10.3334/ORNLDAAC/1852.

Thornton, M.M., Shrestha, R., Wei, Y., Thornton, P.E., Kao, S. & Wilson, B.E. (2020b) "Daymet: Monthly Climate Summaries on a 1-km Grid for North America, Version 4." ORNL Distributed Active Archive Center. doi:10.3334/ORNLDAAC/1855.

Tidwell, V., Moreland, B., Shaneyfelt, C. & Kobos, P. (2017) "Mapping water availability, cost and projected consumptive use in the Eastern United States with comparisons to the West," *Environmental Research Letters*, 13. doi:10.1088/1748-9326/aa9907.

Tobler, W.R. (1970) "A Computer Movie Simulating Urban Growth in the Detroit Region," *Economic Geography*, 46, pp. 234–240. doi:10.2307/143141.

Tulbure, M.G., Broich, M., Stehman, S. V. & Kommareddy, A. (2016) "Surface water extent dynamics from three decades of seasonally continuous Landsat time series at subcontinental scale in a semi-arid region," *Remote Sensing of Environment*, 178, pp. 142–157. doi:10.1016/j.rse.2016.02.034.

UNESCO, U.-W. (2020) *United Nations World Water Development Report 2020: Water and Climate Change*. Paris.

United Nations (2019) *World Urbanization Prospects: The 2018 Revision*. New York: UN. doi:10.18356/b9e995fe-en.

US Census (2021) *Urbanized Areas and Urban Clusters: 2010*. Available at: https://www.census.gov/library/visualizations/2010/geo/ua2010_uas_and_ucs_map.html.

Van Loon, A.F., Stahl, K., Di Baldassarre, G., Clark, J., Rangecroft, S., Wanders, N., Gleeson, T., Van Dijk, A.I.J.M., Tallaksen, L.M., Hannaford, J., Uijlenhoet, R., Teuling, A.J., Hannah, D.M., Sheffield, J., Svoboda, M., Verbeiren, B., Wagener, T. & Van Lanen, H.A.J. (2016) "Drought in a human-modified world: reframing drought definitions, understanding, and analysis approaches," *Hydrology and Earth System Sciences*, 20(9), pp. 3631–3650. doi:10.5194/hess-20-3631-2016.

Varouchakis, E.A., Kamińska-Chuchmała, A., Kowalik, G., Spanoudaki, K. & Graña, M. (2021) "Combining Geostatistics and Remote Sensing Data to Improve Spatiotemporal Analysis of Precipitation," *Sensors*, 21(9), p. 3132. doi:10.3390/s21093132.

Venter, Z.S., Brousse, O., Esau, I. & Meier, F. (2020) "Hyperlocal mapping of urban air temperature using remote sensing and crowdsourced weather data," *Remote Sensing of Environment*, 242, p. 111791. doi:10.1016/j.rse.2020.111791.

Vörösmarty, C., Lettenmaier, D., Leveque, C., Meybeck, M., Pahl-Wostl, C., Alcamo, J., Cosgrove, W., Grassl, H., Hoff, H., Kabat, P., Lansigan, F., Lawford, R. & Naiman, R. (2004) "Humans transforming the global water system," *Eos, Transactions American Geophysical Union*, 85(48), pp. 509–514. doi:10.1029/2004EO480001.

Vörösmarty, C.J., McIntyre, P.B., Gessner, M.O., Dudgeon, D., Prusevich, A., Green, P., Glidden, S., Bunn, S.E., Sullivan, C.A., Liermann, C.R. & Davies, P.M. (2010) "Global threats to human water security and river biodiversity," *Nature*, 467(7315), pp. 555–561. doi:10.1038/nature09440.

Vose, R.S., Easterling, D.R., Kunkel, K.E., LeGrande, A.N. & Wehner, M.F. (2017) *Ch. 6: Temperature Changes in the United States. Climate Science Special Report: Fourth National Climate Assessment, Volume I*. Washington, DC. doi:10.7930/J0N29V45.

Wada, Y., van Beek, L.P.H. & Bierkens, M.F.P. (2012) "Nonsustainable groundwater sustaining irrigation: A global assessment," *Water Resources Research*, 48(6). doi:https://doi.org/10.1029/2011WR010562.

Wada, Y., van Beek, L.P.H., Wanders, N. & Bierkens, M.F.P. (2013) "Human water consumption intensifies hydrological drought worldwide," *Environmental Research Letters*, 8(3), p. 034036. doi:10.1088/1748-9326/8/3/034036.

Wada, Y. & Bierkens, M.F.P. (2014) "Sustainability of global water use: past reconstruction and future projections," *Environmental Research Letters*, 9(10), p. 104003. doi:10.1088/1748-9326/9/10/104003.

Wada, Y., Flörke, M., Hanasaki, N., Eisner, S., Fischer, G., Tramberend, S., Satoh, Y., van Vliet, M.T.H., Yillia, P., Ringler, C., Burek, P. & Wiberg, D. (2016) "Modeling global water use for the 21st century: the Water Futures and Solutions (WFaS) initiative and its approaches," *Geoscientific Model Development*, 9(1), pp. 175–222. doi:10.5194/gmd-9-175-2016.

Wada, Y., Bierkens, M.F.P., de Roo, A., Dirmeyer, P.A., Famiglietti, J.S., Hanasaki, N., Konar, M., Liu, J., Müller Schmied, H., Oki, T., Pokhrel, Y., Sivapalan, M., Troy, T.J., van Dijk, A.I.J.M., van Emmerik, T., Van Huijgevoort, M.H.J., Van Lanen, H.A.J., Vörösmarty, C.J., Wanders, N. & Wheater, H. (2017) "Human–water interface in hydrological modelling: current status and future directions," *Hydrology and Earth System Sciences*, 21(8), pp. 4169–4193. doi:10.5194/hess-21-4169-2017.

Wanders, N., Wada, Y. & Van Lanen, H.A.J. (2015) "Global hydrological droughts in the 21st century under a changing hydrological regime," *Earth System Dynamics*, 6(1), pp. 1–15. doi:10.5194/esd-6-1-2015.

Wanders, N. & Wada, Y. (2015) "Human and climate impacts on the 21st century hydrological drought," *Journal of Hydrology*, 526, pp. 208–220. doi:10.1016/j.jhydrol.2014.10.047.

Wang, C., Jia, M., Chen, N. & Wang, W. (2018) "Long-Term Surface Water Dynamics Analysis Based on Landsat Imagery and the Google Earth Engine Platform: A Case Study in the Middle Yangtze River Basin," *Remote Sensing* . doi:10.3390/rs10101635.

Wang, X. & Xie, H. (2018) "A Review on Applications of Remote Sensing and Geographic Information Systems (GIS) in Water Resources and Flood Risk Management," *Water*, 10(5), p. 608. doi:10.3390/w10050608.

Wang, X., Xiao, X., Zou, Z., Dong, J., Qin, Y., Doughty, R.B., Menarguez, M.A., Chen, B., Wang, J., Ye, H., Ma, J., Zhong, Q., Zhao, B. & Li, B. (2020) "Gainers and losers of surface and terrestrial water resources in China during 1989–2016," *Nature Communications*, 11(1), p. 3471. doi:10.1038/s41467-020-17103-w.

World Bank (2021) *Water in Agriculture : Towards Sustainable Agriculture*, *Washington, D.C. : World Bank Group*. Washington, D.C. Available at: http://documents1.worldbank.org/curated/en/875921614166983369/pdf/Water-in-Agriculture-Towards-Sustainable-Agriculture.pdf%0Ahttp://documents.worldbank.org/curated/en/875921614166983369/Water-in-Agriculture-Towards-Sustainable-Agriculture.

WWAP (2015) *The United Nations World Water Development Report 2015: Water for a Sustainable World.* Paris.

Xiong, L., Deng, R., Li, J., Liu, X., Qin, Y., Liang, Y. & Liu, Y. (2018) "Subpixel Surface Water Extraction (SSWE) Using Landsat 8 OLI Data," *Water*, 10(5). doi:10.3390/w10050653.

Xu, L., Chen, N., Moradkhani, H., Zhang, X. & Hu, C. (2020) "Improving Global Monthly and Daily Precipitation Estimation by Fusing Gauge Observations, Remote Sensing, and Reanalysis Data Sets," *Water Resources Research*, 56(3). doi:10.1029/2019WR026444.

Xu, Y. & Beekman, H.E. (2019) "Review: Groundwater recharge estimation in arid and semi-arid southern Africa," *Hydrogeology Journal*, 27(3), pp. 929–943. doi:10.1007/s10040-018-1898-8.

Yamazaki, D. & Trigg, M.A. (2016) "The dynamics of Earth's surface water," *Nature*, 540(7633), pp. 348–349. doi:10.1038/nature21100.

Yigzaw, W. & Hossain, F. (2016) "Water sustainability of large cities in the United States from the perspectives of population increase, anthropogenic activities, and climate change," *Earth's Future*, 4(12), pp. 603–617. doi:https://doi.org/10.1002/2016EF000393.

Yuan, Y., Lin, L., Chen, J., Sahli, H., Chen, Y., Wang, C. & Wu, B. (2019) "A New Framework for Modelling and Monitoring the Conversion of Cultivated Land to Built-up Land Based on a Hierarchical Hidden Semi-Markov Model Using Satellite Image Time Series," *Remote Sensing*, 11(2), p. 210. doi:10.3390/rs11020210.

Zhang, C. & Long, D. (2021) "Estimating Spatially Explicit Irrigation Water Use Based on Remotely Sensed Evapotranspiration and Modeled Root Zone Soil Moisture," *Water Resources Research*, 57(12). doi:10.1029/2021WR031382.

Zhang, T. (2011) "Distance-decay patterns of nutrient loading at watershed scale: Regression modeling with a special spatial aggregation strategy," *Journal of Hydrology*, 402(3), pp. 239–249. doi:https://doi.org/10.1016/j.jhydrol.2011.03.017.

Zhang, X., Zhou, J., Liang, S. & Wang, D. (2021) "A practical reanalysis data and thermal infrared remote sensing data merging (RTM) method for reconstruction of a 1-km all-weather land surface temperature," *Remote Sensing of Environment*, 260, p. 112437. doi:10.1016/j.rse.2021.112437.

Zhou, D., Zhao, S., Zhang, L., Sun, G. & Liu, Y. (2015) "The footprint of urban heat island effect in China," *Scientific Reports*, 5(1), p. 11160. doi:10.1038/srep11160.

Zhou, X., Guan**, H., Xie, H. & Wilson, J.L. (2009) "Analysis and optimization of NDVI definitions and areal fraction models in remote sensing of vegetation," *International Journal of Remote Sensing*, 30(3), pp. 721–751. doi:10.1080/01431160802392620.

Zhuang, X.W., Li, Y.P., Nie, S., Fan, Y.R. & Huang, G.H. (2018) "Analyzing climate change impacts on water resources under uncertainty using an integrated simulation-optimization approach," *Journal of Hydrology*, 556, pp. 523–538. doi:https://doi.org/10.1016/j.jhydrol.2017.11.016.

Zohaib, M. & Choi, M. (2020) "Satellite-based global-scale irrigation water use and its contemporary trends," *Science of The Total Environment*, 714, p. 136719. doi:10.1016/j.scitotenv.2020.136719.

Appendix A

This appendix contains all figures related to the study area, data, and methods presented in Chapter 3, 4, and 5.

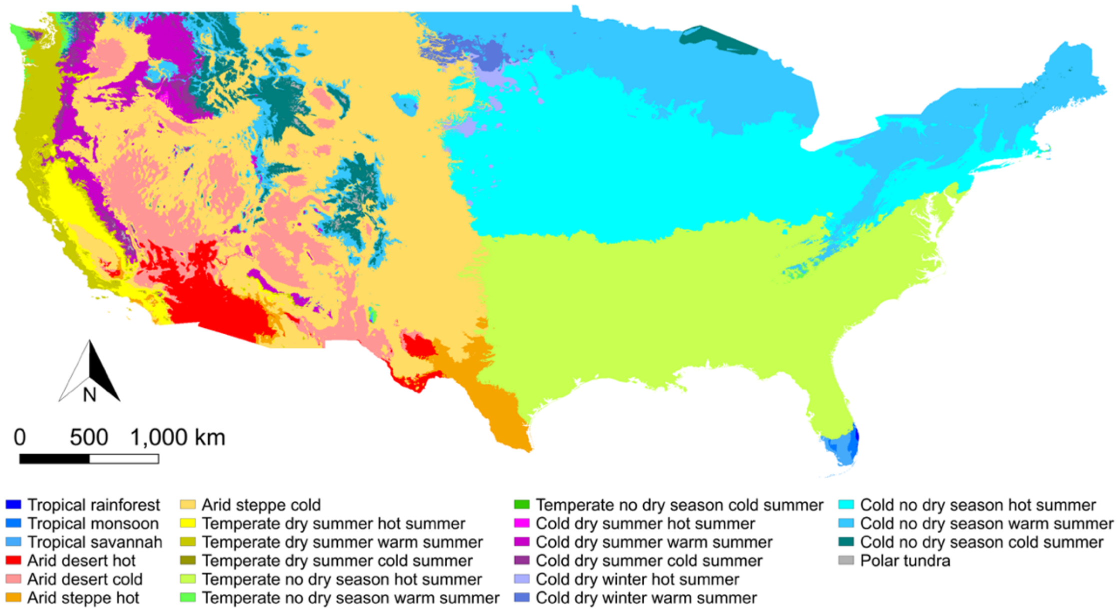
N
0
500
1,000 km
Tropical rainforest
Tropical monsoon
Tropical savannah
Arid desert hot
Arid desert cold
Arid steppe hot
Arid steppe cold
Temperate dry summer hot summer
Temperate dry summer warm summer
Temperate dry summer cold summer
Temperate no dry season hot summer
Temperate no dry season warm summer
Temperate no dry season cold summer
Cold dry summer hot summer
Cold dry summer warm summer
Cold dry summer cold summer
Cold dry winter hot summer
Cold dry winter warm summer
Cold no dry season hot summer
Cold no dry season warm summer
Cold no dry season cold summer
Polar tundra

Figure A1 Sub-types (22 classes) of climatic regions defined by the Köppen-Geiger climate classification system found within the CONUS.

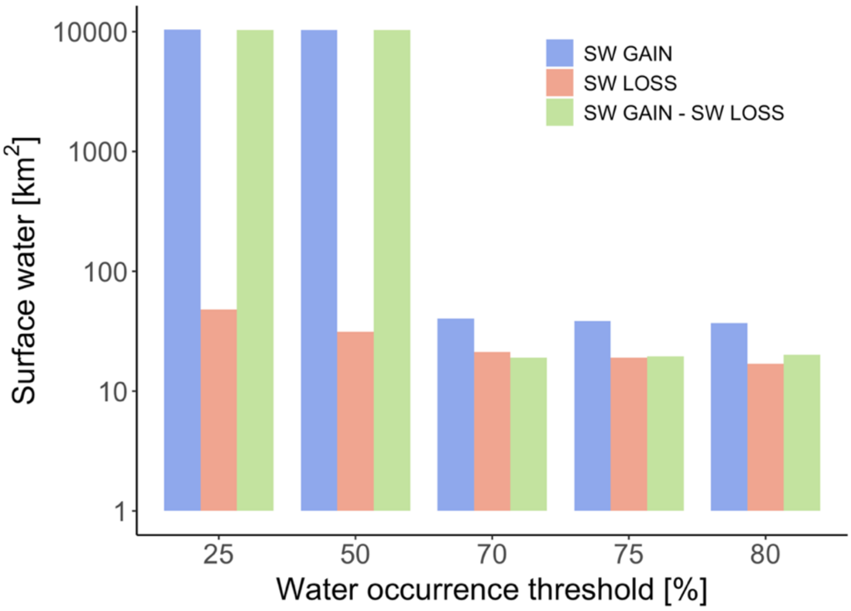

Figure A2 Total extent of surface water gain, loss, and net variation (gain – loss) across the CONUS as a function of the adopted threshold of change in the frequency of water observation.

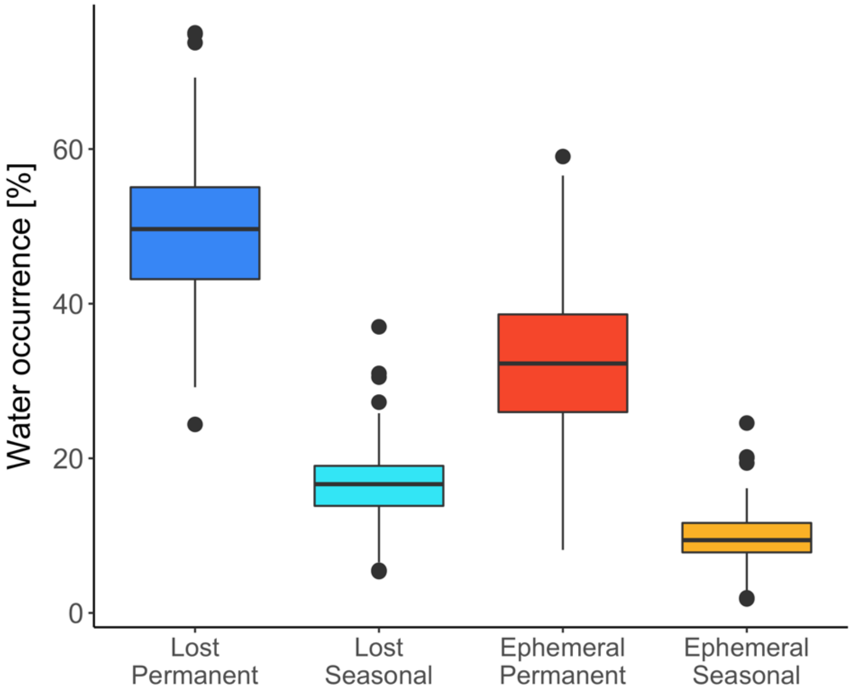

Figure A3 Variability of the water occurrence averaged over the river basins of the CONUS for each class of water transition included in the Surface Water Loss map.

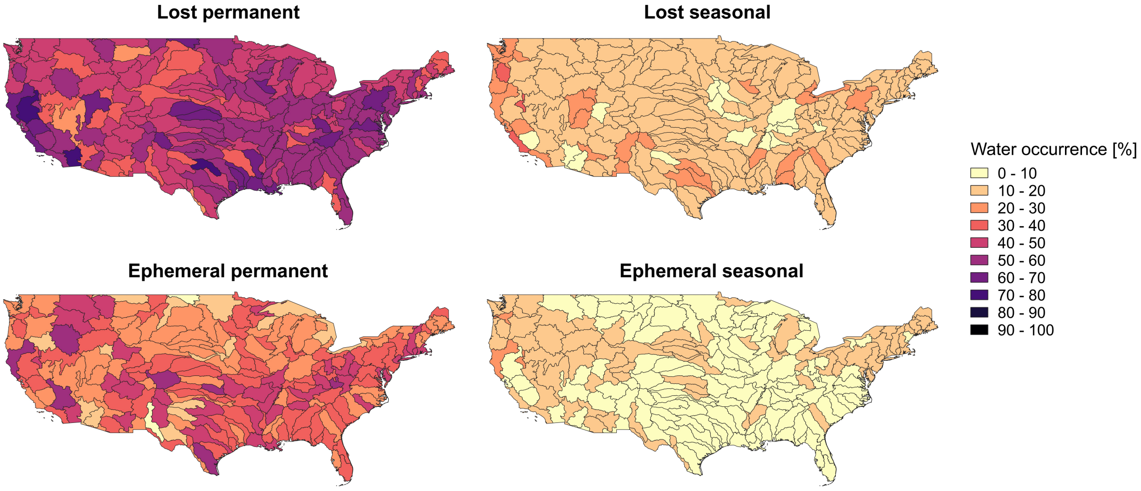
Lost permanent
Lost seasonal
Ephemeral permanent
Ephemeral seasonal
Water occurrence [%]
0 - 10
10 - 20
20 - 30
30 - 40
40 - 50
50 - 60
60 - 70
70 - 80
80 - 90
90 - 100

Figure A4 Spatial distribution of the average water occurrence for each class of water transition included in the Surface Water Loss map across the river basins of the CONUS.

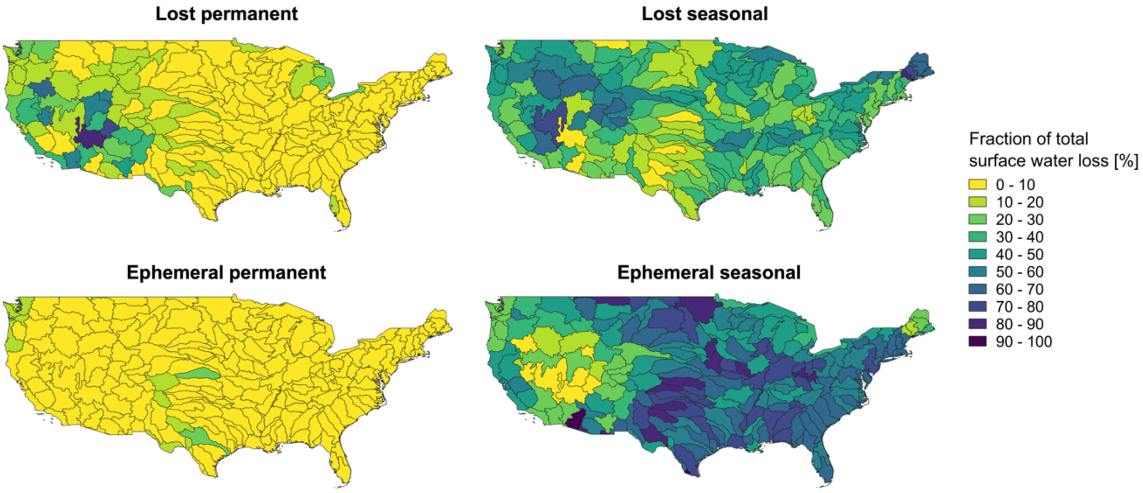
Lost permanent
Lost seasonal
Ephemeral permanent
Ephemeral seasonal
Fraction of total surface water loss [%]
0 - 10
10 - 20
20 - 30
30 - 40
40 - 50
50 - 60
60 - 70
70 - 80
80 - 90
90 - 100

Figure A5 Spatial distribution of the representativeness of each class of water transition included in the Surface Water Loss map across the river basins of the CONUS.

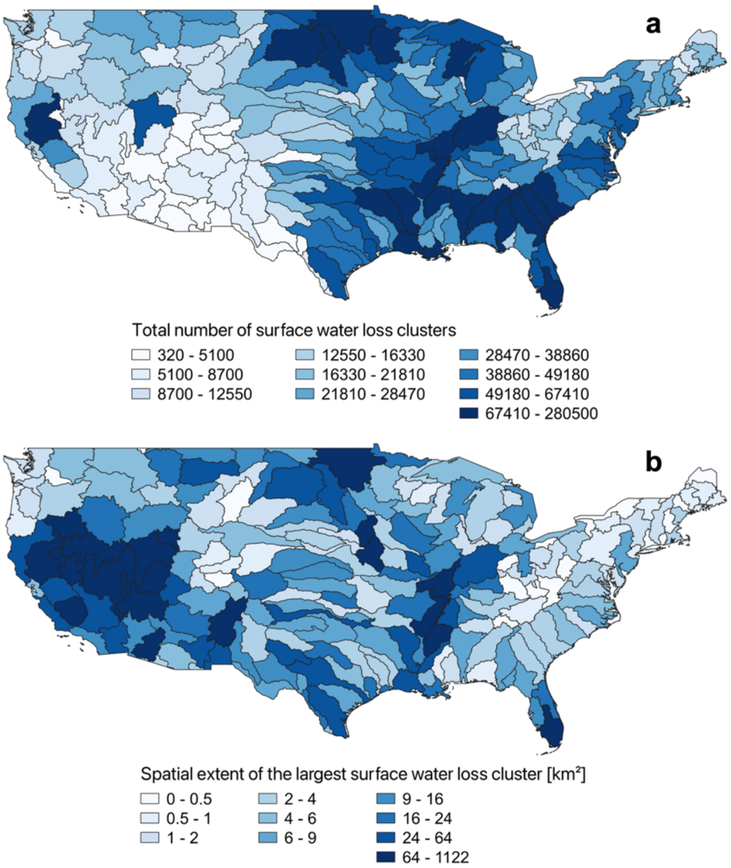
a
Total number of surface water loss clusters
320 - 5100
5100 - 8700
8700 - 12550
12550 - 16330
16330 - 21810
21810 - 28470
28470 - 38860
38860 - 49180
49180 - 67410
67410 - 280500
b
Spatial extent of the largest surface water loss cluster [km²]
0 - 0.5
0.5 - 1
1 - 2
2 - 4
4 - 6
6 - 9
9 - 16
16 - 24
24 - 64
64 - 1122

Figure A6 Spatial distribution of surface water loss clusters across the river basins of the CONUS. **a** Total number of surface water loss clusters. **b** Spatial extent of the largest surface water loss clusters.

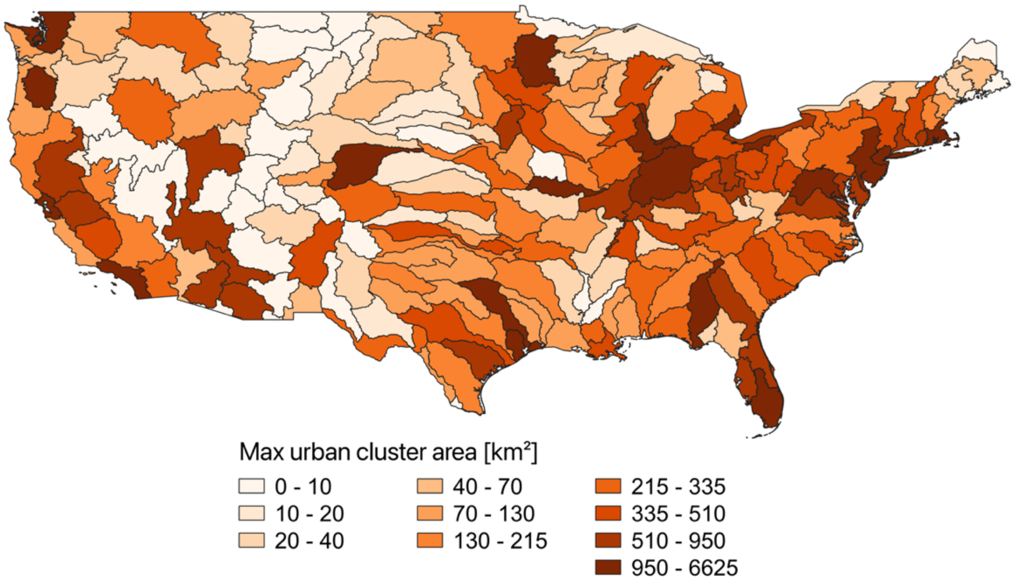

Figure A7 Spatial distribution of the extent of the largest urban clusters across river basins of the CONUS.

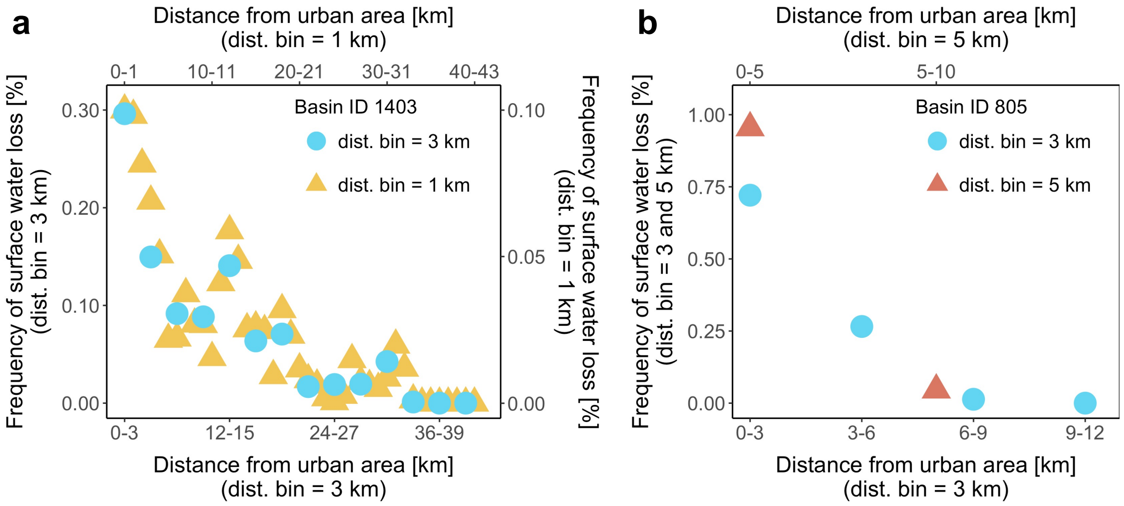

Figure A8 Comparison between the frequency of occurrence of surface water loss across distance classes based on 1, 3, and 5 km wide distance bins. **a**. Comparison between the frequency of occurrence of surface water loss based on 1 and 3 km wide distance bins in the Upper Colorado-Dolores Basin (ID 1403), belonging to the Upper Colorado Region (water resource region ID 14). The increase of the distance bin width from 1 to 3 km allows to remove data noise. The axes relative to the yellow triangles are the top and right axes. **b**. Comparison between the frequency of occurrence of surface water loss based on 3 and 5 km distance bins in the Boeuf-Tensas Basin (ID 805) belonging to the Lower Mississippi Region (water resource region ID 8). The increase of the distance bin width from 3 to 5 km halves the number of data points. The x axis relative to the red triangles is the top axis.

Appendix B

This appendix contains all figures and the table supporting the discussion of the results presented in Chapter 5.

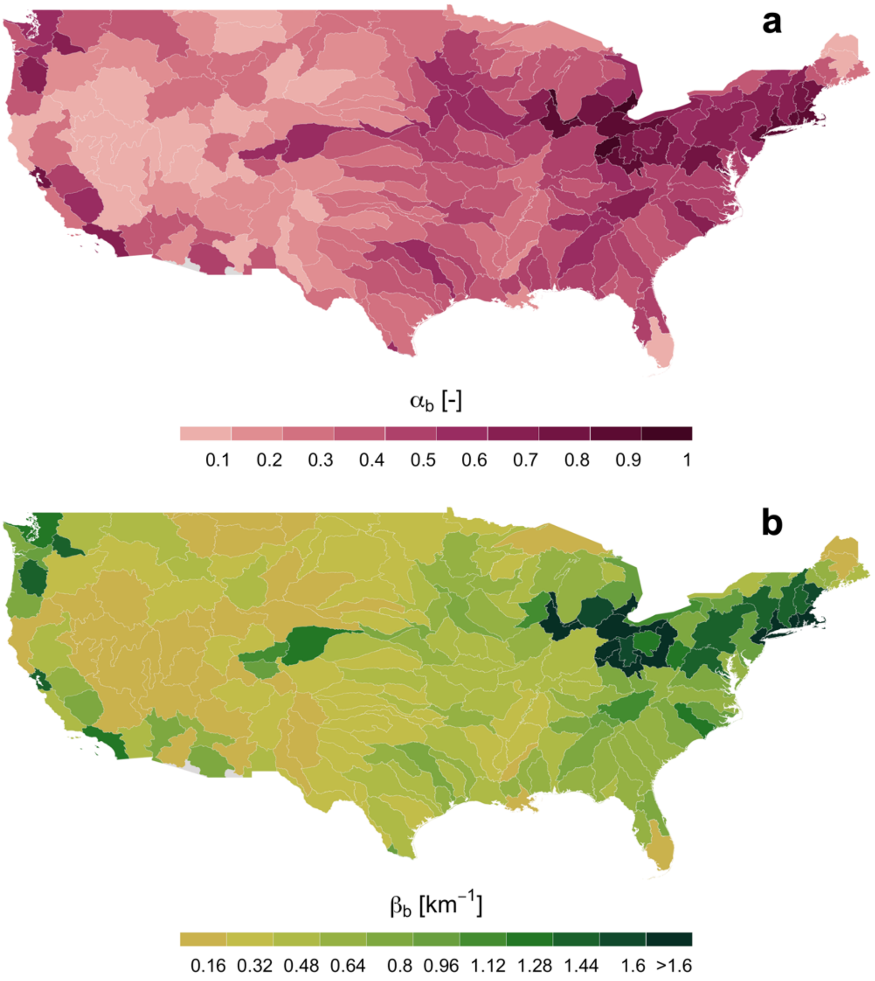
a
αb [-]
0.1
0.2
0.3
0.4
0.5
0.6
0.7
0.8
0.9
1
b
βb [km⁻¹]
0.16
0.32
0.48
0.64
0.8
0.96
1.12
1.28
1.44
1.6
>1.6

Figure B1 Spatial variability of α_b and β_b. parameters of the distance-decay model based on a 1 km wide distance bin and applied at the river basin level. **a**. Spatial variability of α_b. **b.** Spatial variability of β_b.

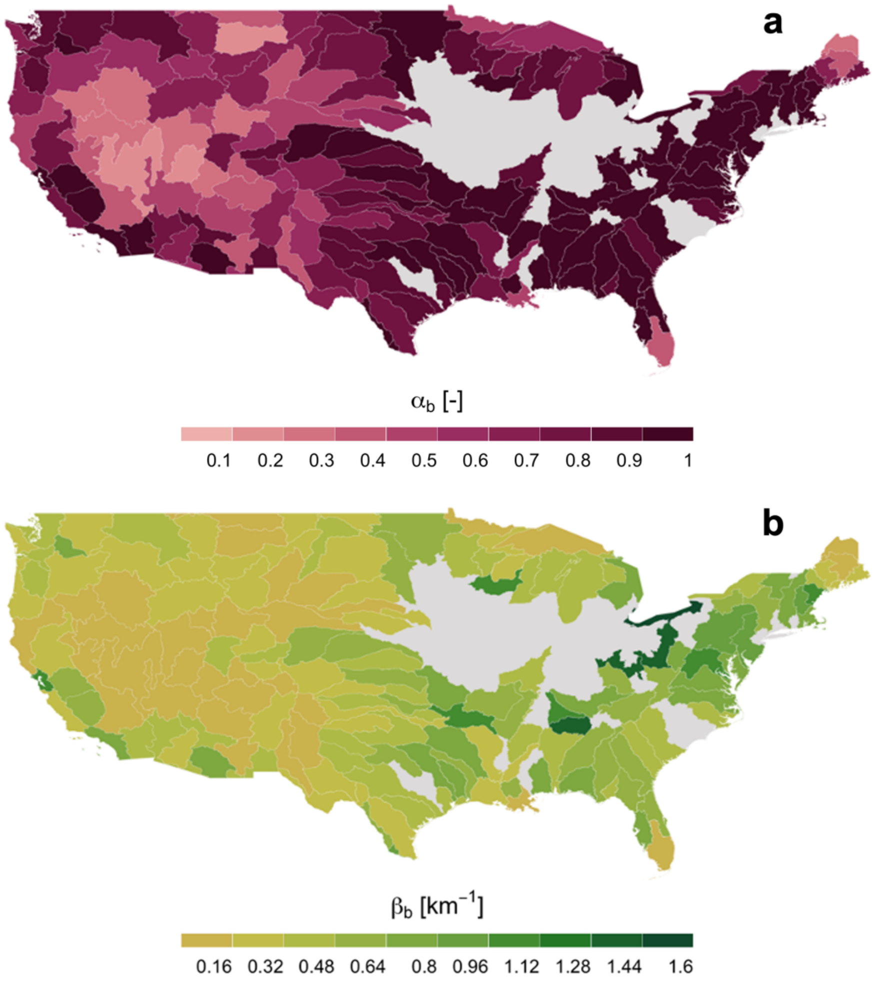
a
α_b [-]
0.1 0.2 0.3 0.4 0.5 0.6 0.7 0.8 0.9 1
b
β_b [km^{-1}]
0.16 0.32 0.48 0.64 0.8 0.96 1.12 1.28 1.44 1.6

Figure B2 Spatial variability of α_b and β_b parameters of the distance-decay model based on a 5 km wide distance bin and applied at the river basin level. River basins that are not fitted by the model using a 5 km wide distance bin are indicated in light grey. **a.** Spatial variability of α_b. **b.** Spatial variability of β_b.

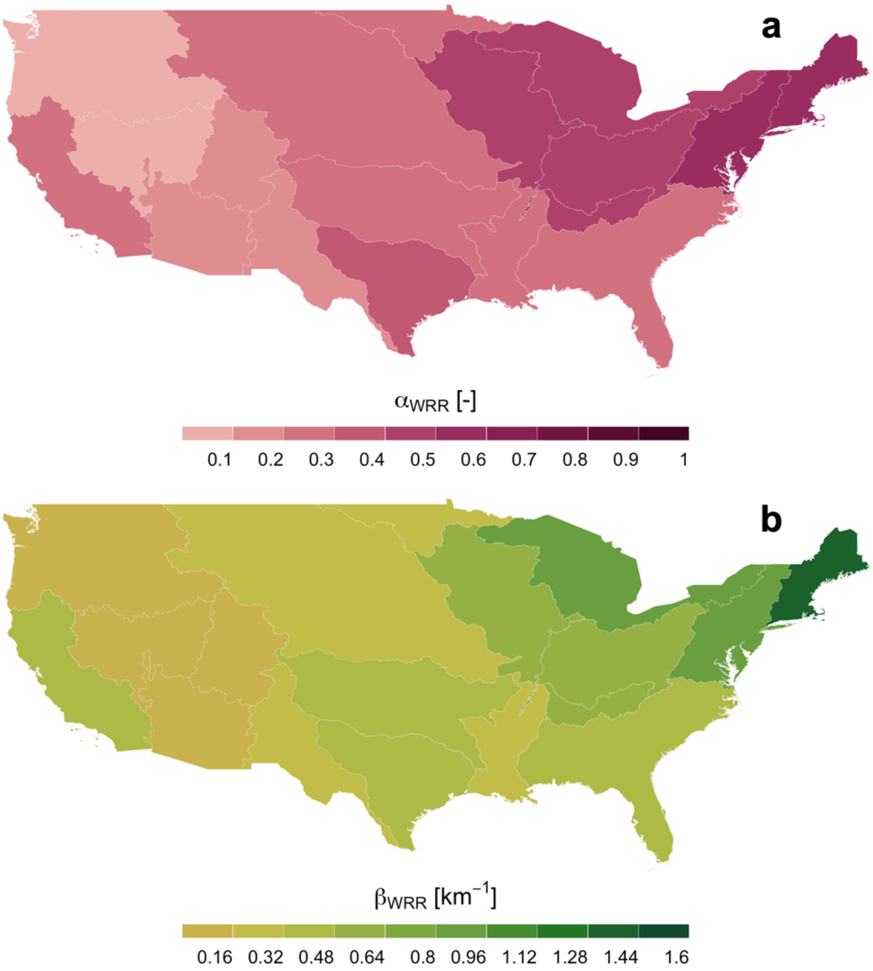
a
α_{WRR} [-]
0.1
0.2
0.3
0.4
0.5
0.6
0.7
0.8
0.9
1
b
β_{WRR} [km^{-1}]
0.16
0.32
0.48
0.64
0.8
0.96
1.12
1.28
1.44
1.6

Figure B3 Spatial variability of α_{WRR} and β_{WRR} parameters of the distance-decay model based on a 1 km wide distance bin and applied at the water resource region level. **a.** Spatial variability of α_{WRR}. **b.** Spatial variability of β_{WRR}.

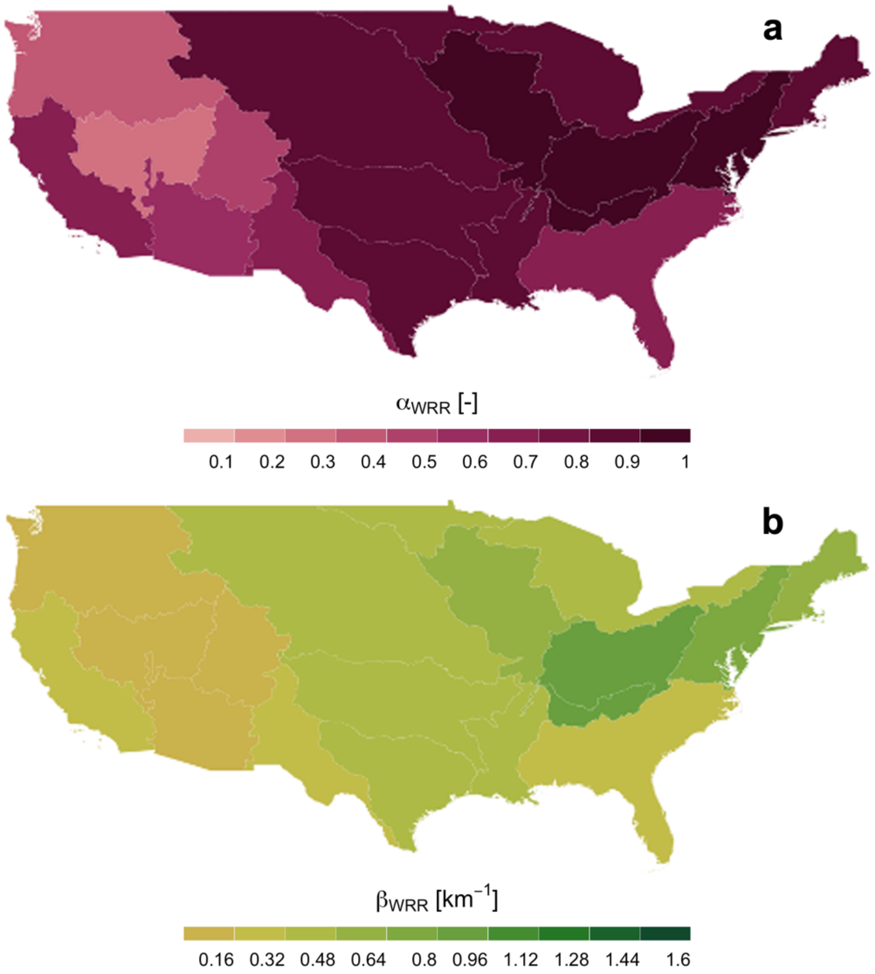
a
αWRR [-]
0.1
0.2
0.3
0.4
0.5
0.6
0.7
0.8
0.9
1
b
βWRR [km⁻¹]
0.16
0.32
0.48
0.64
0.8
0.96
1.12
1.28
1.44
1.6

Figure B4 Spatial variability of α_{WRR} and β_{WRR} parameters of the distance-decay model based on a 5 km wide distance bin and applied at the water resource region level. **a.** Spatial variability of α_{WRR}. **b.** Spatial variability of β_{WRR}.

Table B1 Main physical and climatic properties and model fit results, based on a 3 km wide distance bin, for the 18 water regions and 204 river basins across the CONUS. α_x and β_x are the distance-decay model parameters; *r* is the Pearson's correlation coefficient; $\langle d_x \rangle$ and $\langle \tilde{d}_x \rangle$ are the observed and theoretical average distance, respectively. Water resource regions name and ID are indicated in bold, while rows corresponding to the 13 basins whose data were fitted with a distance bin of 1 km are highlighted in light grey.

Water resource region/river basin name and ID	**Area [km^2]**	**Average elevation ± std dev [m]**	**Climatic regions and coverage percentage**	**α_x [-]**	**β_x [km^{-1}]**	**r**	**$\langle d_x \rangle$ [km]**	**$\langle \tilde{d}_x \rangle$ [km]**
New England Region (1)	156847	249 ± 190	Continental (100%)	0.792	0.768	0.999	3.042	1.302
St. John (101)	18879	298 ± 94	Continental (100%)	0.184	0.066	0.862	13.337	13.136
Penobscot (102)	22307	228 ± 152	Continental (100%)	0.232	0.097	0.877	11.955	9.503
Kennebec (103)	15260	302 ± 202	Continental (100%)	0.572	0.380	0.989	4.644	2.632
Androscoggin (104)	9071	400 ± 241	Continental (100%)	0.690	0.439	0.999	3.073	2.278
Maine Coastal (105)	13835	77 ± 52	Continental (100%)	0.585	0.327	0.998	3.983	3.054
Saco (106)	10835	175 ± 185	Continental (100%)	0.965	1.122	1.000	0.784	0.891
Merrimack (107)	12898	241 ± 185	Continental (100%)	0.947	1.021	1.000	0.871	0.979
Connecticut (108)	28943	358 ± 195	Continental (100%)	0.895	0.774	1.000	1.121	1.291

Massachusetts -Rhode Island Coastal. (109)	11159	54 ± 51	Continental (97.25%), Temperate (2.75%)	0.968	1.431	1.000	0.617	0.699
Connecticut Coastal (110)	12130	189 ± 129	Continental (100%)	0.985	1.404	1.000	0.517	0.712
St. Francois (111)	1531	420 ± 117	Continental (100%)	0.697	0.386	0.996	2.413	2.137
Mid Atlantic Region (2)	273049	284 ± 227	Temperate (82.73%), Continental (17.27%)	0.890	0.754	1.000	1.273	1.326
Richelieu (201)	19929	315 ± 220	Continental (100%)	0.877	0.715	1.000	1.437	1.397
Upper Hudson (202)	34040	337 ± 211	Continental (100%)	0.851	0.800	0.999	1.661	1.251
Lower Hudson-Long Island (203)	11293	75 ± 88	Continental (100%)	0.982	1.337	1.000	0.355	0.747
Delaware (204)	38260	217 ± 212	Continental (79.82%), Temperate (20.18%)	0.886	0.700	1.000	1.223	1.427
Susquehanna (205)	71081	398 ± 155	Continental (100%)	0.937	0.968	1.000	0.940	1.033
Upper Chesapeake (206)	18228	43 ± 61	Temperate (81.71%), Continental (18.29%)	0.834	0.586	1.000	1.591	1.680
Potomac (207)	37124	328 ± 254	Continental (76.97%), Temperate (23.03%)	0.939	0.931	1.000	0.858	1.074

Lower Chesapeake (208)	43094	211 ± 248	Temperate (82.73%), Continental (17.27%)	0.881	0.756	1.000	1.521	1.324
South Atlantic-Gulf Region (3)	695951	110 ± 118	Tropical (59.48%), Temperate (40.52%)	0.512	0.295	0.994	5.407	3.391
Chowan-Roanoke (301)	45324	141 ± 153	Temperate (98.56%), Continental (1.44%)	0.843	0.607	1.000	1.614	1.644
Neuse-Pamlico (302)	28656	48 ± 48	Temperate (100%)	0.759	0.534	0.999	2.162	1.870
Cape Fear (303)	25012	85 ± 77	Temperate (100%)	0.955	1.032	1.000	0.851	0.969
Pee Dee (304)	47969	131 ± 144	Temperate (99.66%), Continental (0.34%)	0.809	0.535	1.000	1.604	1.810
Edisto-Santee (305)	59320	167 ± 166	Temperate (99.55%), Continental (0.45%)	0.730	0.416	1.000	2.033	2.351
Ogeechee-Savannah (306)	43163	146 ± 156	Temperate (99.98%), Continental (0.02%)	0.733	0.436	1.000	2.103	2.247
Altamaha-St. Marys (307)	52445	108 ± 79	Temperate (100%)	0.811	0.545	1.000	1.716	1.833
St. Johns (308)	28940	21 ± 14	Temperate (100%)	0.816	0.547	1.000	1.579	1.794
Southern Florida (309)	42136	12 ± 9	Tropical (59.48%), Temperate (40.52%)	0.255	0.093	0.996	8.992	10.140

Peace-Tampa Bay (310)	23205	26 ± 14	Temperate (98.86%), Tropical (1.14%)	0.865	0.668	1.000	1.515	1.493
Suwannee (311)	34900	48 ± 29	Temperate (100%)	0.810	0.587	1.000	2.050	1.704
Ochlockonee (312)	9264	55 ± 31	Temperate (100%)	0.743	0.457	0.999	2.251	2.175
Apalachicola (313)	52371	155 ± 119	Temperate (100%)	0.809	0.540	1.000	1.741	1.850
Choctawhatchee-Escambia (314)	37226	74 ± 41	Temperate (100%)	0.861	0.642	1.000	1.508	1.555
Alabama (315)	58808	203 ± 128	Temperate (100%)	0.826	0.605	1.000	1.623	1.650
Mobile-Tombigbee (316)	55646	111 ± 67	Temperate (100%)	0.730	0.416	0.999	2.177	2.329
Pascagoula (317)	29210	80 ± 41	Temperate (100%)	0.801	0.551	0.999	2.028	1.816
Pearl (318)	22357	111 ± 39	Temperate (100%)	0.828	0.573	1.000	1.732	1.709
Great Lakes Region (4)	461782	248 ± 109	Continental (100%)	0.750	0.559	0.998	2.501	1.789
Western Lake Superior (401)	23904	400 ± 98	Continental (100%)	0.507	0.259	0.995	4.567	3.865
Southern Lake Superior-Lake Superior (402)	72536	208 ± 101	Continental (100%)	0.330	0.121	0.978	6.256	8.269

Northwestern Lake Michigan (403)	48209	311 ± 99	Continental (100%)	0.756	0.559	0.999	2.553	1.789
Southwestern Lake Michigan (404)	5165	238 ± 44	Continental (100%)	0.928	2.646	1.000	0.259	0.377
Southeastern Lake Michigan (405)	33400	259 ± 34	Continental (100%)	0.768	1.446	1.000	0.667	0.689
Northeastern Lake Michigan-Lake Michigan (406)	87484	209 ± 61	Continental (100%)	0.629	0.393	0.997	3.699	2.542
Northwestern Lake Huron (407)	18010	270 ± 70	Continental (100%)	0.648	0.340	1.000	2.730	2.879
Southwestern Lake Huron-Lake Huron (408)	47215	205 ± 43	Continental (100%)	0.875	0.717	1.000	1.425	1.394
St. Clair-Detroit (409)	9715	240 ± 43	Continental (100%)	0.937	2.851	1.000	0.290	0.351
Western Lake Erie (410)	30787	242 ± 38	Continental (100%)	0.848	1.859	1.000	0.449	0.532
Southern Lake Erie (411)	7752	289 ± 54	Continental (100%)	0.819	1.704	1.000	0.492	0.574
Eastern Lake Erie-Lake Erie (412)	20942	227 ± 103	Continental (100%)	0.952	1.001	1.000	0.871	0.999

Southwestern Lake Ontario (413)	9293	336 ± 190	Continental (100%)	0.928	0.857	1.000	1.079	1.142
Southeastern Lake Ontario (414)	17732	248 ± 131	Continental (100%)	0.891	0.830	1.000	1.418	1.204
Northeastern Lake Ontario-Lake Ontario-St. Lawrence (415)	29639	262 ± 210	Continental (100%)	0.648	0.374	0.999	3.111	2.676
Ohio Region (5)	422087	327 ± 182	Temperate (98.78%), Continental (1.22%)	0.897	0.746	1.000	1.462	1.341
Allegheny (501)	30242	490 ± 104	Continental (100%)	0.918	0.903	1.000	1.270	1.106
Monongahela (502)	19063	561 ± 235	Continental (100%)	0.878	0.725	1.000	1.220	1.379
Upper Ohio (503)	34707	317 ± 61	Continental (100%)	0.985	1.413	1.000	0.606	0.708
Muskingum (504)	20982	318 ± 43	Continental (100%)	0.692	1.264	0.999	0.906	0.788
Kanawha (505)	31574	680 ± 256	Continental (91.33%), Temperate (8.67%)	0.792	0.519	1.000	1.811	1.923
Scioto (506)	16873	284 ± 43	Continental (100%)	0.783	1.461	1.000	0.603	0.685
Big Sandy-Guyandotte (507)	15540	439 ± 171	Temperate (69.15%), Continental (30.85%)	0.831	0.573	1.000	1.481	1.705

Great Miami (508)	13982	299 ± 42	Continental (100%)	0.922	2.517	1.000	0.316	0.397
Middle Ohio (509)	23066	260 ± 47	Continental (95.5%), Temperate (4.5%)	0.984	1.368	1.000	0.560	0.731
Kentucky-Licking (510)	27669	307 ± 85	Continental (51.02%), Temperate (48.98%)	0.869	0.691	1.000	1.441	1.440
Green (511)	23882	202 ± 56	Temperate (100%)	0.923	0.830	1.000	1.526	1.175
Wabash (512)	85382	213 ± 51	Continental (99.75%), Temperate (0.25%)	0.896	0.732	1.000	1.555	1.356
Cumberland (513)	46325	308 ± 146	Temperate (98.78%), Continental (1.22%)	0.887	0.719	1.000	1.411	1.389
Lower Ohio (514)	32800	177 ± 54	Temperate (59.82%), Continental (40.18%)	0.861	0.649	1.000	1.660	1.467
Tennessee Region (6)	105961	437 ± 293	Temperate (100%)	0.908	0.790	1.000	1.368	1.265
Upper Tennessee (601)	44776	649 ± 302	Temperate (82.05%), Continental (17.95%)	0.881	0.754	1.000	1.279	1.325
Middle Tennessee-Hiwassee (602)	13447	451 ± 216	Temperate (99.72%), Continental (0.28%)	0.909	0.815	1.000	1.182	1.227
Middle Tennessee-Elk (603)	26831	262 ± 91	Temperate (100%)	0.966	1.118	1.000	1.079	0.895

Lower Tennessee (604)	20907	193 ± 59	Temperate (100%)	0.887	0.699	1.000	1.579	1.422
Upper Mississippi Region (7)	494707	295 ± 90	Continental (85.95%), Temperate (14.05%)	0.823	0.575	1.000	1.782	1.738
Mississippi Headwaters (701)	51994	378 ± 52	Continental (100%)	0.766	0.505	1.000	2.089	1.977
Minnesota (702)	43892	351 ± 64	Continental (100%)	0.944	0.945	1.000	1.246	1.046
St. Croix (703)	19932	333 ± 45	Continental (100%)	0.729	0.450	1.000	2.346	2.210
Upper Mississippi-Black-Root (704)	27763	324 ± 54	Continental (100%)	0.950	1.017	1.000	1.303	0.983
Chippewa (705)	24800	386 ± 74	Continental (100%)	0.530	0.235	0.996	3.622	4.026
Upper Mississippi-Maquoketa-Plum (706)	22358	302 ± 54	Continental (100%)	0.849	0.593	1.000	1.781	1.654
Wisconsin (707)	30885	372 ± 86	Continental (100%)	0.754	0.470	1.000	2.163	2.116
Upper Mississippi-Iowa-Skunk-Wapsipinicon (708)	59459	279 ± 61	Continental (100%)	0.507	0.607	0.952	1.147	1.307
Rock (709)	28414	262 ± 37	Continental (100%)	0.679	1.100	1.000	0.857	0.871
Des Moines (710)	37394	340 ± 67	Continental (100%)	0.990	1.546	1.000	1.004	0.646

Upper Mississippi-Salt (711)	26020	215 ± 38	Continental (100%)	0.869	0.645	1.000	1.623	1.476
Upper Illinois (712)	28407	218 ± 28	Continental (100%)	0.870	2.003	1.000	0.404	0.499
Lower Illinois (713)	46392	198 ± 28	Continental (100%)	0.453	0.546	0.990	1.424	1.541
Upper Mississippi-Kaskaskia-Meramec (714)	46997	185 ± 69	Continental (85.95%), Temperate (14.05%)	0.692	0.362	0.997	2.373	2.706
Lower Mississippi Region (8)	259286	71 ± 60	Temperate (100%)	0.630	0.342	1.000	3.521	2.927
Lower Mississippi-Hatchie (801)	25840	124 ± 28	Temperate (100%)	0.740	0.400	0.992	2.211	2.094
Lower Mississippi-St. Francis (802)	43346	89 ± 56	Temperate (93%), Continental (7%)	0.743	0.422	0.998	2.268	2.219
Lower Mississippi-Yazoo (803)	36573	73 ± 39	Temperate (100%)	0.692	0.362	0.997	2.514	2.500
Lower Red-Ouachita (804)	53291	93 ± 80	Temperate (100%)	0.558	0.241	0.981	3.196	3.596
Boeuf-Tensas (805)	13568	31 ± 9	Temperate (100%)	0.728	0.391	0.993	2.304	2.283
Lower Mississippi-Big Black (806)	18289	89 ± 35	Temperate (100%)	0.414	0.143	0.863	4.283	4.491

Lower Mississippi-Lake Maurepas (807)	15123	46 ± 41	Temperate (100%)	0.825	0.566	1.000	1.661	1.756
Louisiana Coastal (808)	34286	20 ± 23	Temperate (100%)	0.633	0.388	0.995	3.468	2.580
Lower Mississippi (809)	18968	5 ± 11	Temperate (100%)	0.331	0.144	0.998	8.505	6.934
Souris-Red-Rainy Region (9)	153909	401 ± 94	Continental (100%)	0.686	0.375	0.998	2.849	2.663
Souris (901)	22915	529 ± 78	Continental (96.89%), Arid (3.11%)	0.562	0.239	0.971	3.212	3.207
Red (902)	10175	371 ± 80	Continental (100%)	0.724	0.410	0.998	2.550	2.442
Rainy (903)	29247	403 ± 57	Continental (100%)	0.367	0.174	0.973	7.512	5.709
Missouri Region (10)	1323835	996 ± 620	Continental (99.94%), Temperate (0.06%)	0.646	0.376	1.000	3.653	2.658
Saskatchewan (1001)	1791	1788 ± 344	Continental (96.12%), Polar (3.88%)	0.348	0.133	0.956	6.422	6.757
Missouri Headwaters (1002)	36368	2066 ± 388	Continental (57.77%), Arid (41.81%), Polar (0.42%)	0.493	0.451	0.990	10.723	2.215

Missouri-Marias (1003)	51449	1346 ± 357	Arid (68.56%), Continental (31.41%), Polar (0.03%)	0.409	0.156	0.971	4.694	6.375
Missouri-Musselshell (1004)	60690	1081 ± 321	Arid (85.16%), Continental (14.84%)	0.121	0.037	0.838	18.399	18.785
Milk (1005)	38908	874 ± 179	Arid (94.27%), Continental (5.73%), Polar (0%)	0.264	0.096	0.991	8.635	9.960
Missouri-Poplar (1006)	27953	729 ± 86	Arid (99.6%), Continental (0.4%)	0.395	0.154	0.969	5.197	6.104
Upper Yellowstone (1007)	37430	1810 ± 662	Continental (50.97%), Arid (45.97%), Polar (3.05%)	0.436	0.226	0.991	8.199	4.418
Big Horn (1008)	59367	1849 ± 622	Arid (73.47%), Continental (22.93%), Polar (3.61%)	0.511	0.306	0.996	6.326	3.270
Powder-Tongue (1009)	48798	1326 ± 435	Arid (91.33%), Continental (8.19%), Polar (0.48%)	0.222	0.077	0.988	10.280	11.310
Lower Yellowstone (1010)	35887	858 ± 138	Arid (99.14%), Continental (0.86%)	0.527	0.326	0.988	5.794	3.063

Missouri-Little Missouri (1011)	44421	790 ± 180	Arid (68.94%), Continental (31.06%)	0.584	0.285	0.996	3.496	3.498
Cheyenne (1012)	62698	1186 ± 328	Arid (82.13%), Continental (17.87%)	0.272	0.092	0.952	7.410	8.584
Missouri-Oahe (1013)	95966	673 ± 120	Continental (52%), Arid (48%)	0.459	0.190	0.970	4.498	5.175
Missouri-White (1014)	52347	714 ± 211	Continental (50.5%), Arid (49.5%)	0.493	0.208	0.991	3.978	4.670
Niobrara (1015)	36532	959 ± 293	Continental (62.06%), Arid (37.94%)	0.290	0.102	0.939	7.013	8.662
James (1016)	55079	462 ± 64	Continental (100%)	0.728	0.399	0.997	2.347	2.413
Missouri-Big Sioux (1017)	37817	478 ± 62	Continental (100%)	0.875	0.671	1.000	1.711	1.441
North Platte (1018)	80311	1850 ± 521	Arid (82%), Continental (17.89%), Polar (0.11%)	0.341	0.148	0.992	7.792	6.702
South Platte (1019)	62514	1808 ± 607	Arid (75.56%), Continental (22.55%), Polar (1.89%)	0.847	0.701	0.999	1.483	1.427
Platte (1020)	21402	612 ± 194	Continental (100%)	0.973	1.202	1.000	1.045	0.832

Loup (1021)	39214	825 ± 188	Continental (95.29%), Arid (4.71%)	0.408	0.182	0.995	5.946	5.380
Elkhorn (1022)	18075	537 ± 104	Continental (100%)	0.568	0.271	0.992	3.322	3.433
Missouri-Little Sioux (1023)	24050	394 ± 44	Continental (100%)	0.505	0.612	0.952	1.172	1.430
Missouri-Nishnabotna (1024)	34967	341 ± 46	Continental (100%)	0.908	0.769	1.000	1.537	1.264
Republican (1025)	64737	966 ± 302	Continental (52.56%), Arid (47.44%)	0.763	0.463	1.000	2.203	2.158
Smoky Hill (1026)	51874	695 ± 250	Continental (76.17%), Arid (23.83%)	0.615	0.291	0.995	2.868	3.346
Kansas (1027)	39405	427 ± 90	Continental (100%)	0.906	0.760	1.000	1.423	1.267
Chariton-Grand (1028)	28466	284 ± 43	Continental (100%)	0.831	0.554	0.999	1.831	1.681
Gasconade-Osage (1029)	48535	301 ± 56	Continental (99.94%), Temperate (0.06%)	0.844	0.581	0.999	1.766	1.623
Lower Missouri (1030)	26785	239 ± 38	Continental (100%)	0.922	0.830	1.000	1.492	1.166
Arkansas-White-Red Region (11)	642156	709 ± 621	Temperate (100%)	0.689	0.390	1.000	2.759	2.561

Upper White (1101)	57886	286 ± 128	Temperate (80.24%), Continental (19.76%)	0.730	0.407	0.998	2.273	2.443
Upper Arkansas (1102)	64547	1818 ± 605	Arid (84.33%), Continental (13.62%), Polar (2.05%)	0.453	0.191	0.993	4.637	5.145
Middel Arkansas (1103)	52823	681 ± 224	Continental (70.95%), Arid (26.86%), Temperate (2.2%)	0.810	0.567	1.000	1.903	1.760
Upper Cimarron (1104)	31236	1086 ± 350	Arid (86.99%), Continental (7.41%), Temperate (5.6%)	0.483	0.210	0.990	4.402	4.739
Lower Cimarron (1105)	18432	404 ± 102	Temperate (99.71%), Continental (0.27%), Arid (0.01%)	0.803	0.556	1.000	2.040	1.789
Arkansas-Keystone (1106)	25590	404 ± 102	Temperate (77.72%), Continental (22.28%)	0.682	0.363	0.999	2.567	2.739
Neosho-Verdigris (1107)	53699	309 ± 72	Temperate (56.75%), Continental (43.25%)	0.834	0.571	1.000	1.695	1.719
Upper Canadian (1108)	32400	1808 ± 467	Arid (82.97%), Continental (17.01%), Polar (0.02%)	0.259	0.092	0.976	8.510	9.526

Lower Canadian (1109)	44093	861 ± 453	Arid (59.56%), Temperate (40.42%), Continental (0.02%)	0.592	0.317	0.999	3.952	3.152
North Canadian (1110)	46228	787 ± 387	Arid (61.17%), Temperate (38.81%), Continental (0.02%)	0.667	0.347	0.998	2.653	2.878
Lower Arkansas (1111)	41122	236 ± 117	Temperate (100%)	0.875	0.668	1.000	1.559	1.496
Red Headwaters (1112)	38352	860 ± 287	Arid (67.96%), Temperate (32.04%)	0.451	0.183	0.984	4.369	5.405
Red-Washita (1113)	64202	436 ± 174	Temperate (78.47%), Arid (21.53%)	0.656	0.332	0.997	2.674	3.009
Red-Sulphur (1114)	71545	147 ± 87	Temperate (100%)	0.801	0.507	0.999	1.928	1.968
Texas-Gulf Region (12)	464006	370 ± 348	Arid (85.42%), Temperate (14.58%)	0.692	0.407	1.000	2.703	2.457
Sabine (1201)	25541	100 ± 44	Temperate (100%)	0.819	0.598	1.000	1.885	1.666
Neches (1202)	25890	95 ± 44	Temperate (100%)	0.807	0.523	1.000	1.826	1.861
Trinity (1203)	46428	168 ± 86	Temperate (100%)	0.851	0.622	1.000	1.459	1.588

Galveston Bay-San Jacinto (1204)	18776	38 ± 36	Temperate (100%)	0.706	0.409	1.000	2.296	2.384
Brazos Headwaters (1205)	37361	997 ± 242	Arid (99.91%), Temperate (0.09%)	0.588	0.271	0.992	3.102	3.557
Middle Brazos (1206)	40544	402 ± 139	Temperate (75.16%), Arid (24.84%)	0.816	0.553	1.000	1.766	1.804
Lower Brazos (1207)	40177	209 ± 136	Temperate (100%)	0.875	0.664	1.000	1.594	1.490
Upper Colorado (1208)	41540	939 ± 195	Arid (99.78%), Temperate (0.22%)	0.617	0.293	0.992	2.847	3.324
Lower Colorado-San Bernard Coastal (1209)	73086	498 ± 232	Temperate (56.19%), Arid (43.81%)	0.716	0.420	1.000	2.402	2.381
Central Texas Coastal (1210)	44227	160 ± 170	Temperate (99.94%), Arid (0.06%)	0.613	0.318	1.000	3.189	3.099
Nueces-Southwestern Texas Coastal (1211)	70435	171 ± 161	Arid (85.42%), Temperate (14.58%)	0.552	0.301	0.997	4.329	3.322
Rio Grande Region (13)	344287	1506 ± 675	Arid (100%)	0.460	0.206	1.000	4.917	4.859
Rio Grande Headwaters (1301)	19788	2779 ± 446	Arid (52.34%), Continental (43.52%), Polar (4.14%)	0.338	0.121	0.888	5.751	7.493

Rio Grande-Elephant Butte (1302)	69986	2098 ± 413	Arid (85.89%), Continental (14.08%), Polar (0.03%)	0.424	0.173	0.994	4.734	5.646
Rio Grande-Mimbres (1303)	29599	1497 ± 279	Arid (98.92%), Continental (1.08%), Temperate (0%)	0.699	0.516	0.998	3.603	1.939
Rio Grande-Amistad (1304)	47939	997 ± 331	Arid (100%)	0.491	0.246	0.994	5.982	4.061
Rio Grande Closed Basins (1305)	45466	1568 ± 337	Arid (98.08%), Temperate (1.2%), Continental (0.72%)	0.231	0.071	0.676	7.771	10.728
Upper Pecos (1306)	61139	1525 ± 414	Arid (93.89%), Continental (3.68%), Temperate (2.43%)	0.330	0.136	0.992	7.751	7.112
Lower Pecos (1307)	53606	966 ± 257	Arid (100%)	0.518	0.232	0.992	4.145	4.312
Rio Grande-Falcon (1308)	13370	234 ± 108	Arid (100%)	0.707	0.381	0.997	2.452	2.612
Lower Rio Grande (1309)	3396	99 ± 46	Arid (100%)	0.947	1.205	1.000	1.299	0.830
Upper Colorado Region (14)	294126	2154 ± 510	Arid (84.16%), Continental (15.12%), Polar (0.72%)	0.283	0.137	0.977	11.682	7.308

Colorado Headwaters (1401)	25559	2594 ± 584	Continental (61.77%), Arid (32.31%), Polar (5.92%)	0.789	0.680	0.998	2.350	1.471
Gunnison (1402)	20789	2666 ± 574	Continental (53.45%), Arid (41.01%), Polar (5.55%)	0.600	0.372	0.986	3.875	2.689
Upper Colorado-Dolores (1403)	21678	2086 ± 520	Arid (73.09%), Continental (26.49%), Polar (0.41%)	0.256	0.100	0.928	9.747	9.258
Great Divide-Upper Green (1404)	54015	2226 ± 306	Arid (85.47%), Continental (13.69%), Polar (0.84%)	0.183	0.065	0.945	13.279	13.883
White-Yampa (1405)	34142	2179 ± 359	Arid (63.39%), Continental (36.56%), Polar (0.05%)	0.383	0.183	0.971	7.129	5.452
Lower Green (1406)	37598	2052 ± 520	Arid (79.9%), Continental (19.54%), Polar (0.55%)	0.556	0.296	0.997	4.617	3.378
Upper Colorado-Dirty Devil (1407)	35377	1827 ± 443	Arid (95.3%), Continental (4.7%)	0.191	0.071	0.981	13.744	13.269

San Juan (1408)	64968	1993 ± 436	Arid (84.16%), Continental (15.12%), Polar (0.72%)	0.249	0.152	0.852	15.781	6.564
Lower Colorado Region (15)	361999	1317 ± 650	Arid (99.73%), Temperate (0.27%)	0.377	0.151	0.997	5.860	6.630
Lower Colorado-Lake Mead (1501)	78557	1473 ± 509	Arid (95.86%), Continental (4.13%), Temperate (0.01%)	0.309	0.111	0.951	6.962	8.947
Little Colorado (1502)	69438	1920 ± 276	Arid (93.12%), Continental (6.8%), Temperate (0.08%)	0.307	0.116	0.981	7.322	8.187
Lower Colorado (1503)	44514	679 ± 479	Arid (99.91%), Temperate (0.09%)	0.676	0.455	0.994	3.155	2.199
Upper Gila (1504)	39511	1648 ± 472	Arid (92.44%), Continental (6.35%), Temperate (1.21%)	0.237	0.079	0.812	8.472	11.647
Middle Gila (1505)	43930	1007 ± 425	Arid (99.15%), Temperate (0.85%)	0.820	0.591	1.000	1.720	1.691
Salt (1506)	34863	1577 ± 531	Arid (67.79%), Temperate (19.49%), Continental (12.73%)	0.651	0.384	0.999	3.207	2.607

Lower Gila (1507)	39186	523 ± 385	Arid (98.66%), Temperate (1.34%)	0.399	0.153	0.977	4.911	6.483
Sonora (1508)	12001	952 ± 441	Arid (99.73%), Temperate (0.27%)	0.329	0.164	0.828	9.586	6.016
Great Basin Region (16)	367241	1763 ± 405	Arid (89.08%), Continental (10.92%)	0.151	0.050	0.974	14.776	18.706
Bear (1601)	19420	1982 ± 395	Arid (58.05%), Continental (41.91%), Polar (0.04%)	0.317	0.111	0.920	5.923	8.401
Great Salt Lake (1602)	74470	1671 ± 398	Arid (84.33%), Continental (15.67%)	0.138	0.044	0.958	15.722	18.626
Escalante Desert-Sevier Lake (1603)	42507	1920 ± 441	Arid (89.08%), Continental (10.92%)	0.114	0.034	0.750	18.706	20.433
Black Rock Desert-Humboldt (1604)	74250	1671 ± 314	Arid (98.05%), Continental (1.95%)	0.158	0.051	0.808	13.870	18.263
Central Lahontan (1605)	32889	1684 ± 451	Arid (77.38%), Continental (21.21%), Temperate (1.4%), Polar (0.01%)	0.208	0.068	0.862	9.820	12.252

Central Nevada Desert Basins (1606)	12370	1808 ± 397	Arid (98.84%), Continental (1.14%), Polar (0.02%)	0.095	0.028	0.727	20.666	26.019
Pacific Northwest Region (17)	709825	1199 ± 642	Arid (60.1%), Continental (39.7%), Polar (0.2%)	0.243	0.093	0.986	10.963	10.686
Kootenai-Pend Oreille-Spokane (1701)	94069	1365 ± 457	Continental (87.39%), Arid (12.49%), Polar (0.12%)	0.684	0.463	0.999	3.855	2.160
Upper Columbia (1702)	57657	845 ± 475	Arid (59.74%), Continental (39.49%), Polar (0.74%), Temperate (0.03%)	0.646	0.349	1.000	2.913	2.864
Yakima (1703)	15940	827 ± 452	Continental (56.71%), Arid (42.82%), Temperate (0.45%), Polar (0.02%)	0.936	1.303	1.000	1.346	0.768
Upper Snake (1704)	93091	1840 ± 461	Arid (60.1%), Continental (39.7%), Polar (0.2%)	0.499	0.253	0.996	5.094	3.953

Middle Snake (1705)	95762	1421 ± 415	Arid (72.02%), Continental (27.97%), Polar (0%)	0.141	0.049	0.863	17.636	18.384
Lower Snake (1706)	90799	1478 ± 656	Continental (76.42%), Arid (23.31%), Temperate (0.15%), Polar (0.12%)	0.434	0.332	0.992	13.312	3.013
Middle Columbia (1707)	77335	986 ± 468	Arid (53%), Continental (41.1%), Temperate (5.74%), Polar (0.16%)	0.407	0.232	0.982	7.982	4.307
Lower Columbia (1708)	15027	599 ± 464	Temperate (73.62%), Continental (25.94%), Polar (0.44%)	0.840	0.775	0.998	1.776	1.290
Willamette (1709)	30329	544 ± 484	Temperate (88.62%), Continental (11.28%), Polar (0.1%)	0.812	0.666	0.999	1.877	1.501
Oregon-Washington Coastal (1710)	59281	503 ± 427	Temperate (94.94%), Continental (4.94%), Polar (0.12%)	0.586	0.437	0.994	5.358	2.291
Puget Sound (1711)	35473	632 ± 586	Temperate (60.32%), Continental (38.53%), Polar	0.780	0.797	0.997	2.798	1.255

			(1.09%), Arid (0.06%)					
Oregon Closed Basins (1712)	45062	1530 ± 222	Arid (89.87%), Continental (10.13%)	0.173	0.057	0.826	12.977	16.719
California Region (18)	416156	888 ± 724	Temperate (77.67%), Arid (21.74%), Continental (0.59%)	0.558	0.312	0.993	4.245	3.202
Klamath-Northern California Coastal (1801)	64767	1037 ± 542	Temperate (64.36%), Continental (24.71%), Arid (10.91%), Polar (0.03%)	0.273	0.102	0.980	8.623	9.391
Sacramento (1802)	71960	946 ± 698	Temperate (67.86%), Continental (24.71%), Arid (7.39%), Polar (0.04%)	0.578	0.342	0.987	3.980	2.924
Tulare-Buena Vista Lakes (1803)	42579	846 ± 981	Arid (56.08%), Temperate (29.74%), Continental (12.92%), Polar (1.27%)	0.870	0.693	1.000	1.533	1.442
San Joaquin (1804)	41009	825 ± 973	Temperate (59.6%), Arid (23.92%), Continental (15.53%),	0.880	0.776	1.000	1.709	1.288

			Polar (0.95%)					
San Francisco Bay (1805)	10482	216 ± 239	Temperate (100%)	0.945	0.956	1.000	0.845	1.046
Central California Coastal (1806)	29872	492 ± 350	Temperate (92.82%), Arid (7.18%)	0.632	0.445	0.983	3.748	2.248
Southern California Coastal (1807)	28748	626 ± 540	Temperate (77.67%), Arid (21.74%), Continental (0.59%)	0.907	0.795	1.000	1.053	1.257
North Lahontan (1808)	11769	1627 ± 261	Arid (49.03%), Continental (48.89%), Temperate (2.08%)	0.270	0.089	0.775	7.001	9.454
Northern Mojave-Mono Lake (1809)	73611	1163 ± 658	Arid (88.39%), Continental (6.34%), Temperate (4.73%), Polar (0.54%)	0.248	0.088	0.934	8.866	10.820
Southern Mojave-Salton Sea (1810)	41361	548 ± 470	Arid (93.38%), Temperate (6.4%), Continental (0.22%)	0.756	0.475	1.000	2.244	2.103